Homotopic local-global parcellation of the human cerebral cortex from resting-state functional connectivity

Xiaoxuan Yan[1,2,3,4], Ru Kong[1,2,3], Aihuiping Xue[1,2,3], Qing Yang[1,2,3], Csaba Orban[1,2,3], Lijun An[1,2,3], Avram J. Holmes[5], Xing Qian[1], Jianzhong Chen[1,2,3], Xi-Nian Zuo[6,7], Juan Helen Zhou[1,2,4], Marielle V Fortier[8,9], Ai Peng Tan[9,10], Peter Gluckman[11], Yap Seng Chong[9,12], Michael Meaney[9,13], Danilo Bzdok[14,15], Simon B. Eickhoff[16,17], B.T. Thomas Yeo[1,2,3,4,18]

[1]Centre for Sleep and Cognition (CSC) & Centre for Translational Magnetic Resonance Research (TMR), Yong Loo Lin School of Medicine, National University of Singapore, Singapore [2]Department of Electrical and Computer Engineering, National University of Singapore, Singapore [3]N.1 Institute for Health and Institute for Digital Medicine (WisDM), National University of Singapore, Singapore, [4]Integrative Sciences and Engineering Programme (ISEP), National University of Singapore, Singapore, [5]Yale University, Departments of Psychology and Psychiatry, New Haven, CT, USA, [6]State Key Laboratory of Cognitive Neuroscience and Learning/IDG McGovern Institute for Brain Research, Beijing Normal University, Beijing, China, [7]National Basic Public Science Data Center, China, [8]Department of Diagnostic and Interventional Imaging, KK Women's and Children's Hospital, Singapore [9]Singapore Institute for Clinical Sciences (SICS), Agency for Science, Technology and Research (A*STAR), Singapore, [10]Department of Diagnostic Radiology, Yong Loo Lin School of Medicine, National University of Singapore, Singapore, [11]UK Centre for Human Evolution, Adaptation and Disease, Liggins Institute, University of Auckland, Auckland, New Zealand, [12]Department of Obstetrics and Gynaecology, Yong Loo Lin School of Medicine, National University of Singapore, Singapore, Singapore, [13]Department of Neurology and Neurosurgery, McGill University, Montreal, QC, Canada, [14]Department of Biomedical Engineering, Montreal Neurological Institute, McGill University, Montreal, QC, Canada [15]Mila - Quebec AI Institute, Montreal, QC, Canada [16]Institute for Systems Neuroscience, Medical Faculty, Heinrich-Heine University Düsseldorf, Düsseldorf, Germany [17]Institute of Neuroscience and Medicine, Brain & Behaviour (INM-7), Research Center Jülich, Jülich, Germany, [18]Martinos Center for Biomedical Imaging, Massachusetts General Hospital, Charlestown, MA, USA

Address correspondence to:
B.T. Thomas Yeo
CSC, TMR, ECE, N.1 & WISDM
National University of Singapore
Email: thomas.yeo@nus.edu.sg

Abstract

Resting-state fMRI is commonly used to derive brain parcellations, which are widely used for dimensionality reduction and interpreting human neuroscience studies. We previously developed a model that integrates local and global approaches for estimating areal-level cortical parcellations. The resulting local-global parcellations are often referred to as the Schaefer parcellations. However, the lack of homotopic correspondence between left and right Schaefer parcels has limited their use for brain lateralization studies. Here, we extend our previous model to derive homotopic areal-level parcellations. Using resting-fMRI and task-fMRI across diverse scanners, acquisition protocols, preprocessing and demographics, we show that the resulting homotopic parcellations are as homogeneous as the Schaefer parcellations, while being more homogeneous than five publicly available parcellations. Furthermore, weaker correlations between homotopic parcels are associated with greater lateralization in resting network organization, as well as lateralization in language and motor task activation. Finally, the homotopic parcellations agree with the boundaries of a number of cortical areas estimated from histology and visuotopic fMRI, while capturing sub-areal (e.g., somatotopic and visuotopic) features. Overall, these results suggest that the homotopic local-global parcellations represent neurobiologically meaningful subdivisions of the human cerebral cortex and will be a useful resource for future studies. Multi-resolution parcellations estimated from 1479 participants are publicly available (GITHUB_LINK).

1 Introduction

Information processing in the human brain is facilitated by the transformation of neural signals across cortical areas (Ungerleider and Desimone, 1986; Felleman and Van Essen, 1991). Therefore, accurate delineation of cortical areas is an important goal in systems neuroscience (Amunts and Zilles, 2015). Cortical areas are defined based on the principle that an area should exhibit distinct architectonics, topography, connectivity, and function (Kaas, 1987; Felleman and Van Essen, 1991; Eickhoff et al., 2018a). Traditionally, these criteria were evaluated with a broad range of invasive techniques. However, recent progress in non-invasive brain imaging techniques offer the opportunities to delineate cortical areas in vivo (Sereno et al., 1995; Cohen et al., 2008; Van Essen and Glasser 2014).

One popular non-invasive brain imaging technique is resting-state functional connectivity (RSFC). RSFC measures the synchrony of fMRI signals between brain regions, while a participant is "resting" in the scanner in the absence of any explicit task (Biswal et al., 1995). RSFC has been widely used to estimate a small number of (typically less than 20) large-scale brain networks (Damoiseaux et al., 2006; Calhoun et al., 2008; Smith et al., 2009; Power et al., 2011). RSFC has also been used to parcellate (or subdivide) the brain into hundreds of finer parcels (Craddock et al., 2012; Shen et al., 2013; Honnorat et al., 2015; Eickhoff et al., 2015). We refer to these finer parcellations as areal-level parcellations, since their boundaries are known to align with certain cortical areas (Wig et al., 2014; Gordon et al., 2016; Schaefer et al., 2018). However, cortical areas are internally heterogeneous (Kaas 1987), so most RSFC parcellations also capture sub-areal features, such as visual eccentricity and somatomotor representations of different body parts (Yeo et al., 2011; Gordon et al., 2016; Schaefer et al., 2018). This sub-areal characteristic can be advantageous, for instance when modeling a behavioral task involving button presses, it might be useful for hand and tongue motor regions to be represented by different parcels.

We previously developed a gradient-weighted Markov Random Field (gwMRF) model for estimating areal-level RSFC parcellations (Schaefer et al., 2018). The gwMRF model integrates two popular approaches for estimating brain parcellations. The local gradient approach (Hirose et al., 2012; Wig et al., 2014; Laumann et al., 2015; Xu et al., 2016) detects abrupt changes in RSFC patterns between adjacent spatial locations in the cerebral cortex. The locations of these abrupt changes often correspond to known cortical areal boundaries (Wig et al., 2014; Gordon et al., 2016). On the other hand, the global similarity approach clusters the brain into parcels with similar RSFC patterns or resting-fMRI time courses (van den Heuvel et al., 2008; Power et al., 2011; Yeo et al., 2011; Ryali et al.,

2013). By construction, the resulting parcels are more homogeneous (than those obtained with the local gradient approach), which is useful for dimensionality reduction of fMRI data. By combining both local gradient and global similarity approaches, the gwMRF parcellations agreed well with the boundaries of certain cortical areas defined using histology and visuotopic fMRI (Schaefer et al., 2018). The resulting gwMRF parcels were also more homogeneous than other parcellations evaluated using task-fMRI and resting-fMRI (Schaefer et al., 2018).

However, there is no homotopic correspondence between left and right gwMRF parcels, which limits their use for lateralization studies. Histological studies suggest the presence of homotopic pairs of cortical areas in roughly spatially homotopic locations across the hemispheres (Amunts et al., 2020). Homotopic areas do not necessarily have the same function, e.g., language processing is lateralized towards the left hemisphere in most participants (Szaflarski et al., 2006; Hartwigsen et al., 2021; Malik-Moraleda et al., 2022). Despite functional lateralization, most higher-level cognitive functions are supported by distributed networks across the two hemispheres, enabled by inter-hemispheric commissural fibers (e.g., corpus callosum) and subcortical relays (Middleton and Strick, 2020; Schmahmann et al., 2008; Jones 2012). Direct and indirect connections between the two hemispheres in turn lead to strong homotopic RSFC observed in both electrophysiological (Duffy et al., 1996) and fMRI (Lowe et al., 1998; Salvador et al., 2005) studies. Spatial variation in homotopic RSFC has been observed along the functional hierarchy with sensory-motor regions exhibiting stronger homotopic RSFC than association regions (Stark et al., 2008). Within the sensory-motor cortex, tongue regions exhibit stronger homotopic RSFC than hand and foot regions (Yeo et al., 2011), consistent with nonhuman primate studies showing that the representations of midline structures in S1 and M1 (e.g., face) have denser callosal connections than those of distal limbs (e.g., hand and foot; Pandya and Vignolo 1971; Jones and Wise 1977; Killackey et al., 1983; Gould et al., 1986).

In this study, we extend the gwMRF model to derive homotopic areal-level parcellations, in which pairs of parcels exist in approximately spatially homotopic locations across the hemispheres. Homotopic parcellations have been derived by manual delineation of parcellation boundaries (Glasser et al., 2016) or post hoc grouping of parcel pairs (Joliot et al., 2015). By contrast, our homotopic Markov Random Field (hMRF) approach is fully automated and seeks to preserve the desirable properties of the original gwMRF approach. We compared the hMRF parcellations with six publicly available parcellations (Craddock et al., 2012; Shen et al., 2013; Joliot et al., 2015; Glasser et al., 2016; Gordon et al., 2016;

Schaefer et al., 2018) using multiple datasets. Based on task-fMRI and resting-fMRI, the hMRF parcels were as homogeneous as gwMRF parcels, while being more homogeneous than the other five parcellations. Compared with other fully automated approaches, the hMRF parcellations exhibited similar alignment with architectonic and visuotopic areal boundaries. Multi-resolution hMRF parcellations from 100 to 1000 parcels are made publicly available as reference maps for future studies.

2 Material and Methods

2.1 Overview

A homotopic Markov Random Field (hMRF) parcellation procedure was developed and applied to resting-fMRI from the GSP dataset. Using data collected from multiple scanners, acquisition protocols and preprocessing procedures, the estimated homotopic parcellations were compared with six previously published resting-fMRI parcellations (Craddock et al., 2012; Shen et al., 2013; Joliot et al., 2015; Glasser et al., 2016; Gordon et al., 2016; Schaefer et al., 2018). Of these six parcellations, two of them were homotopic (Joliot et al., 2015; Glasser et al., 2016). A final set of hMRF parcellations at various resolutions were estimated from the full GSP dataset and further characterized.

2.2 fMRI Datasets

2.2.1 GSP dataset

The GSP dataset consisted of resting-fMRI data from 1489 young adults aged between 18 to 35 years old (Holmes et al., 2015). All imaging data were collected on matched 3T Tim Trio scanners (Siemens Healthcare) at Harvard University and Massachusetts General Hospital using the vendor-supplied 12-channel phased-array head coil. For each participant, one or two resting-fMRI runs were acquired. Out of the total 1489 participants, 1083 participants had two runs and 406 participants had one run. Each run was acquired in 3 mm isotropic resolution with a TR of 3.0 s and lasted for 6 min and 12 s. The structural data consisted of one 1.2 mm isotropic scan for each participant.

Detailed information about the resting-fMRI preprocessing can be found elsewhere (Li et al., 2019). Here we provide the broad outlines of the processing steps, which utilized a mixture of FreeSurfer 5.3.0 (Fischl, 2012), FSL 5.0.8 (Jenkinson et al., 2012) and in-house Matlab functions. The processing steps were as follows. (1) First four frames were removed. (2) Slice time correction was applied. (3) Motion correction and censoring of outlier volumes were performed. Volumes with framewise displacement (FD) > 0.2 mm or root-mean-square of voxel-wise differentiated signal (DVARS) > 50, along with one volume before and two volumes after, were marked as outliers. Uncensored segments of data lasting fewer than five contiguous volumes were also labeled as censored frames. BOLD runs with more than half of the volumes labeled as censored frames were removed. (4) Alignment with structural images with boundary-based registration was performed (Greve and Fischl, 2009). (5) White matter and ventricular signals, whole brain signal, six motion parameters, and their temporal

derivatives were regressed from the fMRI data. Outlier frames from step 3 were excluded when computing the regression coefficients. (6) Censored frames were interpolated with Lomb-Scargle periodogram (Power et al., 2014), (7) Bandpass filtering (0.009Hz < f < 0.08Hz) was performed. (8) Data was projected to the FreeSurfer fsaverage6 space and smoothed by a 6mm full-width half-maximum (FWHM) kernel.

Only participants with at least one run remaining (N = 1479) were considered. The 1479 participants were further divided into training (N = 740) and test (N = 739) sets. The GSP training set was used to estimate hMRF parcellations, while the GSP test set was used to evaluate the parcellations (Sections 2.4 and 2.5). The full dataset (N = 1479) was also used to estimate a final set of hMRF parcellations at different resolution (Section 2.6).

2.2.2 HCP dataset

For the purpose of evaluation (Section 2.4), we considered resting-fMRI data from the HCP S1200 release. Details about the acquisition protocol and minimal processing for the HCP data can be found elsewhere (Glasser et al., 2013; Van Essen et al., 2012b). Briefly, each participant has 4 resting-fMRI runs acquired from a custom-made Skyra scanner. Each run was acquired in 2 mm isotropic resolution with a TR of 0.72 s and lasted for 14 min and 33 s. The structural data consisted of one 0.7 mm isotropic scan for each participant.

We utilized ICA-FIX resting-fMRI data in MNI152 space, which have been denoised with ICA-FIX (Griffanti et al., 2014; Salimi-Khorshidi et al., 2014) and smoothed by a Gaussian kernel with 6 mm FWHM. We also considered MSMAII ICA-FIX resting-fMRI data, which were projected to fs_LR32k surface space (Van Essen et al., 2012b), smoothed by a Gaussian kernel with 2 mm FWHM and aligned with MSMAII (Robinson et al., 2014).

To further remove head motion-related artifacts (Burgess et al., 2016; Siegel et al., 2017), additional censoring was performed (volumes with FD > 0.2 mm or DVARS > 50 were marked as outliers) and runs with more than 50% censored frames were removed. Only participants with at least one resting-fMRI run remaining (N = 1030) were considered.

Furthermore, for the purpose of evaluation, we utilized task contrasts released by the HCP in fs_LR32k surface space. Details of the task contrasts can be found in the HCP documentation and publications (Barch et al., 2013). Briefly, there were seven tasks: social cognition, motor, gambling, working memory, language processing, emotional processing, and relational processing. For each task, there were multiple task contrasts released by the

HCP in fsLR surface space. We used all independent task contrasts. The subset of HCP participants with available contrasts for all tasks was considered (N = 956).

2.2.3 ABCD dataset

The GSP test set (Section 2.2.1) and HCP dataset (Section 2.2.2) allowed us to evaluate parcellation quality in young adults in MNI152, fsaverage and fs_LR32k spaces. We also considered 9- to 10-year-old children from the Adolescent Brain Cognitive Development (ABCD) dataset to evaluate parcellation quality in children. Details of the ABCD dataset can be found elsewhere (Casey et al., 2018). Briefly, each participant has 4 resting-fMRI runs acquired from Philips, GE or Siemens scanners. Consistent with our previous study (Chen et al., 2022), individuals from Philips scanners were excluded due to incorrect preprocessing. Each resting-fMRI run was acquired in 2.4 mm isotropic resolution with a TR of 0.8 s and lasted for 5 min. The structural data consisted of one 1 mm isotropic scan for each participant.

We considered 2262 participants from our previous study (Chen et al., 2022). Briefly, we utilized minimally preprocessed fMRI data released by the ABCD study (Hagler et al., 2019). The minimally processed data were further preprocessed with the following steps. (1) Functional images were aligned to T1 images using boundary-based registration (Greve & Fischl, 2009). (2) Respiratory pseudo-motion was removed with a bandstop filter of 0.31-0.43Hz (Fair et al., 2020). (3) Frames with FD > 0.3 mm or DVARS > 50, along with one volume before and two volumes after, were marked as outliers and subsequently censored. Uncensored segments of data consisting of less than 5 frames were also censored. Runs with more than 50% censored frames were not considered. (4) Global, white matter and ventricular signals, 6 motion parameters, and their temporal derivatives were regressed from the fMRI data. Censored frames were not considered when computing the regression coefficients. (5) Censored frames were interpolated with Lomb-Scargle periodogram (Power et al., 2014). (6) Bandpass filtering (0.009Hz – 0.08Hz) was applied. (7) Finally, the data was projected onto FreeSurfer fsaverage6 surface space and smoothed using a 6 mm full-width half maximum kernel.

The ABCD study also provided task-fMRI data from the N-back, monetary incentive delay (MID), and stop signal tasks (SST). There were 2 fMRI runs for each task. Each run was acquired in 2.4 mm isotropic resolution with a TR of 0.8 s. Each MID run was 322.4-secs long. Each N-back run was 289.6-secs long. Each SST run was 349.6-secs long.

Preprocessing of the task data was similar to the resting-fMRI data with some notable differences. Briefly, we utilized minimally preprocessed fMRI data released by the ABCD study (Hagler et al., 2019). The minimally processed data were further preprocessed with the following steps. (1) Functional images were aligned to T1 images using boundary-based registration (Greve & Fischl, 2009). (2) Respiratory pseudo-motion was removed with a bandstop filter of 0.31-0.43Hz (Fair et al., 2020). (3) Frames with FD > 0.3 mm or DVARS > 50, along with one volume before and two volumes after, were marked as outliers. Segments of data consisting of less than 5 non-outlier frames were also marked as outliers. Runs with more than 50% outlier frames were not considered. (4) 6 motion parameters, and their temporal derivatives were regressed from the fMRI data. Outlier frames were not used to compute regression coefficients. (5) Finally, the data was projected onto FreeSurfer fsaverage6 surface space and smoothed using a 6 mm full-width half maximum kernel. To estimate the task-related activation, we fitted general linear model to the preprocessed task-fMRI data using AFNI's 3dDevonvolve (Cox, 1996). We utilized task regressors provided by ABCD (Casey et al., 2018), comprising 15 task conditions from MID, 9 conditions from N-back and 8 conditions from SST. The resulting activation z-scores were finally projected to the fsaverage6 surface mesh.

2.2.4 GUSTO dataset

The previous evaluation datasets comprised mostly participants from North America. Given concerns about cross-ethnicity generalization failures in neuroimaging studies (Li et al., 2022), we also considered resting-fMRI data from 7.5-year-old children in the Growing Up in Singapore Towards Healthy Outcomes (GUSTO) dataset (Soh et al., 2014). Each participant has 1 resting-fMRI run collected on a Siemens Prisma scanner. Each run was acquired in 3 mm isotropic resolution with a TR of 2.62 s and lasted for 5.24 min. The structural data consisted of one 1 mm isotropic scan for each participant.

The processing steps are as follows. (1) First four frames were removed. (2) Slice time correction was applied. (3) Motion correction was performed, and frames with FD > 0.6 mm or DVARS > 80 were marked as outliers. (4) Alignment with structural images with boundary-based registration was performed (Greve and Fischl, 2009). (5) White matter and ventricular signals, whole brain signal, six motion parameters, and their temporal derivatives were regressed from the fMRI data. Outlier frames from step 3 were excluded when computing the regression coefficients (6) AFNI despiking was applied to the data. (7) The resulting time courses were bandpass filtered (0.009Hz < f < 0.08Hz). (8) The fMRI data was

projected to the FreeSurfer fsaverage6 space. (9) Surface data were smoothed by a 6mm full-width half-maximum (FWHM) kernel. Participants with poor T1-fMRI alignment (based on visual QC) was excluded. Participants with less than 4 minutes of non-outlier frames were also excluded, yielding a final set of 393 participants.

2.3 hMRF parcellation procedure

A typical MRF model is defined by an objective function comprising several competing terms encoding the ideal properties of a segmentation or parcellation. The homotopic Markov Random Field (hMRF) model is the same as the gwMRF model (Schaefer et al., 2018) except for two additional terms to encourage homotopic parcels.

The gwMRF objective function comprises three terms, which encode the global connectivity similarity objective, the local gradient objective, and a spatial contiguity constraint. The global connectivity similarity term encourages brain locations with similar preprocessed fMRI time courses to be assigned to the same parcel. The local gradient term penalizes adjacent brain locations with different parcellation labels. This penalty is relaxed in the presence of strong local RSFC gradients (hence the name "gradient weighted"). With only the first two terms, the resulting parcellation will contain spatially distributed parcels due to long-range RSFC. Therefore, the spatial contiguity term encourages brain locations within a parcel to be near to the parcel center. More details about the gwMRF model can be found elsewhere (Schaefer et al., 2018). For completeness, Supplementary Methods S1 provides details about the three gwMRF terms.

Our proposed hMRF objective function has a fourth homotopic constraint term that encourages homotopic pairs of vertices to be assigned to homotopic pairs of parcels. Homotopic vertex pairs were defined as follows. The left and right fsaverage6 hemispheres were first registered using the Freesurfer's "mris_left_right_register" function. After registration, the closest right hemisphere vertex was found for each left hemisphere vertex. Similarly, the closest left hemisphere vertex was found for each right hemisphere vertex. A pair of left and right hemisphere vertices was considered homotopic if they were each other's closest neighbor. Without loss of generality, the *p*-th parcels on the left and right hemispheres are assumed to be homotopic pair of parcels. For example, in the case of the 400-region hMRF parcellation, we assume that parcels 1 to 200 are in the left hemisphere and parcels 201 to 400 are in the right hemisphere. Furthermore, we assume that parcels 1 and 201 are homotopic, parcels 2 and 202 are homotopic, etc. The homotopic constraint imposes a penalty if a pair of homotopic vertices is assigned to non-homotopic pairs of parcels.

Because of the strong homotopic correlations between the two hemispheres, a fifth "bookkeeping" term is necessary to prevent any parcel from spanning across both hemispheres. Using the example of the 400-region hMRF parcellation, this bookkeeping term imposes a very large penalty if any right hemisphere vertex is assigned to parcels 1 to 200 or if any left hemisphere vertex is assigned to parcels 201 to 400.

Mathematical details of the hMRF model are found in Supplementary Methods S1 and S2. Tradeoffs among different terms of the hMRF model are governed by a set of hyperparameters. For a fixed set of hyperparameters, we used the alpha expansion algorithm to estimate the parcellation labels within a maximum-a-posteriori estimation framework (Delong et al., 2010), following our previous study (Schaefer et al., 2018). Details of the estimation procedure is found in Supplementary Methods S3 and S4. Supplementary Methods S5 provides details on how the hyperparameters are set in the following analyses.

2.4 Quantitative Evaluation Measures

Evaluating the quality of a human cerebral cortical parcellation is difficult due to a lack of ground truth. Motivated by the definition of a cortical area (Felleman and Van Essen, 1991), we considered four evaluation metrics utilized in previous parcellation studies (Glasser et al., 2016; Gordon et al., 2016; Gordon et al., 2017; Schaefer et al., 2018): architectonic alignment, visuotopic alignment, task functional inhomogeneity and resting-state connectional homogeneity. These evaluation metrics were utilized to compare hMRF parcellations with other public parcellations after controlling for the number of parcels (Section 2.5). A good parcellation should align well with known cytoarchitectonic and visuotopic boundaries, as well as have homogeneous function and connectivity.

2.4.1 Architectonic boundaries

Ten human architectonic areas were considered: 1, 2, 3 (areas 3a and 3b combined), 4 (areas 4a and 4p combined), 6, 17, 18 hOc5, 44, and 45 (Geyer et al., 1996, 1999, 2000, 2001; Amunts et al., 1999, 2000, 2004; Geyer 2004; Malikovic et al., 2007). These histological areas were projected to the fsLR surface template by Van Essen et al (2012a) based on Fischl et al (2008). To evaluate the alignment between these histological areas and the boundaries of a given parcellation, averaged geodesic distances were computed. In short, for each boundary vertex of an architectonic area, the geodesic distance to the nearest parcellation boundary was computed, then averaged across all boundary vertices of the area.

Lower geodesic distance indicated better alignment between histological and parcellation boundaries. When comparing two parcellations, paired-sample t-test of the geodesic distances from both hemispheres was used (degrees of freedom or dof = 19).

2.4.2 Visuotopic boundaries

Eighteen visuotopic areas were considered (Abdollahi et al., 2014). The areas were obtained by averaging individual fMRI visuotopic mapping in fsLR surface space after multimodal alignment (Abdollahi et al., 2014). Each visuotopic area generally occupied half of its true extent since it was difficult to stimulate the peripheral visual field (Hinds et al., 2009). Therefore, we only considered visuotopic boundaries between adjacent areas, yielding 46 pairs of adjacent areas across both hemispheres. The agreement between visuotopic areal boundaries and parcellation boundaries was quantified by computing the geodesic distance. For each visuotopic boundary vertex, the geodesic distance to the nearest parcellation boundary was computed. The geodesic distances were averaged across all boundary vertices of each pair of adjacent areas. Lower geodesic distance indicated better alignment between visuotopic and parcellation boundaries. When comparing two parcellations, paired-sample t-test of the geodesic distances was used (dof = 45).

2.4.3 Task functional inhomogeneity

Given a task activation contrast, the task functional inhomogeneity of a parcel was defined as the standard deviation (SD) of activation z-values across vertices within the parcel. The task functional inhomogeneities were combined across all parcels, yielding an overall task functional inhomogeneity metric (Gordon et al., 2017; Schaefer et al., 2018):

$$\frac{\sum_{l=1}^{L} SD_l * |l|}{\sum_{l=1}^{L} |l|},$$

where SD_l was the task functional inhomogeneity of the l-th parcel, $|l|$ indicated the number of vertices in parcel l and L was the total number of parcels. Therefore, larger parcels were weighted more in the overall task functional inhomogeneity metric. A lower task inhomogeneity metric indicated that activation within each parcel was more uniform, suggesting higher parcellation quality.

In this study, we utilized task contrasts from the HCP and ABCD datasets (Sections 2.2.2 and 2.2.3), which were in fsLR and fsaverage space respectively. For a given parcellation, task inhomogeneity was computed for each task contrast and each participant.

Task inhomogeneities were then averaged across all contrasts within each task. When comparing two parcellations for a given dataset, task inhomogeneities were further averaged across all tasks before applying the paired-sample t-test (dof = 955 for the HCP dataset and dof = 2261 for the ABCD dataset).

2.4.4 Resting-state connectional homogeneity

RSFC homogeneity was defined as the averaged Pearson's moment-product correlations between resting-fMRI time courses of all pairs of vertices (or voxels) within a given parcel. The correlations were then averaged across all parcels, while accounting for parcel size (Schaefer et al 2018; Kong et al 2021a):

$$\frac{\sum_{l=1}^{L} \rho_l * |l|}{\sum_{l=1}^{L} |l|},$$

where ρ_l was the averaged correlation within parcel l, $|l|$ indicated the number of vertices in parcel l and L was the total number of parcels. A higher resting-state homogeneity meant that vertices within a parcel shared more similar time courses. Therefore, a higher resting-state homogeneity indicated better parcellation quality.

Here, resting homogeneity was computed using (1) GSP test set in fsaverage space (N = 739), (2) HCP dataset in MNI152 volumetric space (N = 1030), (3) HCP dataset in fsLR space (N = 1030), (4) ABCD dataset in fsaverage space (N = 2262) and (5) GUSTO dataset in fsaverage space (N = 393). Therefore, the datasets spanned across multiple volume and surface coordinate systems. The GSP dataset consisted of participants aged 18 to 35, the HCP datasets consisted of participants aged 22 to 35, while the ABCD and GUSTO datasets comprised children aged 7 to 10 years old. Furthermore, while the GSP, HCP and ABCD datasets comprised largely white participants, the GUSTO comprised East Asian participants. Finally, the HCP dataset was processed using ICA-FIX, while the remaining datasets were processed with whole brain signal regression. The wide variety of datasets allowed us to evaluate the generalizability of the hMRF parcellations to new datasets in terms of resting-homogeneity.

To compare two parcellations for a given dataset, resting-state homogeneity was computed for each participant before a paired-sample t-test was performed (dof = 738 for GSP, dof = 1029 for HCP, dof = 2261 for ABCD and dof = 392 for GUSTO).

A cortical parcellation with more parcels will have smaller parcels, so will generally perform better on the resting homogeneity and task inhomogeneity metrics. A cortical parcellation with more parcels will also generally have lower architectonic and visuotopic geodesic distances. The reason is that more parcels will lead to more parcellation boundary vertices. Therefore, it is more likely that histological (or visuotopic) boundaries will lie closer to some parcellation boundary vertices. Overall, when assessing the above evaluation metrics, it is critical to control for the number of parcels (see next section).

2.5 Comparison with other parcellations

To evaluate the hMRF parcellations, we utilized the GSP training set (N = 740) to estimate a set of hMRF parcellations with different resolutions in fsaverage6 surface space. Details regarding the estimation procedure can be found in the Supplementary Methods. The resulting hMRF parcellations were compared with six public parcellations (Craddock et al., 2012; Shen et al., 2013; Joliot et al., 2015; Glasser et al., 2016; Gordon et al., 2016; Schaefer et al., 2018) using four evaluation metrics (Section 2.4). Five of these parcellations were generated with automatic algorithms from resting-fMRI data (Craddock et al., 2012; Shen et al., 2013; Joliot et al., 2015; Gordon et al., 2016; Schaefer et al., 2018). The remaining parcellation was generated from multimodal MRI data using a semi-automatic algorithm with inputs from an anatomist (Glasser et al., 2016).

Both the Glasser (Glasser et al., 2016) and AICHA (Joliot et al., 2015) parcellations were homotopic parcellations, while the remaining parcellations were non-homotopic. The Shen, Craddock and Schaefer parcellations are available in multiple resolutions. Given that there are estimated to be about 300 to 400 areas in the human cerebral cortex (Van Essen et al., 2012a), we chose the 400-region Craddock parcellation as a baseline. The most commonly used resolutions for the Shen and Schaefer parcellations were 268 and 400 parcels respectively, so they were chosen for comparison. Finally, the Gordon, Glasser and AICHA parcellations had 333, 360 and 384 parcels respectively.

For fair comparisons, there were several important issues to consider. First, the number of parcels had a strong influence on the evaluation metrics, so the hMRF parcellation procedure was run with different number of parcels to match the publicly available parcellations. Second, the Gordon parcellation included many unlabeled vertices near parcel boundaries and in low signal-to-noise regions, which artificially inflated the evaluation metrics. Therefore, when comparing with the Gordon parcellation, boundary vertices with the

worst resting homogeneity in the GSP training set were removed from the hMRF parcellation to match the number of unlabeled vertices in the Gordon parcellation.

Another issue is that different parcellations were developed in different coordinate systems. The Shen, Craddock, and AICHA parcellations were in MNI152 volumetric space. The Glasser and Gordon parcellations were in fsLR surface space. The Schaefer and hMRF parcellations were in fsaverage6 surface space. On the other hand, the data used for computing the evaluation metrics were also in different coordinate systems. Data used for computing architectonic and visuotopy metrics were in fsLR space. The GSP resting-fMRI data, GUSTO resting-fMRI data, ABCD resting-fMRI data and ABCD task-fMRI data were in fsaverage6 space. The HCP resting-fMRI data and task-fMRI data were in fsLR space. HCP resting-fMRI data was also available in MNI152 space.

To compute the evaluation metrics, a parcellation was transformed into the coordinate system where the evaluation data resided. For example, to compute task activation inhomogeneity using the ABCD task-fMRI data, the Shen, Craddock, AICHA, Glasser, and Gordon parcellations were transformed into fsaverage6 surface space. On the other hand, to evaluate architectonic or visuotopic geodesic distances, the Shen, Craddock, AICHA, Schaefer and hMRF parcellations were projected to fsLR surface space. The non-linear transformations between fsLR, fsaverage and MNI spaces are detailed elsewhere (Van Essen et al., 2012a; https://wiki.humanconnectome.org/display/PublicData/HCP+Users+FAQ; Wu et al., 2018).

The two issues (number of parcels and coordinate systems) were not independent, since transforming a parcellation from one space to another might change the number of parcels. For example, after projecting the Craddock parcellation from MNI152 to fsaverage or fsLR space, the number of parcels was reduced from 400 to 355. Furthermore, the coverage of the parcellations varied across different coordinate systems, so an intersection procedure was applied to pairs of parcellations to ensure that each pair covered the same portion of the cerebral cortex. The intersection procedure can further reduce the number of parcels. For example, after the application of the intersection procedure, the resolution of the Craddock parcellation in MNI152 space dropped to 346 parcels. In this case, we ran the hMRF procedure twice, with 346 and 355 parcels, to match the Craddock parcellations in volumetric and surface spaces respectively. In the case of the Shen parcellation, there were 268 and 197 parcels in volumetric and surface spaces respectively. Therefore, the hMRF procedure was run twice, with 268 and 197 parcels, to match the Shen parcellations in volumetric and surface spaces respectively.

For the Shen, Craddock and Gordon parcellations, the number of parcels were different between the two hemispheres, which was problematic since hMRF parcellations have equal number of parcels on both hemispheres. In the case of the Shen parcellation in fsaverage6 space, there were 100 parcels in the left hemisphere and 97 parcels in the right hemisphere. Therefore, we ran the hMRF parcellation procedure with 200 parcels. The right hemisphere of the hMRF parcellation has more parcels than the right hemisphere of the Shen parcellation. Therefore, a merging procedure was applied to merge parcels in the right hemisphere of the hMRF parcellation (in a way that maximizes resting-homogeneity in the GSP training set), resulting in 97 parcels in the right hemisphere. The same procedure was repeated for the Craddock and Gordon parcellations.

Finally, when mapping a parcellation from MNI152 to fsaverage space, the parcellation boundary tended to become rough, leading to lower resting-homogeneity. To reduce such bias, we smoothed the boundaries of the Shen, Craddock and AICHA parcellations after projecting them from MNI152 to fsaverage space. The resulting parcellations were visually appealing, but it is of course not possible to fully eliminate biases that arose from the mismatch between a parcellation's native coordinate system and the space in which the evaluation metrics was computed. For example, the Glasser parcellation (whose native space was fsLR) had inherent advantage over the hMRF parcellation (whose native space was fsaverage6) when computing resting-state homogeneity with the HCP resting-fMRI data in fsLR space.

2.6 Cerebral cortical parcellations of 1479 participants and further characterization

The previous analyses served to compare the hMRF parcellations with other existing parcellations. To provide a final set of parcellations for the community, the hMRF parcellation procedure was finally applied to the full GSP dataset (N = 1479). Details regarding the hyperparameter settings can be found in Supplementary Methods S5. Since a single parcellation resolution was unlikely to be optimal across all applications, we generated parcellations (in the fsaverage6 surface space) from 100 to 1000 parcels in intervals of 100 parcels. The parcellations were also projected to fsLR and MNI152 spaces. To visualize the resulting parcellations, we assigned each parcel to one of 7 or 17 networks based on maximal spatial overlap with the Yeo networks (Yeo et al., 2011).

Since the Yeo networks were asymmetric, homotopic parcels in the hMRF parcellations could be assigned to different networks. We further characterized this phenomenon for the 400-region hMRF parcellation by computing RSFC between homotopic

pairs of parcels. We hypothesized that homotopic parcels with different network assignments would exhibit weaker homotopic RSFC. Spatial overlap (Dice coefficient) for each pair of homotopic parcels was also computed based on our established cross-hemispheric vertex-level correspondence. More specifically, for each pair of homotopic parcels, we divided the total number of spatially homotopic vertices shared between both parcels by the total number of vertices enclosed in both parcels.

We also investigated the relationship between homotopic RSFC and task activation lateralization in the HCP dataset. More specifically, we considered the "story – math" contrast from the language, as well as task contrasts (tongue – average, left fingers – average, right fingers – average, right foot – average, left foot – average) from the motor task. For each activation contrast, we averaged the activation z values within each parcel of the 400-region hMRF parcellation. For each contrast and each homotopic parcel pair, an activation laterality index was defined as the absolute difference between left parcel activation and right parcel activation. Activation laterality was only computed for parcels strongly activated by the task contrast. We defined strongly activated parcels (of a particular task contrast) as those parcels whose average activation was at least 70% of the parcel with the largest average activation. In the case of the motor task, we averaged the activation laterality indices across the five contrasts, yielding a single activation laterality map for the motor task.

Finally, we further characterized the 400-region hMRF parcellation by overlaying the boundaries of histological areas and visuotopical cortical areas. Visual inspection was then performed to explore the agreement between the hMRF parcellation and cortical areal boundaries.

2.7 Data and code availability

Code for the hMRF model can be found here (GITHUB_LINK). Co-authors (RK, AX and LA) reviewed the code before merging into the GitHub repository to reduce the chance of coding errors. Multi-resolution hMRF parcellations generated from 1489 participants are publicly available (GITHUB_LINK).

The HCP preprocessing code can be found here (GITHUB_LINK). The remaining datasets utilized the CBIG preprocessing pipeline (https://github.com/ThomasYeoLab/CBIG/tree/master/stable_projects/preprocessing/CBIG_fMRI_Preproc2016). The datasets were processed by different researchers, so the pipeline was run with slightly different parameters (as reported in Section 2.2).

The GSP (http://neuroinformatics.harvard.edu/gsp/), HCP (https://www.humanconnectome.org/) and ABCD (https://nda.nih.gov/abcd/) datasets are publicly available. The GUSTO dataset can be obtained via a data transfer agreement (https://www.gusto.sg/).

3 Results

3.1 Homotopic differences between hMRF and gwMRF parcellations within area 17

Figure 1 overlays the boundaries of histologically-defined architectonic area 17 (Amunts et al., 1999) on the 400-region parcellations generated by gwMRF and hMRF. Both parcellations agree well with area 17 boundary. However, the gwMRF parcellation subdivided left area 17 into three parcels and right area 17 into two parcels (Figure 1B). On the other hand, the hMRF parcellation subdivided left and right areas 17 into equal number of parcels with similar spatial topography across the two hemispheres, consistent with the fact that area 17 is not known to be asymmetric.

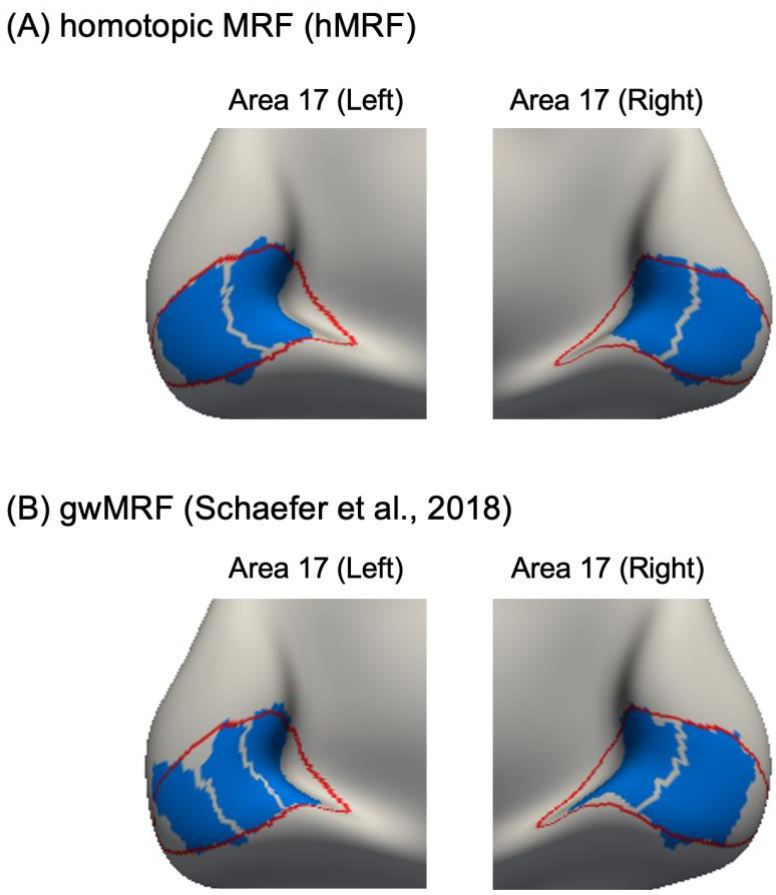

Figure 1. Difference in homotopic correspondence between hMRF and gwMRF parcellations within histologically-defined area 17. (A) Parcels (blue) of the 400-region hMRF parcellation within histological (red) boundaries of area 17. The hMRF parcellation subdivided left and right areas 17 into equal number of parcels with similar spatial topography across the two hemispheres. (B) Parcels (blue) of the 400-region gwMRF parcellation within histological (red) boundaries of area 17. The gwMRF parcellation subdivided left area 17 into three parcels and right area 17 into two parcels.

3.2 Architectonic alignment

Figure S1 shows the geodesic distances between the boundaries of 10 histologically-defined architectonic areas and six publicly available parcellations. Geodesic distances between the architectonic areas and hMRF parcellations are also shown. Number of parcels was matched between the publicly available parcellations and corresponding hMRF parcellations. Lower distance indicates better alignment.

Across the 10 architectonic areas, the hMRF approach generated parcellations with similar architectonic distance as Shen ($p = 0.441$), better distance than Gordon ($p \approx 0$), similar distance to AICHA ($p = 0.210$), better distance than Craddock ($p = 0.031$), worse distance than Glasser ($p = 0.032$), and similar distance to Schaefer ($p = 0.835$).

After correcting for multiple comparisons with a false discovery rate (FDR) of $q < 0.05$, only the comparison with the Gordon parcellation remained significant. Overall, the hMRF parcellations exhibited architectonic alignment comparable with (or better than) other parcellations.

3.3 Visuotopic alignment

Figures S2 show the geodesic distances between the boundaries of 18 visuotopic areas (Abdollahi et al., 2014) and six publicly available parcellations. Geodesic distances between the visuotopic areas and hMRF parcellations are also shown. Number of parcels was matched between the publicly available parcellations and corresponding hMRF parcellations. Lower distance indicates better alignment.

Across the 18 visuotopic areas, the hMRF parcellations achieved similar visuotopic distance to Shen ($p = 0.279$), better distance to Gordon ($p \approx 0$), similar distance to ACIHA ($p = 0.731$), similar distance to Craddock ($p = 0.989$), worse distance to Glasser ($p \approx 0$) and similar distance to Schaefer ($p = 0.083$).

After correcting for multiple comparisons with an FDR of $q < 0.05$, the comparisons with the Gordon and Glasser parcellations remained significant. We note that the Glasser parcellation was derived with a semi-automated algorithm that required an anatomist to manually select multi-modal information to match prior knowledge of areal boundaries. Overall, the hMRF parcellations achieved visuotopic alignment comparable with (or better than) other fully automatic approaches.

3.4 Task-fMRI activation inhomogeneity

Figure 2 compares the task inhomogeneity of the hMRF parcellations with six publicly available parcellations using the HCP task-fMRI data. A lower task inhomogeneity indicated higher parcellation quality. Task inhomogeneity was not comparable between parcellations of different resolutions, so the number of parcels was matched between the publicly available parcellations and corresponding hMRF parcellations.

In the HCP dataset (Figure 2), the hMRF parcellations exhibited lower (better) task inhomogeneity than the Shen (average 2.4%; $p \approx 0$), Gordon (average 5.6%; $p \approx 0$), AICHA (average 2.1%; $p \approx 0$), Craddock (average 2.4%; $p \approx 0$), Glasser (average 2.9%; $p \approx 0$) and Schaefer (average 0.06%; $p = 3.0e-17$) parcellations. It is worth mentioning that the Glasser parcellation was partially derived using task-fMRI data from the HCP dataset, so should have an inherent advantage in this metric.

Figure 3 compares the task inhomogeneity of the hMRF parcellations with six publicly available parcellations using the ABCD task-fMRI data. The hMRF parcellations exhibited lower (better) task inhomogeneity than the Shen (average 1.5%, $p \approx 0$), Gordon (average 4.9%; $p \approx 0$), AICHA (average 2.0%; $p \approx 0$), Craddock (average 1.8%; $p \approx 0$) and Glasser (average 4.0%; $p \approx 0$) parcellations. On the other hand, the hMRF parcellations exhibited higher (worse) task inhomogeneity than the Schaefer parcellation (average 0.02%; $p = 4.9e-08$).

Overall, the hMRF parcellations exhibited comparable task inhomogeneity with the Schaefer parcellation and better task inhomogeneity than the other five parcellations. More specifically, differences between hMRF and Schaefer parcellations were less than 0.1%, which was an order of magnitude smaller than the differences between hMRF and other parcellations.

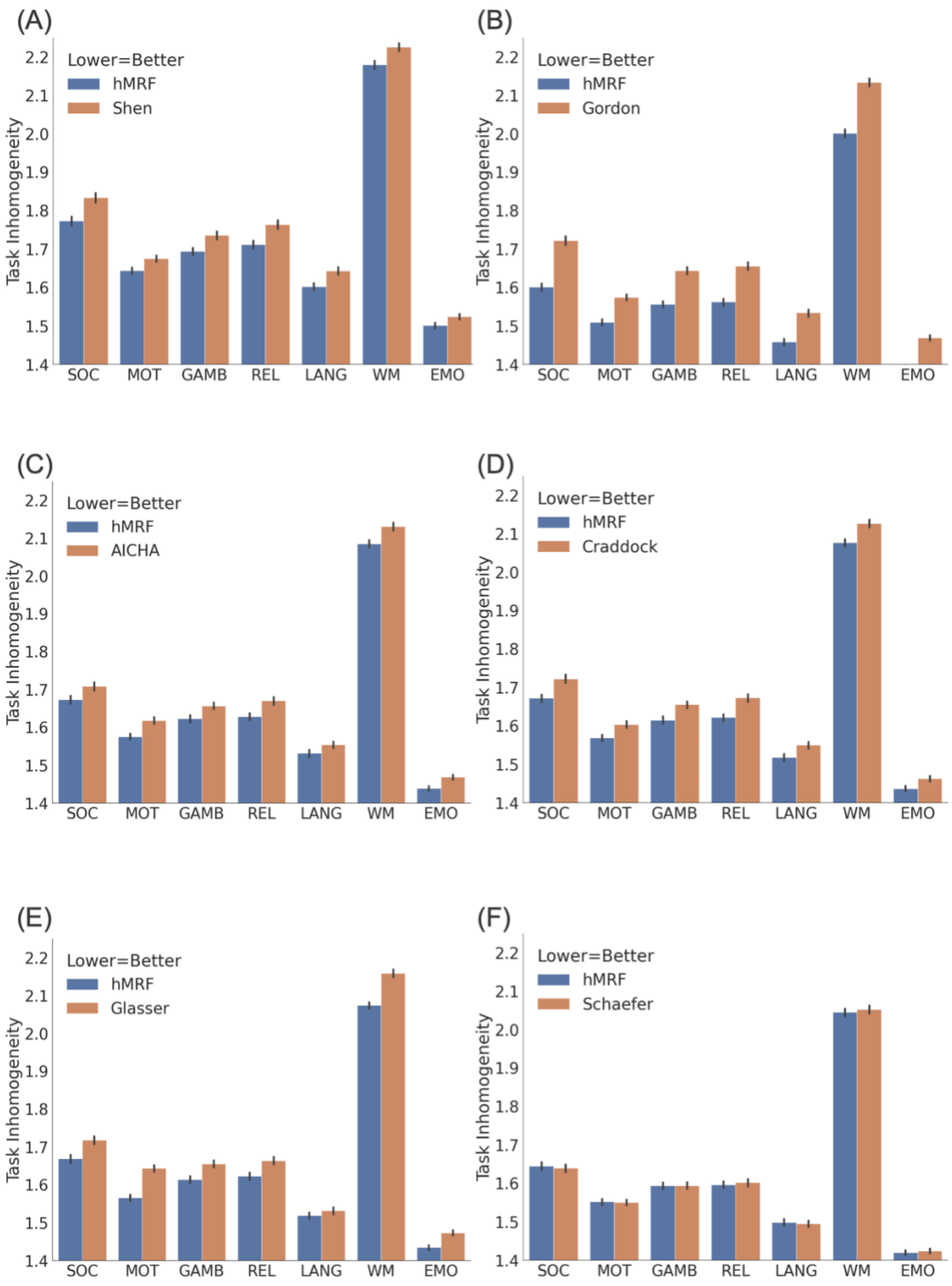

Figure 2. Task inhomogeneity computed from task-fMRI data in the HCP dataset (N = 1030). Lower task inhomogeneity indicates better parcellation quality. We note that task inhomogeneity cannot be compared across the panels because of the different number of parcels across panels. The hMRF parcellations exhibited comparable task inhomogeneity with the Schaefer parcellation and better task inhomogeneity than all other parcellations.

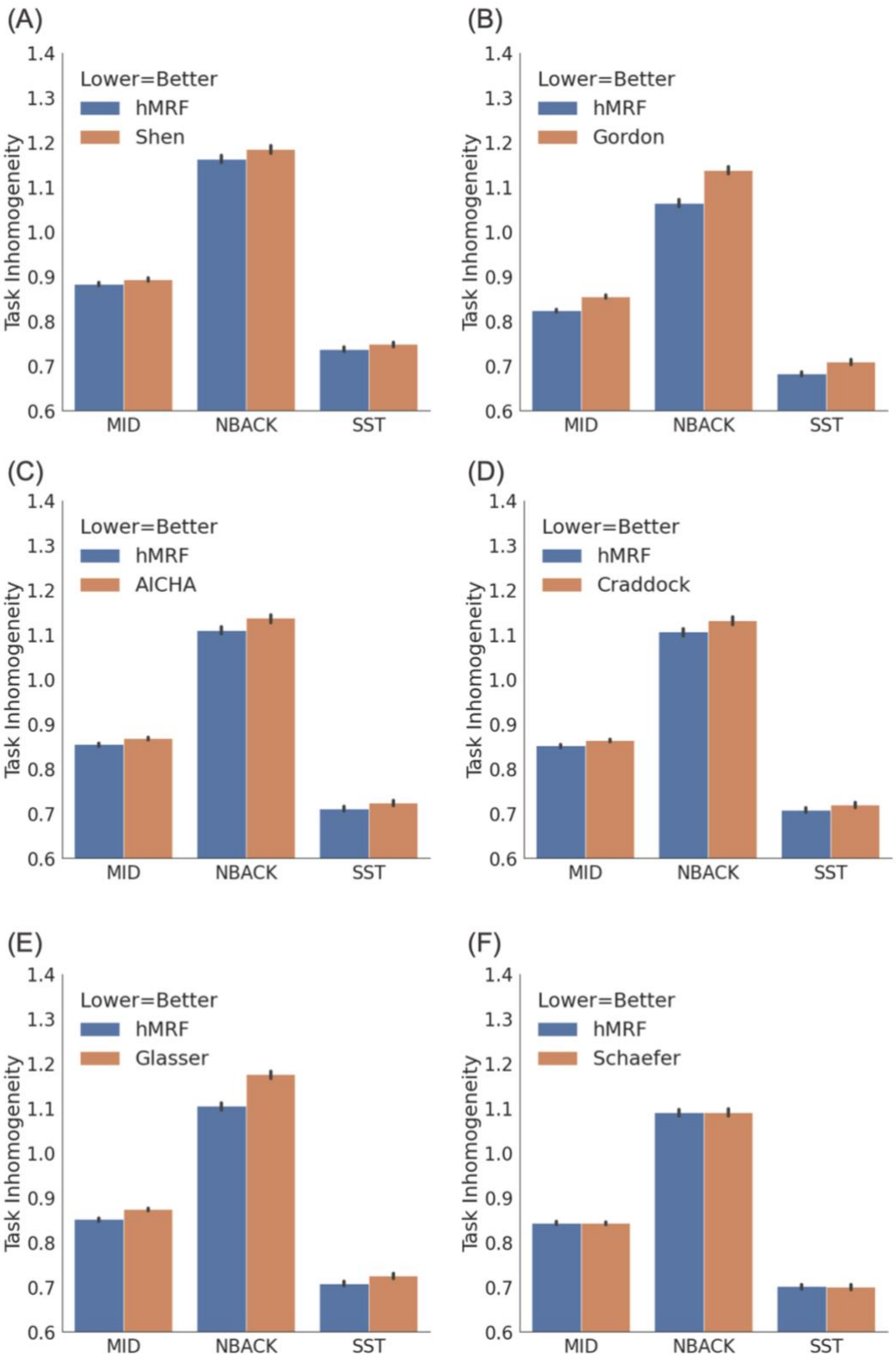

Figure 3. Task inhomogeneity computed from task-fMRI data in the ABCD dataset (N = 2262). Lower task inhomogeneity indicates better parcellation quality. We note that task inhomogeneity cannot be compared across the panels because of the different number of parcels across panels. The hMRF parcellations exhibited comparable task inhomogeneity with the Schaefer parcellation and better task inhomogeneity than all other parcellations.

3.5 Resting-fMRI homogeneity.

Figures 4 and S3 compare the hMRF parcellations with 6 publicly available parcellations in terms of resting-fMRI homogeneity across a variety of datasets. Higher resting-fMRI homogeneity indicated higher parcellation quality. Resting-fMRI homogeneity was not comparable between parcellations of different resolutions, so the number of parcels was matched between the publicly available parcellations and corresponding hMRF parcellations.

The hMRF parcellations were significantly more homogeneous across all five datasets than the Shen (average 6.6%, $p < 7.7e-37$), Gordon (average 11.5%, $p \approx 0$), AICHA (average 6.6%, $p \approx 0$), Craddock (average 5.5%, $p < 9.8e-324$), and Glasser (average 9.0%, $p < 9.5e-284$) parcellations. As noted above, the Glasser parcellation was partially derived from the HCP resting-fMRI data, so should have an inherent advantage in the HCP dataset. On the other hand, the hMRF and Schaefer parcellations were comparable with mean difference of 0.11% across all datasets.

A parcellation with higher number of parcels should result in higher resting-fMRI homogeneity. However, we note that the 333-region Gordon parcellation exhibited higher resting-fMRI homogeneity than other parcellations of higher resolutions (e.g., Glasser parcellation). The reason is that the Gordon parcellation unlabeled vertices at the boundaries between parcels and in low signal-to-noise regions, which artificially boosted its homogeneity. Similarly, when generating hMRF parcellation for comparison with the Gordon parcellation, we unlabeled the same number of vertices as the Gordon parcellation, which boosted our resting-fMRI homogeneity.

Finally, we note that the resting-fMRI homogeneity was much lower in the HCP dataset compared with the GSP and ABCD datasets. A major reason is that the HCP dataset was smoothed with a 2mm FWHM, while the GSP and ABCD datasets were smoothed with a 6mm FWHM. In general, greater spatial smoothing should yield higher resting-fMRI homogeneity (on average).

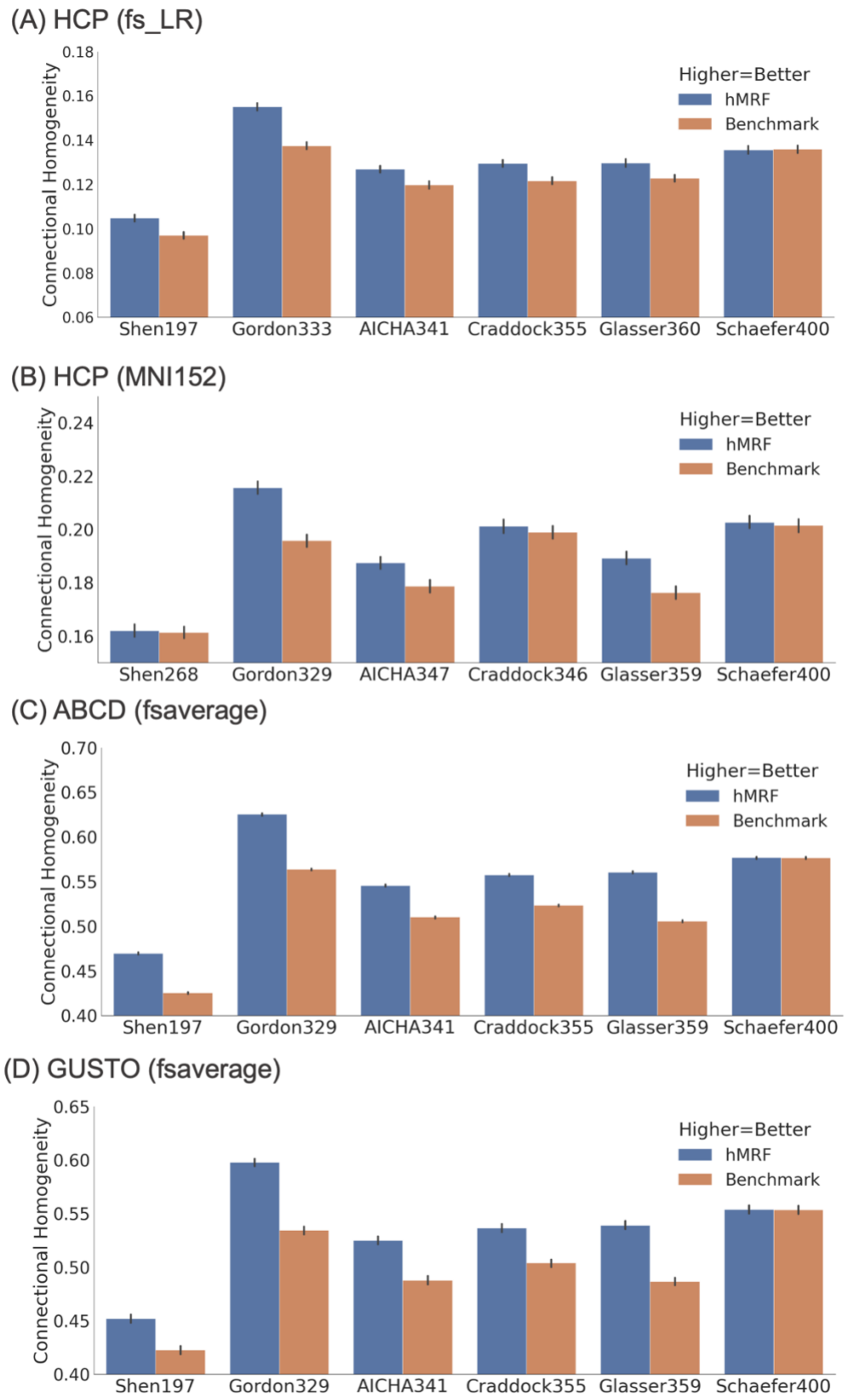

Figure 4. Resting-fMRI homogeneity computed with the (A) ABCD dataset (N = 2262) in fsaverage space, (B) HCP dataset (N = 1030) in fsLR space, (C) HCP dataset (N = 1030) in MNI152 space, and (D) GUSTO dataset (N = 393) in fsaverage space. The hMRF

parcellations achieved comparable resting-fMRI homogeneity with the Schaefer parcellation. On the other hand, the hMRF parcellations were more homogeneous than 5 parcellations across all 4 data sets. Resting-fMRI homogeneity in the GSP test set is shown in Figure S3.

3.6 RSFC lateralization of hMRF parcellations estimated from 1479 Participants

Cerebral parcellations at multiple resolutions, from 100 to 1000 parcel at every 100-parcel interval, were generated from the full GSP dataset (N = 1479) and visualized in Figure S4. The first row of Figure 5 shows the Yeo 7-network and 17-network parcellations (Yeo et al., 2011). The second row of Figure 5 shows the 400-region hMRF parcellation, where the color of each parcel was assigned based on maximal spatial overlap with the Yeo networks. Network assignment for parcellations of other resolutions are shown in Figure S5.

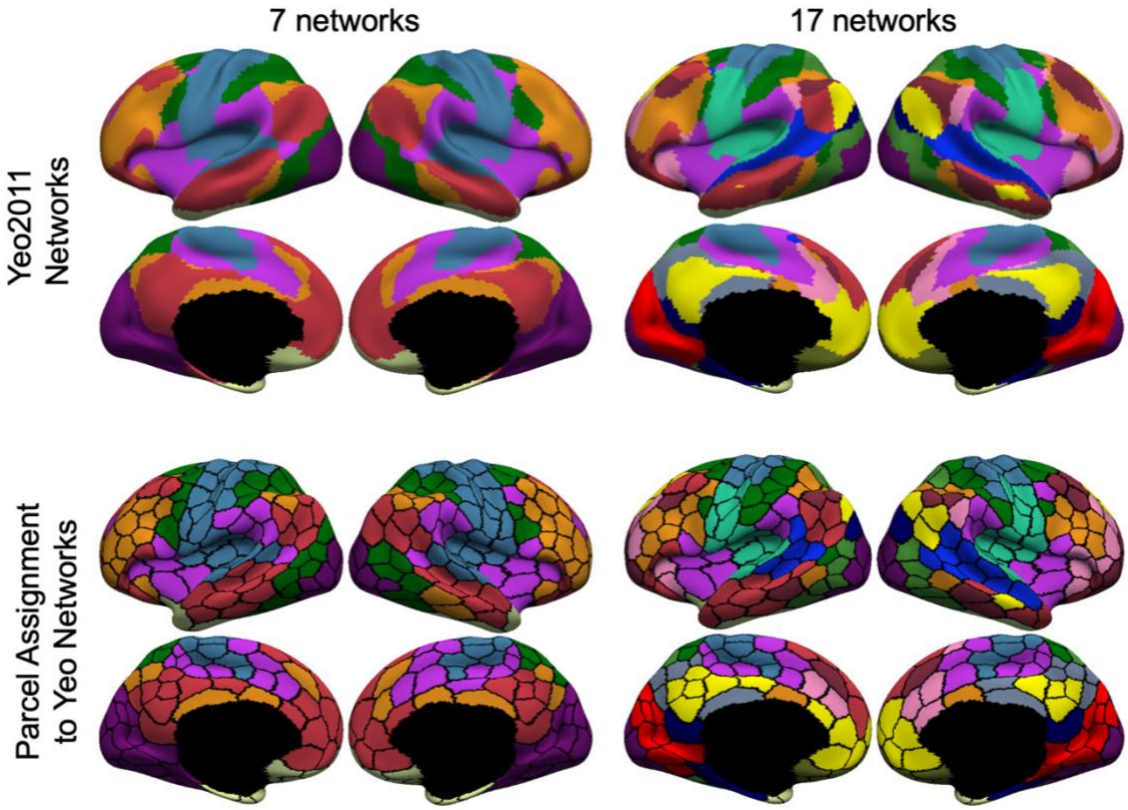

Figure 5. Assignment of parcels to 7 or 17 networks for hMRF parcellations with 400 regions. First row shows the Yeo 7 and 17 networks (Yeo et al., 2011). Second row shows the 400-region hMRF parcellation with each parcel assigned a network color based on its spatial overlap with the 7-network or 17-network parcellation.

Some of the Yeo networks were clearly asymmetric across the hemispheres. For example, the frontoparietal control network (orange network in the first column of Figure 5)

was larger in the right lateral prefrontal cortex than in the left lateral prefrontal cortex. This lateralization difference translated to the network assignment of the hMRF parcellations. Figure 6A shows the 7-network assignment of the 400-region hMRF parcellation with black arrows indicating a pair of homotopic parcels assigned to different networks. The left parcel was assigned to the default network, while the right parcel was assigned to the frontoparietal control network.

Figure 6B shows the RSFC between homotopic pairs of parcels in the 400-region hMRF parcellation in the GSP dataset. As indicated by the black arrows, the homotopic parcels with different network assignment shown in Figure 6A, also exhibited weaker RSFC compared to the rest of the cerebral cortex. This phenomenon is further quantified in Figure 6C, which shows that homotopic parcel pairs assigned to the same networks exhibited stronger RSFC than homotopic parcel pairs assigned to different networks ($p = 3.72e-4$ for 7-network assignment and $p = 0.0028$ for 17-network assignment). Therefore, lateralization differences in the spatial topography of the Yeo networks were reflected in the strength of RSFC between homotopic parcels.

Another clear observation was that sensory-motor parcels showed stronger homotopic RSFC (Figure 6B), while association parcels showed weaker RSFC, consistent with previous studies (Stark et al., 2008; Zuo et al., 2010). Finally, Figure 6D shows the degree of spatial overlap (as measured by the Dice coefficient on the fsaverage6 surface) between homotopic pair of parcels. The degree of spatial overlap varied across the cortex with no clear pattern. There was almost no correlation between the spatial overlap (Figure 6D) and RSFC (Figure 6B) of homotopic parcel pairs ($r = 0.20$). In other words, homotopic parcel pairs with greater spatial overlap did not necessarily have stronger or weaker homotopic RSFC.

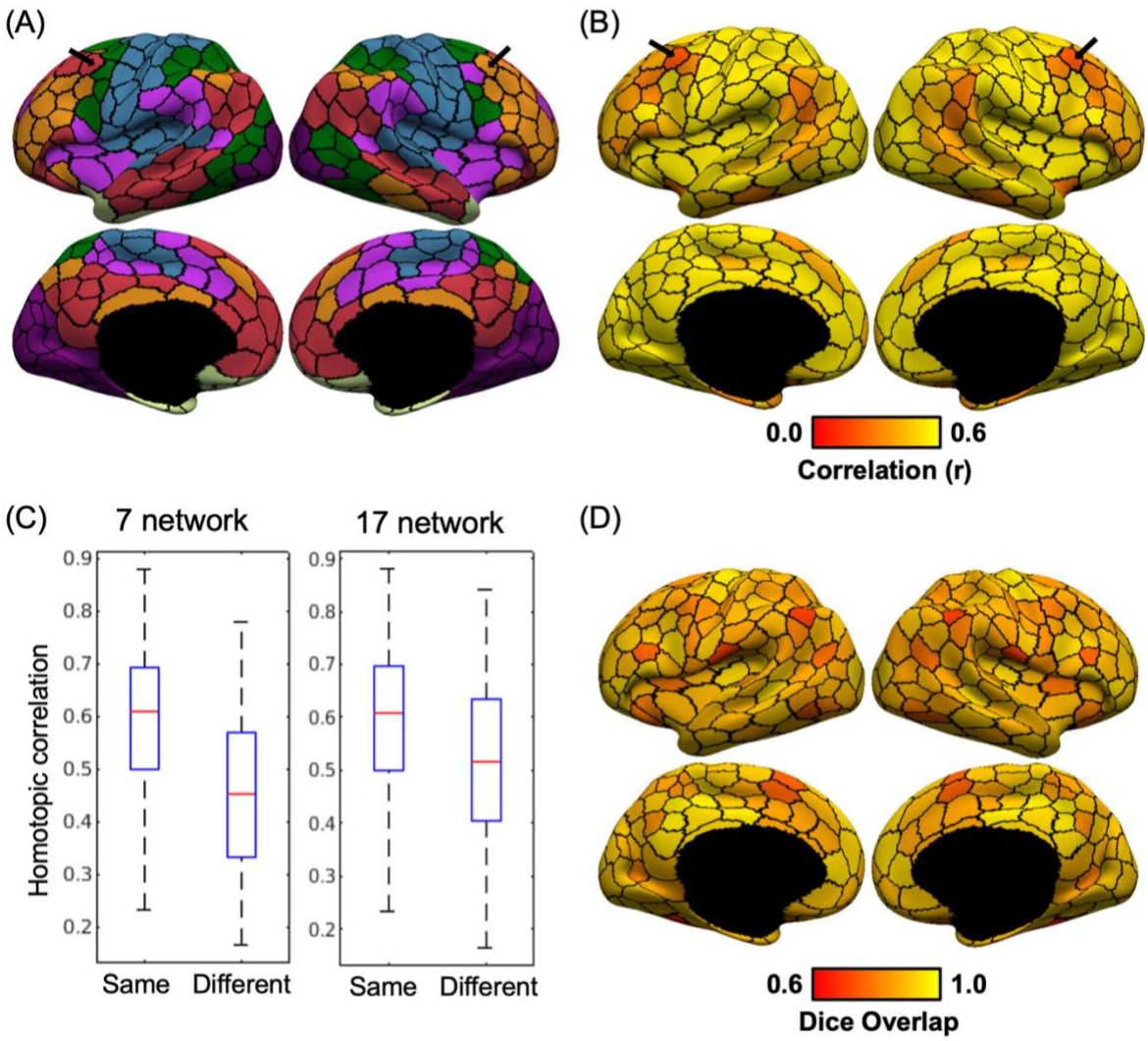

Figure 6. RSFC lateralization of the 400-region hMRF parcellation. (A) Lateralization in network assignment of the 400-region hMRF parcellation. Black arrows indicate a homotopic pair of regions assigned to two different networks from the Yeo 7-network parcellation. (B) RSFC between homotopic pairs of parcels in the GSP dataset. Black arrows indicate that the homotopic pair of parcels highlighted in panel A exhibited weaker RSFC with each other (i.e., homotopic correlation) compared with other homotopic parcel pairs. (C) Boxplot of RSFC between homotopic parcel pairs assigned to the same or different networks for both 7-network and 17-network assignments. Homotopic parcel pairs assigned to the same network exhibited stronger RSFC than homotopic parcel pairs assigned to different networks. (D) Spatial overlap (as measured by Dice coefficient) between homotopic pairs of parcels.

3.7 Task activation lateralization of the 400-region hMRF parcellation

Figures S6 to S10 show the HCP task contrasts overlaid on the 400-region hMRF parcellation boundaries. Consistent with previous parcellations (e.g., Schaefer et al., 2018), task activations were highly distributed across the cortex, cutting across multiple parcellation

boundaries. This is expected given that a single task contrast involves multiple cognitive processes supported by multiple cortical areas (Poldrack 2006; Barrett and Satpute 2013; Yeo et al., 2015).

Figure 7A shows the unthresholded "story – math" language task contrast, in which activation z values were averaged within each of the 400-region hMRF parcels. Figure 7B shows the task activation laterality index defined as the absolute difference between right hemisphere and left hemisphere activation values. This laterality index was only computed for parcels whose average activation-z values were at least 70% of the most activated parcel. Figure 7C shows the RSFC between homotopic pairs of parcels in the HCP dataset. Because the HCP dataset exhibited a strong posterior-to-anterior SNR gradient (Figure S11), the SNR map was regressed from the raw homotopic correlations (Figure 7D). We note that this SNR gradient was absent in the GSP dataset (see Figure 3 of Yeo et al., 2011), so a similar regression was not performed in the GSP dataset (Figure 6B).

We hypothesized that homotopic parcels with greater task activation laterality also exhibited weaker homotopic correlations. This hypothesis was confirmed by the data: correlation between language task activation laterality (Figure 7B) and SNR-regressed homotopic correlation (Figure 7D) was negative ($r = -0.76$; spin test $p = 0.012$). Similar results were obtained with the motor task (Figure 8). As expected, finger and foot activations were lateralized while the tongue activation was bilateral (Figure 8F). Correlation between motor task activation laterality (Figure 8F) and SNR-regressed homotopic correlation (Figure 7D) was negative ($r = -0.83$; spin test $p = 0.028$). Similar results were also obtained with different activation thresholds (Figure S12).

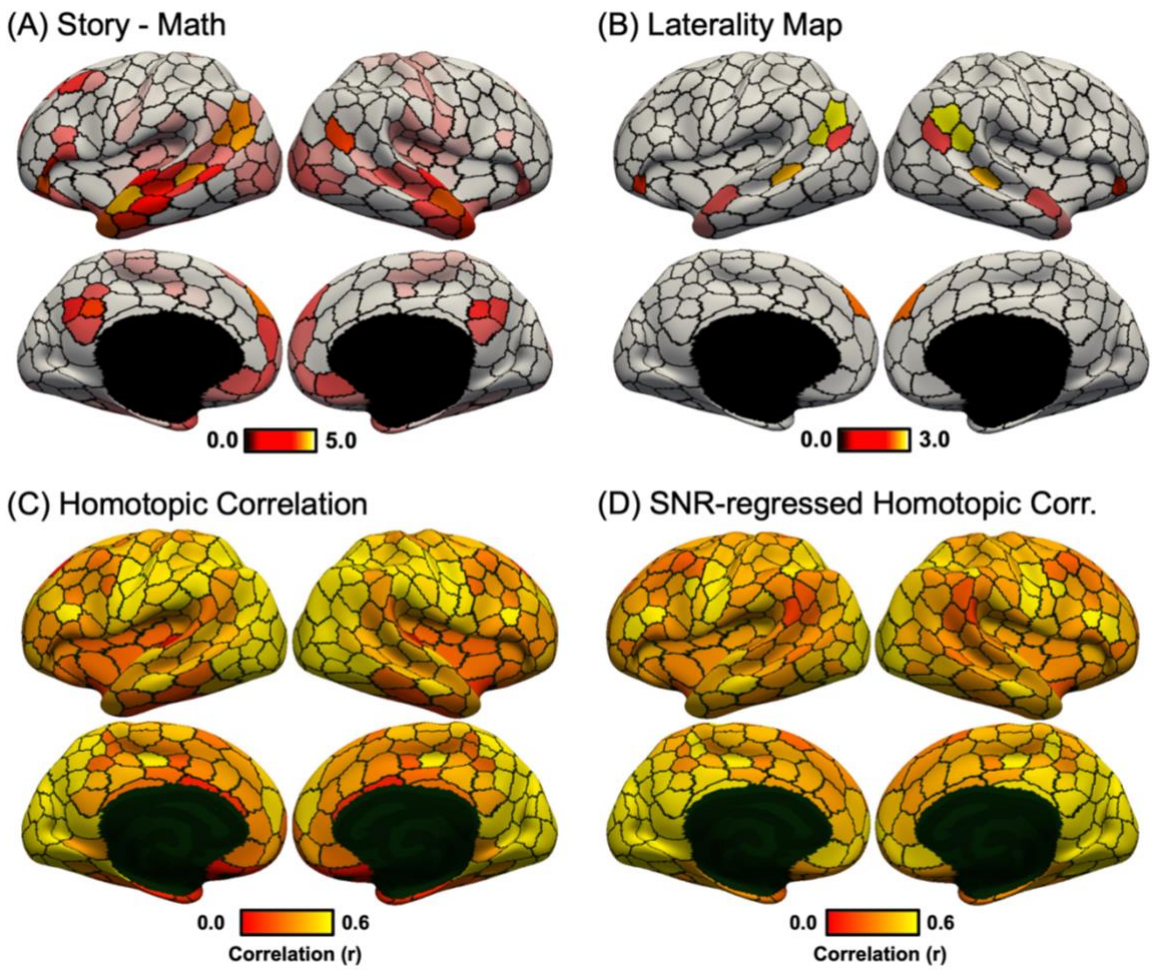

Figure 7. Language task activation lateralization in the HCP dataset. (A) Group-average "story – math" language task contrast in the HCP dataset. Activation z values were averaged within each of the 400-region hMRF cortical parcellation (shown as black boundaries). (B) Group-average task laterality map defined as the absolute difference between left and right hemisphere activation values. Laterality was only computed for parcels whose average activations were at least 70% of the most activated parcel. Laterality maps for alternative thresholds can be found in Figure S12. (C) RSFC between homotopic pairs of parcels in the HCP dataset. (D) RSFC between homotopic pairs of parcels in the HCP dataset after regressing HCP SNR map (Figure S11). There was a negative correlation between task activation laterality (Figure 7B) and SNR-regressed homotopic correlations (Figure 7D).

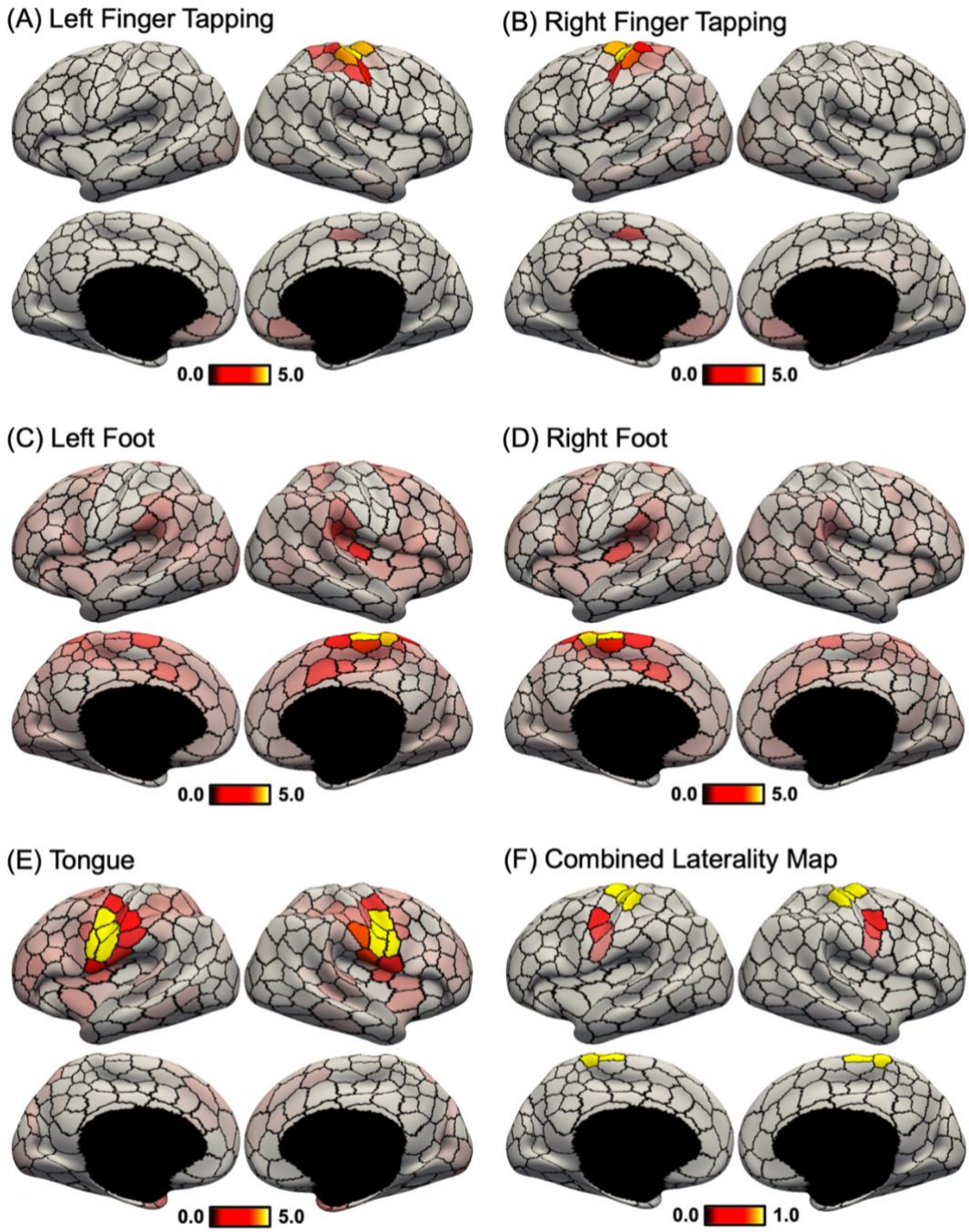

Figure 8. Motor task activation lateralization in the HCP dataset. (A) Group-average "left finger – average" motor task contrast. Activation z values were averaged within each of the 400-region hMRF cortical parcellation (shown as black boundaries). (B) Group-average "right finger – average" motor task contrast. (C) Group-average "left foot – average" motor task contrast. (D) Group-average "right foot – average" motor task contrast. (E) Group-average "tongue – average" motor task contrast. (F) Task laterality map averaged across the five contrasts. Similar to Figure 7, task laterality was defined as the absolute difference between left and right hemisphere activation values. Laterality was only computed for parcels whose average activations were at least 70% of the most activated parcel. Laterality maps for alternative thresholds can be found in Figure S12. There was a negative correlation between task activation laterality (Figure 8F) and SNR-regressed homotopic correlations (Figure 7D).

3.8 Comparison of 400-region hMRF parcellation with architectonic and visuotopic areas

Figure 9 shows the 400-region hMRF parcellation (estimated from the full GSP dataset) overlaid with boundaries of architectonic areas 3, 4, 2, hOc5, and 17 on the right cortical hemisphere (Fischl et al., 2008; Van Essen et al., 2012a). Figures for other architectonic areas as well as those on the left hemisphere are shown in Figure S13.

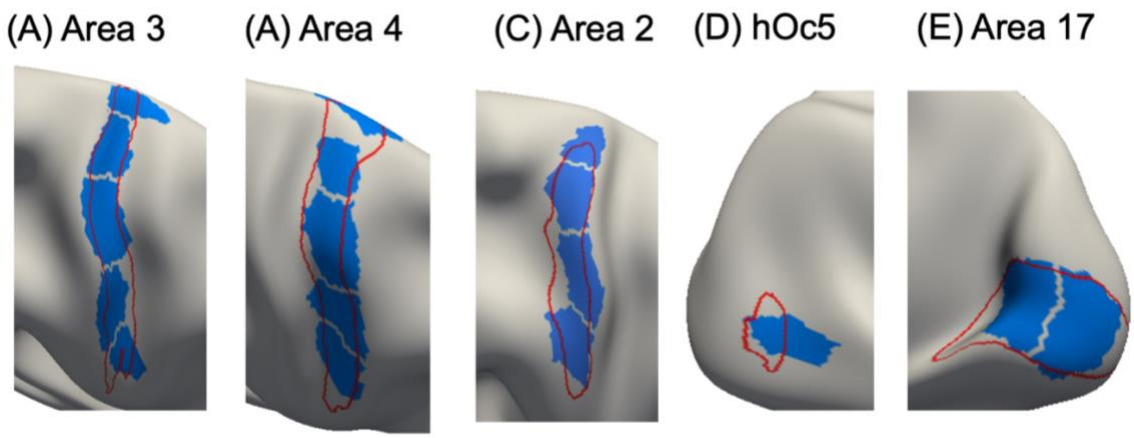

Figure 9. Parcels (blue) of the 400-region hMRF parcellation overlaid on histological (red) boundaries of right hemisphere (A) area 3, (B) area 4, (C) area 2, (D) hOc5, and (E) area 17. Other histological areas are shown in Figure S13.

The parcels corresponded well with the histological boundaries (Figure 9). However, consistent with previous studies, the parcellation also seemed to fractionate each area into multiple subunits. Within areas 3, 4, and 2, the fractionated parcels might correspond to somatotopic representations of different body parts. Parcels within primary area 17 appeared to fractionate the eccentricity axis. Area 44 was captured well by the parcellation on both hemispheres (Figure S13).

For other areas, the alignment between the parcels and areal boundaries was less precise. The parcels overlapping with area 18 aligned well with the boundary between areas 18 and 17, but tended to extend beyond the boundary between areas 18 and 19. The parcellation was not able to capture area 1 boundary, which was long and thin. Area 45 maximally overlapped with two hMRF parcels on each hemisphere. For area 6, the alignment between the parcels and areal boundary on the left hemisphere was more precise than on the right hemisphere.

Figure S14 overlays the 400-region parcellation boundary on 18 visuotopically mapped areas (Adollahi et al., 2014). The parcels overlapping with visuotopically-defined V1 (which is known to correspond to architectonic area 17) were in good agreement with V1 boundaries. For other visuotopic areas, correspondence was more muted. The parcels might fractionate higher order visuotopic areas based on eccentricity, similar to the fractionation within V1.

4 Discussion

In this study, we extended the gwMRF model to derive an atlas of homotopic parcels. Compared with the original gwMRF parcellation (Schaefer et al., 2018), the resulting hMRF parcellation exhibited similar alignment to architectonic and visuotopic boundaries, as well as similar task-state inhomogeneity and resting-state homogeneity. Furthermore, the hMRF parcellations exhibited better task inhomogeneity and resting homogeneity than five publicly available parcellations (Craddock et al., 2012; Shen et al., 2013; Joliot et al., 2015; Glasser et al., 2016; Gordon et al., 2016). Consistent with previous studies, we found that weaker correlations between homotopic parcels were associated with greater lateralization in resting network organization, as well as greater lateralization in language and motor task activation. Overall, we believe the hMRF parcellations will be a useful resource for future studies.

4.1 Interpretation and potential applications of the hMRF parcellations

Histological studies have generally found pairs of cortical areas in roughly spatially homotopic locations across the left and right hemispheres (Amunts et al., 2020). In fact, many histological studies simply report cortical areas on one hemisphere with the strong implicit assumption that homotopic cortical areas exist on the other hemisphere (e.g., Petrides and Pandya, 1999). However, it is important to note that homotopic areas do not necessarily have the same function as demonstrated by well-known lateralization of brain activation during language tasks (Malik-Moraleda et al., 2022)

Similar functional lateralization was also observed for the 400-region hMRF parcellation during both resting and task states. For example, a number of homotopic parcels overlapped with different large-scale resting-state networks (Yeo et al., 2011). Homotopic parcel pairs assigned to the same network exhibited stronger RSFC than homotopic parcel pairs assigned to different networks (Figure 6C). Sensory-motor parcels also exhibited stronger homotopic correlations than association parcels in both GSP (Figure 6B) and HCP (Figures 7D) datasets, consistent with previous studies of homotopic correlations (Stark et al., 2008; Zuo et al., 2010).

A potential mechanism for the observed sensory-association gradient in homotopic correlations is that sensory-motor regions are connected by thickly myelinated fast conducting callosal fibers, while association regions are connected by thinly myelinated slow conducting callosal fibers (LaMantia and Rakic, 1990; Aboitiz et al., 1992). However, we note that these fibers cannot fully explain the strong inter-hemispheric coupling in early visual regions given that callosal fibers terminate preferentially in regions representing the

vertical midline of the visual field (Van Essen and Zeki, 1978; Van Essen et al., 1982). Instead, homotopic correlations (and RSFC in general) are mediated by indirect synaptic coupling (Vincent et al., 2007; Stark et al., 2008; Lu et al., 2011; Xue et al., 2021).

Previous studies (e.g., Yeo et al., 2011) have demonstrated that somatomotor regions representing distal limbs (e.g., hand and foot) exhibited stronger homotopic correlations than somatomotor regions representing midline regions (e.g., tongue), which is consistent with non-human primate studies showing denser callosal fibers connecting regions representing midline structures (Pandya and Vignolo 1971; Jones and Wise 1977; Killackey et al., 1983; Gould et al., 1986). It is also well-known that finger or foot movements activate contralateral somatomotor regions while tongue movements activate bilateral tongue regions (Ehrsson et al., 2003). Therefore, it is perhaps not surprising that homotopic parcels exhibiting stronger laterality during the motor task also exhibited weaker homotopic correlations (Figure 8). Similar results were obtained during the language task: homotopic parcels exhibiting stronger laterality during the language task also exhibited weaker homotopic correlations (Figure 7).

Overall, the hMRF parcels replicated well-known homotopic properties of the cerebral cortex during resting and task states. Given that the hMRF parcellations were more homogeneous than the other two homotopic parcellations (Joliot et al., 2015; Glasser et al., 2016) during resting and task states, we expect the hMRF parcellations to be a useful dimensionality reduction tool for future brain lateralization studies in health and disease. Furthermore, hMRF and Schaefer parcellations exhibit highly matched properties in terms of architectonic alignment, visuotopic alignment, task inhomogeneity and resting homogeneity. Therefore, the hMRF parcellations can also be utilized in studies of brain organization unrelated to lateralization.

4.2 hMRF parcels align with cortical areal boundaries

The local gradient approach for parcellating the cerebral cortex detects abrupt changes in RSFC patterns (Cohen et al., 2008; Laumann et al., 2015; Gordon et al., 2016). On the other hand, the global similarity approach clusters voxels (or vertices) with similar functional connectivity patterns (van den Heuvel et al., 2008; Power et al., 2011; Yeo et al., 2011; Ryali et al., 2013; Gordon et al., 2017). Studies have suggested that the local gradient approach can detect certain areal boundaries not revealed by the global similarity approach (Wig et al., 2014; Buckner and Yeo, 2014).

We previously proposed the gwMRF model to integrate local and global parcellation approaches (Schaefer et al., 2018). The resulting 400-region Schaefer parcellation aligned

well with certain areal boundaries, while exhibiting excellent resting homogeneity and task inhomogeneity. In the current study, the proposed hMRF model extended the gwMRF model by encouraging homotopic parcels. One concern was that the additional homotopic constraint might lead to parcellations with worse areal alignment. However, across both histological and visuotopic areas, we found that the hMRF parcellations exhibited comparable areal alignment with the Schaefer, Craddock, Shen and AICHA parcellations (Craddock et al., 2012; Shen et al., 2013; Joliot et al., 2015; Schaefer et al., 2018) and better areal alignment that the Gordon parcellation (Gordon et al., 2016). Compared with the semi-manual multimodal Glasser parcellation (Glasser et al., 2016), the hMRF parcellation exhibited comparable histological areal alignment, but worse visuotopic areal alignment.

Similar to the Schaefer parcellation, the 400-region hMRF parcellation aligned well with certain cortical areas, e.g., the boundary of histological area 17 (and visuotopic V1), as well as the boundary between histological areas 3 and 4 along the central sulcus. However, the hMRF parcellation did not align well with all cortical areas. It is worth noting that for some areas, the architectonic and retinotopic boundaries are themselves not perfectly aligned. For example, histological area 18 is not well aligned to visuotopic areas V2 or V3. Therefore, it is not possible for the hMRF parcellation to align well with both histological and visuotopic boundaries. Nevertheless, given that the multimodal Glasser parcellation was better aligned with cortical areas, this suggests further room for improvements.

Similar to the Schaefer parcellation, the 400-region hMRF parcellation also captured subareal features. For example, the hMRF parcellation appeared to fractionate somatosensory and motor areas based on the different body representations, as well as visual regions based on their eccentricity representation. This was particularly clear for area 17 or V1 (Figure 1), but likely extended to other visuotopic areas. As mentioned in the introduction, we believe that this subareal characteristic can be potentially useful in many applications. For example, differentiation of the hand and tongue regions might be useful when modeling a task involving button presses. Similarly, many tasks require participants to fixate on certain visual stimuli, so we expect differential response between central (low eccentricity) and peripheral (high eccentricity) visual regions.

4.3 hMRF parcels are homogeneous during resting and task states

Brain parcellations are often used for dimensionality reduction in MRI analyses (Eickhoff et al., 2018b). For example, resting-state or task-state fMRI time courses within each brain parcel are often averaged to compute function connectivity matrices, which are in

turn used for studying mental disorders (Fair et al., 2013; Xia et al., 2018; Kebets et al., 2019), predicting behavioral traits (Finn et al., 2015; Greene et al., 2018; Chen et al., 2022), graph theoretic analyses (Achard et al., 2006; Wang et al., 2010; Fornito et al., 2013) and neural mass modeling (Cabral et al., 2011; Hansen et al., 2015; Kong et al., 2021b). Such a dimensionality reduction strategy only makes sense if the resting-fMRI or task-fMRI time courses are similar (i.e., homogeneous) within each parcel.

In our previous study (Schaefer et al., 2018), we demonstrated that the Schaefer parcellations exhibited better task inhomogeneity and resting homogeneity than four other public parcellations (Craddock et al., 2012; Shen et al., 2013; Glasser et al., 2016; Gordon et al., 2016). One concern is that the additional homotopic constraint in the hMRF model might weaken the homogeneity properties of the local-global parcellations. However, we found that the hMRF parcellations exhibited comparable homogeneity with the Schaefer parcellation and better homogeneity than five other parcellations (Craddock et al., 2012; Shen et al., 2013; Joliot et al., 2015; Glasser et al., 2016; Gordon et al., 2016)

Here, we evaluated task inhomogeneity using task contrasts from the HCP and ABCD datasets. We note that a strict task contrast might isolate a purer cognitive construct, but it was unlikely that any HCP or ABCD task contrast would isolate a single cognitive process. We also did not expect that any task contrast would only activate a single cortical area. Therefore, similar to our previous study (Schaefer et al., 2018), task inhomogeneity was defined as the standard deviation of task activation z-values within each parcel. Low (good) task inhomogeneity could be achieved if activation strength was uniform within each parcel. This approach did not require the task contrast to activate a single cognitive function or single cortical area. Therefore, rather than having to choose a subset of “pure” task contrasts, we utilized all unique contrasts in the HCP and ABCD datasets.

In the case of resting homogeneity, our evaluation utilized data across diverse acquisition protocols, preprocessing and demographics. The hMRF parcellations were estimated from young adults in the GSP dataset acquired from Siemens Tim Trio scanners (Holmes et al., 2015) whose fMRI data was preprocessed using a pipeline involving whole-brain signal regression in FreeSurfer fsaverage space (Li et al., 2019). The improvements in resting homogeneity were demonstrated in additional data from different Siemens and GE scanners with different acquisition protocols (single-band versus multiple-band), preprocessed with different pipelines (ICA-FIX versus whole-brain signal regression), in different coordinate systems (fsaverage, fsLR and MNI152) and in participants with different demographics (young adults, children and Asian populations).

Overall, our results suggest that hMRF parcellations are homogeneous during resting and task states, suggesting their potential utility for dimensionality reduction in future fMRI studies.

4.4 Resolution of cortical parcellation

There is no consensus on the "optimal" resolution of brain parcellations (Eickhoff et al., 2015). From the neuroscience perspective, the brain is hierarchically organized (Churchland and Sejnowski 1988; Mesulam 1998) from molecules to synapses to neurons to areas to systems. Large-scale networks comprise multiple cortical areas, while cortical areas can be again subdivided given their heterogeneity (Kaas 1987; Amunts and Zilles 2015). Consequently, finding the "right" number of parcels is a biologically ill-posed problem. Indeed, it is unlikely that there is an optimal resolution for cortical parcellations. In fact, parcellations of different resolutions are likely useful for different applications. For example, behavioral prediction generally improves with higher dimensional parcellations before plateauing or becoming worse, although the exact results can be quite variable across studies (Dadi et al., 2019; Pervaiz et al., 2020; Kong et al., 2022). On the other hand, a recent study has suggested that brain–behavior relationships are scale-dependent (Betzel et al., 2019). Finally, in many applications (e.g., neural mass modelling or edge-centric network analyses), higher resolution brain parcellations are often not computationally feasible, so studies often employ lower resolution parcellations (Deco et al., 2013; Hansen et al., 2015; Faskowitz et al., 2020; Kong et al., 2021b). Consequently, we generated hMRF parcellations at multiple resolutions, ranging from 100 to 1000 parcels at 100-parcel interval, which will hopefully be useful for a wide range of applications.

4.5 Confounds when comparing brain parcellations

An important confound when comparing parcellations is the number of parcels. In general, greater number of parcels will lead to better evaluation metrics. Here, we controlled for the number of parcels by estimating hMRF parcellations with the same number of parcels as the benchmarked parcellations.

Another major confounding factor is that different parcellations are typically estimated from different datasets in different coordinate systems. Therefore, we employed multiple datasets across different coordinate systems to increase confidence in the generalizability of our parcellations to new datasets and coordinate systems.

However, we note that some biases could not be fully eliminated. Projecting a parcellation from the original coordinate system (in which the parcellation was derived) will lead to some degradation in the parcellation quality. This is especially true when projecting parcellations between a surface coordinate system (fsLR or fsaverage) and a volumetric coordinate system (MNI152).

Therefore, a parcellation estimated in coordinate system X will enjoy inherent advantage over other parcellations projected to coordinate system X. For example, when using the HCP dataset in fsLR space, hMRF parcellations exhibited better resting homogeneity than the Shen and Craddock parcellations with relatively large improvements of 8.1% and 6.4% respectively. On the other hand, when using the same HCP dataset in MNI152 space, hMRF parcellations were still statistically more homogeneous than the Shen and Craddock parcellations, but the margins were significantly reduced with improvements of only 0.5% and 1.2% improvements respectively.

4.6 Limitations and future work

There are two main limitations in the current study. First, the hMRF parcellations were derived by combining resting-fMRI data across many participants. However, recent studies have documented that the topography of brain networks and parcellations vary substantially across individuals, so a group-average parcellation will miss out on fine-scale individual-specific features (Laumann et al., 2015; Glasser et al., 2016; Gordon et al., 2017; Bijsterbosch et al., 2019; Kong et al., 2019; Seitzman et al., 2019). Future work will investigate the estimation of homotopic areal-level parcellations in individual participants.

Second, the hMRF parcellations were estimated only from resting-fMRI data. Traditionally, cortical areas are defined based on multi-modal criteria, including architectonics, topography, function and connectivity (Kaas, 1987; Felleman and Van Essen, 1991). In the current study, we estimated parcellations from resting-fMRI, which provides an indirect measure of brain connectivity reflecting multi-synaptic coupling (Vincent et al., 2007; Lu et al., 2011). We then validated the parcellations using histological boundaries, visuotopic boundaries, task inhomogeneity and resting homogeneity, which acted as proxies for architectonics, topography, function and connectivity respectively.

Given that the multi-modal Glasser parcellation exhibited better alignment with visuotopic boundaries, incorporating further multimodal information might further improve parcellation quality. Indeed, several studies have suggested that brain networks reconfigure during tasks (Cole et al., 2014; Krienen et al., 2014) and estimates of brain parcellations are

sensitive to task states (Salehi et al., 2020). Some have interpreted these results to suggest the need for separate parcellations during resting and task states (Salehi et al., 2020). However, our interpretation is that the boundaries of cortical areas (e.g., V1) should be invariant to transient task states over the span of a few days, although cortical areal boundaries can certainly be shaped during development and long-term experiences (Arcaro et al., 2017; Gomez et al., 2019). Instead, these results (Salehi et al., 2020) suggest the value of estimating areal-level parcellations from multi-modal data.

However, we note that incorporating multi-modal features can be challenging because of the need to select among potentially conflicting information (Eickhoff et al., 2018a). In the case of the semi-manual Glasser parcellation (Glasser et al., 2016), a trained anatomist ignored strong gradients within somatomotor cortex and V1 based on prior neuroanatomical knowledge. Such prior knowledge might have led to better visuotopic alignment in the Glasser parcellation compared with the hMRF parcellations. However, the better visuotopic alignment came at the cost of worse task-inhomogeneity and resting-homogeneity across all datasets, including the HCP dataset from which the Glasser parcellation was partially derived from. The reason is that the Glasser parcellation "wasted" precious parcels distinguishing between cortical areas (e.g., areas 3a and 3b), which have extremely similar resting-fMRI and task-fMRI properties. On the other hand, the Glasser parcellation did not differentiate among body representations (e.g., hand and tongue) with highly distinctive resting-fMRI and task-fMRI properties. Overall, it remains an open problem how to automatically select among competing and conflicting information across multimodal features. We leave this for future work.

5 Conclusion

We develop a homotopic variant of the gwMRF local-global parcellation model, where each parcel has a spatial counterpart on the other hemisphere. The resulting parcels are homogeneous in both resting and task states across datasets from diverse scanners, acquisition protocols, preprocessing and demographics. The parcellations also agree well with a number of known visuotopic and histological boundaries, while capturing meaningful sub-areal features. Finally, the homotopic local-global parcellations replicate known homotopic and lateralization properties of the cerebral cortex. Multi-resolution homotopic local-global parcellations are publicly available as a resource for future studies (GITHUB_LINK).

6 Acknowledgement

This work was supported by the Singapore National Research Foundation (NRF) Fellowship (Class of 2017), the National University of Singapore Yong Loo Lin School of Medicine (NUHSRO/2020/124/TMR/LOA), the Singapore National Medical Research Council (NMRC) LCG (OFLCG19May-0035), NMRC STaR (STaR20nov-0003), and the United States National Institutes of Health (R01MH120080). This study is also supported by the National Research Foundation (NRF) under the Open Fund-Large Collaborative Grant (OF-LCG; MOH-000504) administered by the Singapore Ministry of Health's National Medical Research Council (NMRC) and the Agency for Science, Technology and Research (A*STAR). In RIE2025, GUSTO is supported by funding from the NRF's Human Health and Potential (HHP) Domain, under the Human Potential Programme. Any opinions, findings and conclusions or recommendations expressed in this material are those of the authors and do not reflect the views of the Singapore NRF or the Singapore NMRC. Xi-Nian Zuo was supported by the Startup Funds for Leading Talents at Beijing Normal University, the National Basic Science Data Center 'Chinese Data-sharing Warehouse for In-vivo Imaging Brain' (NBSDC-DB-15). Computational work for this article was partially performed on resources of the National Supercomputing Centre, Singapore (https://www.nscc.sg). Data were in part provided by the Human Connectome Project, WU-Minn Consortium (Principal Investigators: David Van Essen and Kamil Ugurbil; 1U54MH091657) funded by the 16 NIH Institutes and Centers that support the NIH Blueprint for Neuroscience Research; and by the McDonnell Center for Systems Neuroscience at Washington University.

7 References

Abdollahi, R.O., Kolster, H., Glasser, M.F., Robinson, E.C., Coalson, T.S., Dierker, D., Jenkinson, M., Van Essen, D.C., Orban, G.A., 2014. Correspondences between retinotopic areas and myelin maps in human visual cortex. NeuroImage 99, 509–524. https://doi.org/10.1016/j.neuroimage.2014.06.042

Aboitiz, F., Scheibel, A.B., Fisher, R.S., Zaidel, E., 1992. Fiber composition of the human corpus callosum. Brain Research 598, 143–153. https://doi.org/10.1016/0006-8993(92)90178-C

Achard, S., Salvador, R., Whitcher, B., Suckling, J., Bullmore, E., 2006. A Resilient, Low-Frequency, Small-World Human Brain Functional Network with Highly Connected Association Cortical Hubs. J. Neurosci. 26, 63–72. https://doi.org/10.1523/JNEUROSCI.3874-05.2006

Amunts, K., Malikovic, A., Mohlberg, H., Schormann, T., Zilles, K., 2000. Brodmann's Areas 17 and 18 Brought into Stereotaxic Space—Where and How Variable? NeuroImage 11, 66–84. https://doi.org/10.1006/nimg.1999.0516

Amunts, K., Mohlberg, H., Bludau, S., Zilles, K., 2020. Julich-Brain: A 3D probabilistic atlas of the human brain's cytoarchitecture. Science 369, 988–992. https://doi.org/10.1126/science.abb4588

Amunts, K., Schleicher, A., Bürgel, U., Mohlberg, H., Uylings, H.B.M., Zilles, K., 1999. Broca's region revisited: Cytoarchitecture and intersubject variability. Journal of Comparative Neurology 412, 319–341. https://doi.org/10.1002/(SICI)1096-9861(19990920)412:2<319::AID-CNE10>3.0.CO;2-7

Amunts, K., Weiss, P.H., Mohlberg, H., Pieperhoff, P., Eickhoff, S., Gurd, J.M., Marshall, J.C., Shah, N.J., Fink, G.R., Zilles, K., 2004. Analysis of neural mechanisms underlying verbal fluency in cytoarchitectonically defined stereotaxic space—The roles of Brodmann areas 44 and 45. NeuroImage 22, 42–56. https://doi.org/10.1016/j.neuroimage.2003.12.031

Amunts, K., Zilles, K., 2015. Architectonic mapping of the human brain beyond Brodmann. Neuron 88, 1086–1107.

Arcaro, M.J., Schade, P.F., Vincent, J.L., Ponce, C.R., Livingstone, M.S., 2017. Seeing faces is necessary for face-domain formation. Nat Neurosci 20, 1404–1412. https://doi.org/10.1038/nn.4635

Barch, D.M., Burgess, G.C., Harms, M.P., Petersen, S.E., Schlaggar, B.L., Corbetta, M., Glasser, M.F., Curtiss, S., Dixit, S., Feldt, C., Nolan, D., Bryant, E., Hartley, T., Footer, O., Bjork, J.M., Poldrack, R., Smith, S., Johansen-Berg, H., Snyder, A.Z., Van Essen, D.C., 2013. Function in the human connectome: Task-fMRI and individual differences in behavior. NeuroImage, Mapping the Connectome 80, 169–189. https://doi.org/10.1016/j.neuroimage.2013.05.033

Barrett, L.F., Satpute, A.B., 2013. Large-scale brain networks in affective and social neuroscience: towards an integrative functional architecture of the brain. Current Opinion in Neurobiology, Social and emotional neuroscience 23, 361–372. https://doi.org/10.1016/j.conb.2012.12.012

Betzel, R.F., Bertolero, M.A., Gordon, E.M., Gratton, C., Dosenbach, N.U.F., Bassett, D.S., 2019. The community structure of functional brain networks exhibits scale-specific patterns of inter- and intra-subject variability. NeuroImage 202, 115990. https://doi.org/10.1016/j.neuroimage.2019.07.003

Bijsterbosch, J.D., Beckmann, C.F., Woolrich, M.W., Smith, S.M., Harrison, S.J., 2019. The relationship between spatial configuration and functional connectivity of brain regions revisited. eLife 8, e44890. https://doi.org/10.7554/eLife.44890

Biswal, B., Zerrin Yetkin, F., Haughton, V.M., Hyde, J.S., 1995. Functional connectivity in the motor cortex of resting human brain using echo-planar MRI. Magnetic resonance in medicine 34, 537–541.

Burgess, G.C., Kandala, S., Nolan, D., Laumann, T.O., Power, J.D., Adeyemo, B., Harms, M.P., Petersen, S.E., Barch, D.M., 2016. Evaluation of denoising strategies to address motion-correlated artifacts in resting-state functional magnetic resonance imaging data from the human connectome project. Brain connectivity 6, 669–680.

Cabral, J., Hugues, E., Sporns, O., Deco, G., 2011. Role of local network oscillations in resting-state functional connectivity. NeuroImage 57, 130–139. https://doi.org/10.1016/j.neuroimage.2011.04.010

Calhoun, V.D., Kiehl, K.A., Pearlson, G.D., 2008. Modulation of temporally coherent brain networks estimated using ICA at rest and during cognitive tasks. Human Brain Mapping 29, 828–838. https://doi.org/10.1002/hbm.20581

Casey, B.J., Cannonier, T., Conley, M.I., Cohen, A.O., Barch, D.M., Heitzeg, M.M., Soules, M.E., Teslovich, T., Dellarco, D.V., Garavan, H., 2018. The adolescent brain cognitive development (ABCD) study: imaging acquisition across 21 sites. Developmental cognitive neuroscience 32, 43–54.

Chen, J., Tam, A., Kebets, V., Orban, C., Ooi, L.Q.R., Asplund, C.L., Marek, S., Dosenbach, N.U.F., Eickhoff, S.B., Bzdok, D., Holmes, A.J., Yeo, B.T.T., 2022. Shared and unique brain network features predict cognitive, personality, and mental health scores in the ABCD study. Nat Commun 13, 2217. https://doi.org/10.1038/s41467-022-29766-8

Churchland, P.S., Sejnowski, T.J., 1988. Perspectives on cognitive neuroscience. Science 242, 741–745.

Cohen, A.L., Fair, D.A., Dosenbach, N.U., Miezin, F.M., Dierker, D., Van Essen, D.C., Schlaggar, B.L., Petersen, S.E., 2008. Defining functional areas in individual human brains using resting functional connectivity MRI. Neuroimage 41, 45–57.

Cole, M.W., Bassett, D.S., Power, J.D., Braver, T.S., Petersen, S.E., 2014. Intrinsic and task-evoked network architectures of the human brain. Neuron 83, 238–251.

Cox, R.W., 1996. AFNI: software for analysis and visualization of functional magnetic resonance neuroimages. Computers and Biomedical research 29, 162–173.

Craddock, R.C., James, G.A., Holtzheimer III, P.E., Hu, X.P., Mayberg, H.S., 2012. A whole brain fMRI atlas generated via spatially constrained spectral clustering. Human brain mapping 33, 1914–1928.

Dadi, K., Rahim, M., Abraham, A., Chyzhyk, D., Milham, M., Thirion, B., Varoquaux, G., 2019. Benchmarking functional connectome-based predictive models for resting-state fMRI. NeuroImage 192, 115–134. https://doi.org/10.1016/j.neuroimage.2019.02.062

Damoiseaux, J.S., Rombouts, S.A.R.B., Barkhof, F., Scheltens, P., Stam, C.J., Smith, S.M., Beckmann, C.F., 2006. Consistent resting-state networks across healthy subjects. Proceedings of the National Academy of Sciences 103, 13848–13853. https://doi.org/10.1073/pnas.0601417103

Deco, G., Ponce-Alvarez, A., Mantini, D., Romani, G.L., Hagmann, P., Corbetta, M., 2013. Resting-state functional connectivity emerges from structurally and dynamically shaped slow linear fluctuations. Journal of Neuroscience 33, 11239–11252.

Duffy, F.H., Mcanulty, G.B., Albert, M.S., 1996. Effects of age upon interhemispheric EEG coherence in normal adults. Neurobiology of aging 17, 587–599.

Ehrsson, H.H., Geyer, S., Naito, E., 2003. Imagery of Voluntary Movement of Fingers, Toes, and Tongue Activates Corresponding Body-Part-Specific Motor Representations. Journal of Neurophysiology 90, 3304–3316. https://doi.org/10.1152/jn.01113.2002

Eickhoff, S.B., Constable, R.T., Yeo, B.T., 2018a. Topographic organization of the cerebral cortex and brain cartography. Neuroimage 170, 332–347.

Eickhoff, S.B., Yeo, B.T.T., Genon, S., 2018b. Imaging-based parcellations of the human brain. Nat Rev Neurosci 19, 672–686. https://doi.org/10.1038/s41583-018-0071-7

Eickhoff, S.B., Thirion, B., Varoquaux, G., Bzdok, D., 2015. Connectivity-based parcellation: Critique and implications. Human brain mapping 36, 4771–4792.
Fair, D.A., Miranda-Dominguez, O., Snyder, A.Z., Perrone, A., Earl, E.A., Van, A.N., Koller, J.M., Feczko, E., Tisdall, M.D., van der Kouwe, A., Klein, R.L., Mirro, A.E., Hampton, J.M., Adeyemo, B., Laumann, T.O., Gratton, C., Greene, D.J., Schlaggar, B.L., Hagler, D.J., Watts, R., Garavan, H., Barch, D.M., Nigg, J.T., Petersen, S.E., Dale, A.M., Feldstein-Ewing, S.W., Nagel, B.J., Dosenbach, N.U.F., 2020. Correction of respiratory artifacts in MRI head motion estimates. NeuroImage 208, 116400. https://doi.org/10.1016/j.neuroimage.2019.116400
Fair, D.A., Nigg, J.T., Iyer, S., Bathula, D., Mills, K.L., Dosenbach, N.U., Schlaggar, B.L., Mennes, M., Gutman, D., Bangaru, S., 2013. Distinct neural signatures detected for ADHD subtypes after controlling for micro-movements in resting state functional connectivity MRI data. Frontiers in systems neuroscience 6, 80.
Faskowitz, J., Esfahlani, F.Z., Jo, Y., Sporns, O., Betzel, R.F., 2020. Edge-centric functional network representations of human cerebral cortex reveal overlapping system-level architecture. Nat Neurosci 23, 1644–1654. https://doi.org/10.1038/s41593-020-00719-y
Felleman, D.J., Van Essen, D.C., 1991. Distributed hierarchical processing in the primate cerebral cortex. Cerebral cortex (New York, NY: 1991) 1, 1–47.
Finn, E.S., Shen, X., Scheinost, D., Rosenberg, M.D., Huang, J., Chun, M.M., Papademetris, X., Constable, R.T., 2015. Functional connectome fingerprinting: identifying individuals using patterns of brain connectivity. Nature neuroscience 18, 1664–1671.
Fischl, B., 2012. FreeSurfer. Neuroimage 62, 774–781. https://doi.org/10.1016/j.neuroimage.2012.01.021
Fischl, B., Rajendran, N., Busa, E., Augustinack, J., Hinds, O., Yeo, B.T.T., Mohlberg, H., Amunts, K., Zilles, K., 2008. Cortical Folding Patterns and Predicting Cytoarchitecture. Cerebral Cortex 18, 1973–1980. https://doi.org/10.1093/cercor/bhm225
Fornito, A., Zalesky, A., Breakspear, M., 2013. Graph analysis of the human connectome: promise, progress, and pitfalls. Neuroimage 80, 426–444.
Geyer, S., 2004. The microstructural border between the motor and the cognitive domain in the human cerebral cortex. Adv Anat Embryol Cell Biol 174, I–VIII, 1–89. https://doi.org/10.1007/978-3-642-18910-4
Geyer, S., Ledberg, A., Schleicher, A., Kinomura, S., Schormann, T., Bürgel, U., Klingberg, T., Larsson, J., Zilles, K., Roland, P.E., 1996. Two different areas within the primary motor cortex of man. Nature 382, 805–807. https://doi.org/10.1038/382805a0
Geyer, S., Matelli, M., Luppino, G., Zilles, K., 2000. Functional neuroanatomy of the primate isocortical motor system. Anat Embryol 202, 443–474. https://doi.org/10.1007/s004290000127
Geyer, S., Schleicher, A., Schormann, T., Mohlberg, H., Bodegård, A., Roland, P.E., Zilles, K., 2001. Integration of microstructural and functional aspects of human somatosensory areas 3a, 3b, and 1 on the basis of a computerized brain atlas. Anat Embryol 204, 351–366. https://doi.org/10.1007/s004290100200
Geyer, S., Schleicher, A., Zilles, K., 1999. Areas 3a, 3b, and 1 of Human Primary Somatosensory Cortex: 1. Microstructural Organization and Interindividual Variability. NeuroImage 10, 63–83. https://doi.org/10.1006/nimg.1999.0440
Glasser, M.F., Coalson, T.S., Robinson, E.C., Hacker, C.D., Harwell, J., Yacoub, E., Ugurbil, K., Andersson, J., Beckmann, C.F., Jenkinson, M., 2016. A multi-modal parcellation of human cerebral cortex. Nature 536, 171–178.
Glasser, M.F., Sotiropoulos, S.N., Wilson, J.A., Coalson, T.S., Fischl, B., Andersson, J.L., Xu, J., Jbabdi, S., Webster, M., Polimeni, J.R., Van Essen, D.C., Jenkinson, M., 2013. The Minimal Preprocessing Pipelines for the Human Connectome Project. Neuroimage 80, 105–124. https://doi.org/10.1016/j.neuroimage.2013.04.127

Gomez, J., Barnett, M., Grill-Spector, K., 2019. Extensive childhood experience with Pokémon suggests eccentricity drives organization of visual cortex. Nat Hum Behav 3, 611–624. https://doi.org/10.1038/s41562-019-0592-8

Gordon, E.M., Laumann, T.O., Adeyemo, B., Huckins, J.F., Kelley, W.M., Petersen, S.E., 2016. Generation and evaluation of a cortical area parcellation from resting-state correlations. Cerebral cortex 26, 288–303.

Gordon, E.M., Laumann, T.O., Gilmore, A.W., Newbold, D.J., Greene, D.J., Berg, J.J., Ortega, M., Hoyt-Drazen, C., Gratton, C., Sun, H., Hampton, J.M., Coalson, R.S., Nguyen, A.L., McDermott, K.B., Shimony, J.S., Snyder, A.Z., Schlaggar, B.L., Petersen, S.E., Nelson, S.M., Dosenbach, N.U.F., 2017. Precision Functional Mapping of Individual Human Brains. Neuron 95, 791-807.e7. https://doi.org/10.1016/j.neuron.2017.07.011

Gould, H.J., Cusick, C.G., Pons, T.P., Kaas, J.H., 1986. The relationship of corpus callosum connections to electrical stimulation maps of motor, supplementary motor, and the frontal eye fields in owl monkeys. Journal of Comparative Neurology 247, 297–325. https://doi.org/10.1002/cne.902470303

Greene, A.S., Gao, S., Scheinost, D., Constable, R.T., 2018. Task-induced brain state manipulation improves prediction of individual traits. Nat Commun 9, 2807. https://doi.org/10.1038/s41467-018-04920-3

Greve, D.N., Fischl, B., 2009. Accurate and robust brain image alignment using boundary-based registration. Neuroimage.

Griffanti, L., Salimi-Khorshidi, G., Beckmann, C.F., Auerbach, E.J., Douaud, G., Sexton, C.E., Zsoldos, E., Ebmeier, K.P., Filippini, N., Mackay, C.E., Moeller, S., Xu, J., Yacoub, E., Baselli, G., Ugurbil, K., Miller, K.L., Smith, S.M., 2014. ICA-based artefact and accelerated fMRI acquisition for improved Resting State Network imaging. Neuroimage 95, 232–247. https://doi.org/10.1016/j.neuroimage.2014.03.034

Hagler, D.J., Hatton, SeanN., Cornejo, M.D., Makowski, C., Fair, D.A., Dick, A.S., Sutherland, M.T., Casey, B.J., Barch, D.M., Harms, M.P., Watts, R., Bjork, J.M., Garavan, H.P., Hilmer, L., Pung, C.J., Sicat, C.S., Kuperman, J., Bartsch, H., Xue, F., Heitzeg, M.M., Laird, A.R., Trinh, T.T., Gonzalez, R., Tapert, S.F., Riedel, M.C., Squeglia, L.M., Hyde, L.W., Rosenberg, M.D., Earl, E.A., Howlett, K.D., Baker, F.C., Soules, M., Diaz, J., de Leon, O.R., Thompson, W.K., Neale, M.C., Herting, M., Sowell, E.R., Alvarez, R.P., Hawes, S.W., Sanchez, M., Bodurka, J., Breslin, F.J., Morris, A.S., Paulus, M.P., Simmons, W.K., Polimeni, J.R., van der Kouwe, A., Nencka, A.S., Gray, K.M., Pierpaoli, C., Matochik, J.A., Noronha, A., Aklin, W.M., Conway, K., Glantz, M., Hoffman, E., Little, R., Lopez, M., Pariyadath, V., Weiss, S.RB., Wolff-Hughes, D.L., DelCarmen-Wiggins, R., Feldstein Ewing, S.W., Miranda-Dominguez, O., Nagel, B.J., Perrone, A.J., Sturgeon, D.T., Goldstone, A., Pfefferbaum, A., Pohl, K.M., Prouty, D., Uban, K., Bookheimer, S.Y., Dapretto, M., Galvan, A., Bagot, K., Giedd, J., Infante, M.A., Jacobus, J., Patrick, K., Shilling, P.D., Desikan, R., Li, Y., Sugrue, L., Banich, M.T., Friedman, N., Hewitt, J.K., Hopfer, C., Sakai, J., Tanabe, J., Cottler, L.B., Nixon, S.J., Chang, L., Cloak, C., Ernst, T., Reeves, G., Kennedy, D.N., Heeringa, S., Peltier, S., Schulenberg, J., Sripada, C., Zucker, R.A., Iacono, W.G., Luciana, M., Calabro, F.J., Clark, D.B., Lewis, D.A., Luna, B., Schirda, C., Brima, T., Foxe, J.J., Freedman, E.G., Mruzek, D.W., Mason, M.J., Huber, R., McGlade, E., Prescot, A., Renshaw, P.F., Yurgelun-Todd, D.A., Allgaier, N.A., Dumas, J.A., Ivanova, M., Potter, A., Florsheim, P., Larson, C., Lisdahl, K., Charness, M.E., Fuemmeler, B., Hettema, J.M., Maes, H.H., Steinberg, J., Anokhin, A.P., Glaser, P., Heath, A.C., Madden, P.A., Baskin-Sommers, A., Constable, R.T., Grant, S.J., Dowling, G.J., Brown, S.A., Jernigan, T.L., Dale, A.M., 2019. Image processing and analysis methods for the Adolescent Brain Cognitive Development Study. NeuroImage 202, 116091. https://doi.org/10.1016/j.neuroimage.2019.116091

Hansen, E.C.A., Battaglia, D., Spiegler, A., Deco, G., Jirsa, V.K., 2015. Functional connectivity dynamics: Modeling the switching behavior of the resting state. NeuroImage 105, 525–535. https://doi.org/10.1016/j.neuroimage.2014.11.001
Hartwigsen, G., Bengio, Y., Bzdok, D., 2021. How does hemispheric specialization contribute to human-defining cognition? Neuron 109, 2075–2090. https://doi.org/10.1016/j.neuron.2021.04.024
Hinds, O., Polimeni, J.R., Rajendran, N., Balasubramanian, M., Amunts, K., Zilles, K., Schwartz, E.L., Fischl, B., Triantafyllou, C., 2009. Locating the functional and anatomical boundaries of human primary visual cortex. Neuroimage 46, 915–922.
Hirose, S., Watanabe, T., Jimura, K., Katsura, M., Kunimatsu, A., Abe, O., Ohtomo, K., Miyashita, Y., Konishi, S., 2012. Local signal time-series during rest used for areal boundary mapping in individual human brains. PLoS One 7, e36496.
Holmes, A.J., Hollinshead, M.O., O'Keefe, T.M., Petrov, V.I., Fariello, G.R., Wald, L.L., Fischl, B., Rosen, B.R., Mair, R.W., Roffman, J.L., Smoller, J.W., Buckner, R.L., 2015. Brain Genomics Superstruct Project initial data release with structural, functional, and behavioral measures. Sci Data 2, 150031. https://doi.org/10.1038/sdata.2015.31
Honnorat, N., Eavani, H., Satterthwaite, T.D., Gur, R.E., Gur, R.C., Davatzikos, C., 2015. GraSP: Geodesic Graph-based Segmentation with Shape Priors for the functional parcellation of the cortex. NeuroImage 106, 207–221. https://doi.org/10.1016/j.neuroimage.2014.11.008
Jenkinson, M., Beckmann, C.F., Behrens, T.E.J., Woolrich, M.W., Smith, S.M., 2012. FSL. NeuroImage, 20 YEARS OF fMRI 62, 782–790. https://doi.org/10.1016/j.neuroimage.2011.09.015
Joliot, M., Jobard, G., Naveau, M., Delcroix, N., Petit, L., Zago, L., Crivello, F., Mellet, E., Mazoyer, B., Tzourio-Mazoyer, N., 2015. AICHA: An atlas of intrinsic connectivity of homotopic areas. Journal of neuroscience methods 254, 46–59.
Jones, E.G., Wise, S.P., 1977. Size, laminar and columnar distribution of efferent cells in the sensory-motor cortex of monkeys. Journal of Comparative Neurology 175, 391–437. https://doi.org/10.1002/cne.901750403
Jones, E.G., 2012. The thalamus. Springer Science & Business Media.
Kaas, J.H., 1987. The organization of neocortex in mammals: implications for theories of brain function. Annu. rev. psychol 38, 129–151.
Kebets, V., Holmes, A.J., Orban, C., Tang, S., Li, J., Sun, N., Kong, R., Poldrack, R.A., Yeo, B.T.T., 2019. Somatosensory-Motor Dysconnectivity Spans Multiple Transdiagnostic Dimensions of Psychopathology. Biological Psychiatry, Cortical Pathology and Depression 86, 779–791. https://doi.org/10.1016/j.biopsych.2019.06.013
Killackey, H.P., Gould III, H.J., Cusick, C.G., Pons, T.P., Kaas, J.H., 1983. The relation of corpus callosum connections to architectonic fields and body surface maps in sensorimotor cortex of new and old world monkeys. Journal of Comparative Neurology 219, 384–419. https://doi.org/10.1002/cne.902190403
Kong, R., Li, J., Orban, C., Sabuncu, M.R., Liu, H., Schaefer, A., Sun, N., Zuo, X.-N., Holmes, A.J., Eickhoff, S.B., 2019. Spatial topography of individual-specific cortical networks predicts human cognition, personality, and emotion. Cerebral cortex 29, 2533–2551.
Kong, R., Tan, Y. Rui., Wulan, N., Ooi, Q.R., Farahibozorg, S.-R., Harrison, S., Bijsterbosch, J.D., Bernhardt, B.C., Eickhoff, S., Yeo, B.T., 2022. Comparison Between Gradients and Parcellations for Functional Connectivity Prediction of Behavior.
Kong, R., Yang, Q., Gordon, E., Xue, A., Yan, X., Orban, C., Zuo, X.-N., Spreng, N., Ge, T., Holmes, A., 2021a. Individual-specific areal-level parcellations improve functional connectivity prediction of behavior. Cerebral Cortex 31, 4477–4500.
Kong, X., Kong, R., Orban, C., Wang, P., Zhang, S., Anderson, K., Holmes, A., Murray, J.D., Deco, G., van den Heuvel, M., Yeo, B.T.T., 2021b. Sensory-motor cortices shape functional

connectivity dynamics in the human brain. Nat Commun 12, 6373. https://doi.org/10.1038/s41467-021-26704-y
Krienen, F.M., Yeo, B.T., Buckner, R.L., 2014. Reconfigurable task-dependent functional coupling modes cluster around a core functional architecture. Philosophical Transactions of the Royal Society B: Biological Sciences 369, 20130526.
Lamantia, A.-S., Rakic, P., 1990. Cytological and quantitative characteristics of four cerebral commissures in the rhesus monkey. Journal of Comparative Neurology 291, 520–537. https://doi.org/10.1002/cne.902910404
Laumann, T.O., Gordon, E.M., Adeyemo, B., Snyder, A.Z., Joo, S.J., Chen, M.-Y., Gilmore, A.W., McDermott, K.B., Nelson, S.M., Dosenbach, N.U., others, 2015. Functional system and areal organization of a highly sampled individual human brain. Neuron 87, 657–670.
Li, J., Bzdok, D., Chen, J., Tam, A., Ooi, L.Q.R., Holmes, A.J., Ge, T., Patil, K.R., Jabbi, M., Eickhoff, S.B., Yeo, B.T.T., Genon, S., 2022. Cross-ethnicity/race generalization failure of behavioral prediction from resting-state functional connectivity. Science Advances 8, eabj1812. https://doi.org/10.1126/sciadv.abj1812
Li, J., Kong, R., Liégeois, R., Orban, C., Tan, Y., Sun, N., Holmes, A.J., Sabuncu, M.R., Ge, T., Yeo, B.T., 2019. Global signal regression strengthens association between resting-state functional connectivity and behavior. NeuroImage 196, 126–141.
Lowe, M.J., Mock, B.J., Sorenson, J.A., 1998. Functional Connectivity in Single and Multislice Echoplanar Imaging Using Resting-State Fluctuations. NeuroImage 7, 119–132. https://doi.org/10.1006/nimg.1997.0315
Lu, J., Liu, H., Zhang, M., Wang, D., Cao, Y., Ma, Q., Rong, D., Wang, X., Buckner, R.L., Li, K., 2011. Focal Pontine Lesions Provide Evidence That Intrinsic Functional Connectivity Reflects Polysynaptic Anatomical Pathways. J. Neurosci. 31, 15065–15071. https://doi.org/10.1523/JNEUROSCI.2364-11.2011
Malik-Moraleda, S., Ayyash, D., Gallée, J., Affourtit, J., Hoffmann, M., Mineroff, Z., Jouravlev, O., Fedorenko, E., 2022. An investigation across 45 languages and 12 language families reveals a universal language network. Nat Neurosci 25, 1014–1019. https://doi.org/10.1038/s41593-022-01114-5
Mesulam, M.M., 1998. From sensation to cognition. Brain 121, 1013–1052. https://doi.org/10.1093/brain/121.6.1013
Middleton, F.A., Strick, P.L., 2000. Basal ganglia and cerebellar loops: motor and cognitive circuits. Brain Research Reviews 31, 236–250. https://doi.org/10.1016/S0165-0173(99)00040-5
Pandya, D.N., Vignolo, L.A., 1971. Intra- and interhemispheric projections of the precentral, premotor and arcuate areas in the rhesus monkey. Brain Research 26, 217–233. https://doi.org/10.1016/S0006-8993(71)80001-X
Pervaiz, U., Vidaurre, D., Woolrich, M.W., Smith, S.M., 2020. Optimising network modelling methods for fMRI. NeuroImage 211, 116604. https://doi.org/10.1016/j.neuroimage.2020.116604
Petrides, M., Pandya, D.N., 1999. Dorsolateral prefrontal cortex: comparative cytoarchitectonic analysis in the human and the macaque brain and corticocortical connection patterns. European Journal of Neuroscience 11, 1011–1036. https://doi.org/10.1046/j.1460-9568.1999.00518.x
Poldrack, R.A., 2006. Can cognitive processes be inferred from neuroimaging data? Trends in Cognitive Sciences 10, 59–63. https://doi.org/10.1016/j.tics.2005.12.004
Power, J.D., Cohen, A.L., Nelson, S.M., Wig, G.S., Barnes, K.A., Church, J.A., Vogel, A.C., Laumann, T.O., Miezin, F.M., Schlaggar, B.L., 2011. Functional network organization of the human brain. Neuron 72, 665–678.

Power, J.D., Mitra, A., Laumann, T.O., Snyder, A.Z., Schlaggar, B.L., Petersen, S.E., 2014. Methods to detect, characterize, and remove motion artifact in resting state fMRI. Neuroimage 84, 10.1016/j.neuroimage.2013.08.048. https://doi.org/10.1016/j.neuroimage.2013.08.048

Robinson, E.C., Jbabdi, S., Glasser, M.F., Andersson, J., Burgess, G.C., Harms, M.P., Smith, Stephen.M., Van Essen, D.C., Jenkinson, M., 2014. MSM: a new flexible framework for Multimodal Surface Matching☆. Neuroimage 100, 414–426. https://doi.org/10.1016/j.neuroimage.2014.05.069

Ryali, S., Chen, T., Supekar, K., Menon, V., 2013. A parcellation scheme based on von Mises-Fisher distributions and Markov random fields for segmenting brain regions using resting-state fMRI. Neuroimage 65, 83–96.

Salehi, M., Greene, A.S., Karbasi, A., Shen, X., Scheinost, D., Constable, R.T., 2020. There is no single functional atlas even for a single individual: Functional parcel definitions change with task. NeuroImage 208, 116366.

Salimi-Khorshidi, G., Douaud, G., Beckmann, C.F., Glasser, M.F., Griffanti, L., Smith, S.M., 2014. Automatic denoising of functional MRI data: Combining independent component analysis and hierarchical fusion of classifiers. NeuroImage 90, 449–468. https://doi.org/10.1016/j.neuroimage.2013.11.046

Salvador, R., Suckling, J., Coleman, M.R., Pickard, J.D., Menon, D., Bullmore, E.D., 2005. Neurophysiological architecture of functional magnetic resonance images of human brain. Cerebral cortex 15, 1332–1342.

Schaefer, A., Kong, R., Gordon, E.M., Laumann, T.O., Zuo, X.-N., Holmes, A.J., Eickhoff, S.B., Yeo, B.T., 2018. Local-global parcellation of the human cerebral cortex from intrinsic functional connectivity MRI. Cerebral cortex 28, 3095–3114.

Schmahmann, J.D., Smith, E.E., Eichler, F.S., Filley, C.M., 2008. Cerebral White Matter. Annals of the New York Academy of Sciences 1142, 266–309. https://doi.org/10.1196/annals.1444.017

Seitzman, B.A., Gratton, C., Laumann, T.O., Gordon, E.M., Adeyemo, B., Dworetsky, A., Kraus, B.T., Gilmore, A.W., Berg, J.J., Ortega, M., Nguyen, A., Greene, D.J., McDermott, K.B., Nelson, S.M., Lessov-Schlaggar, C.N., Schlaggar, B.L., Dosenbach, N.U.F., Petersen, S.E., 2019. Trait-like variants in human functional brain networks. Proceedings of the National Academy of Sciences 116, 22851–22861. https://doi.org/10.1073/pnas.1902932116

Sereno, M.I., Dale, A.M., Reppas, J.B., Kwong, K.K., Belliveau, J.W., Brady, T.J., Rosen, B.R., Tootell, R.B.H., 1995. Borders of multiple visual areas in humans revealed by functional magnetic resonance imaging. Science 268, 889–893.

Shen, X., Tokoglu, F., Papademetris, X., Constable, R.T., 2013. Groupwise whole-brain parcellation from resting-state fMRI data for network node identification. Neuroimage 82, 403–415.

Siegel, J.S., Mitra, A., Laumann, T.O., Seitzman, B.A., Raichle, M., Corbetta, M., Snyder, A.Z., 2017. Data quality influences observed links between functional connectivity and behavior. Cerebral cortex 27, 4492–4502.

Smith, S.M., Fox, P.T., Miller, K.L., Glahn, D.C., Fox, P.M., Mackay, C.E., Filippini, N., Watkins, K.E., Toro, R., Laird, A.R., Beckmann, C.F., 2009. Correspondence of the brain's functional architecture during activation and rest. Proceedings of the National Academy of Sciences 106, 13040–13045. https://doi.org/10.1073/pnas.0905267106

Soh, S.-E., Tint, M.T., Gluckman, P.D., Godfrey, K.M., Rifkin-Graboi, A., Chan, Y.H., Stünkel, W., Holbrook, J.D., Kwek, K., Chong, Y.-S., Saw, S.M., the GUSTO Study Group, 2014. Cohort Profile: Growing Up in Singapore Towards healthy Outcomes (GUSTO) birth cohort study. International Journal of Epidemiology 43, 1401–1409. https://doi.org/10.1093/ije/dyt125

Stark, D.E., Margulies, D.S., Shehzad, Z.E., Reiss, P., Kelly, A.C., Uddin, L.Q., Gee, D.G., Roy, A.K., Banich, M.T., Castellanos, F.X., 2008. Regional variation in interhemispheric coordination of intrinsic hemodynamic fluctuations. Journal of Neuroscience 28, 13754–13764.

Szaflarski, J.P., Holland, S.K., Schmithorst, V.J., Byars, A.W., 2006. fMRI study of language lateralization in children and adults. Human Brain Mapping 27, 202–212. https://doi.org/10.1002/hbm.20177

Ungerleider, L.G., Desimone, R., 1986. Cortical connections of visual area MT in the macaque. Journal of Comparative Neurology 248, 190–222.

Van Den Heuvel, M., Mandl, R., Hulshoff Pol, H., 2008. Normalized cut group clustering of resting-state FMRI data. PloS one 3, e2001.

Van Essen, D.C., Glasser, M.F., 2014. In vivo architectonics: a cortico-centric perspective. Neuroimage 93, 157–164.

Van Essen, D.C., Glasser, M.F., Dierker, D.L., Harwell, J., Coalson, T., 2012a. Parcellations and Hemispheric Asymmetries of Human Cerebral Cortex Analyzed on Surface-Based Atlases. Cerebral Cortex 22, 2241–2262. https://doi.org/10.1093/cercor/bhr291

Van Essen, D.C., Newsome, W.T., Bixby, J.L., 1982. The pattern of interhemispheric connections and its relationship to extrastriate visual areas in the macaque monkey. J. Neurosci. 2, 265–283. https://doi.org/10.1523/JNEUROSCI.02-03-00265.1982

Van Essen, D.C., Ugurbil, K., Auerbach, E., Barch, D., Behrens, T.E., Bucholz, R., Chang, A., Chen, L., Corbetta, M., Curtiss, S.W., 2012b. The Human Connectome Project: a data acquisition perspective. Neuroimage 62, 2222–2231.

Van Essen, D.C., Zeki, S.M., 1978. The topographic organization of rhesus monkey prestriate cortex. The Journal of physiology 277, 193–226.

Vincent, J.L., Patel, G.H., Fox, M.D., Snyder, A.Z., Baker, J.T., Van Essen, D.C., Zempel, J.M., Snyder, L.H., Corbetta, M., Raichle, M.E., 2007. Intrinsic functional architecture in the anaesthetized monkey brain. Nature 447, 83–86. https://doi.org/10.1038/nature05758

Wang, J., Zuo, X., He, Y., 2010. Graph-based network analysis of resting-state functional MRI. Frontiers in systems neuroscience 16.

Wig, Gagan S, Laumann, T.O., Petersen, S.E., 2014. An approach for parcellating human cortical areas using resting-state correlations. Neuroimage 93, 276–291.

Wu, J., Ngo, G.H., Greve, D., Li, J., He, T., Fischl, B., Eickhoff, S.B., Yeo, B.T.T., 2018. Accurate nonlinear mapping between MNI volumetric and FreeSurfer surface coordinate systems. Human Brain Mapping 39, 3793–3808. https://doi.org/10.1002/hbm.24213

Xia, C.H., Ma, Z., Ciric, R., Gu, S., Betzel, R.F., Kaczkurkin, A.N., Calkins, M.E., Cook, P.A., García de la Garza, A., Vandekar, S.N., Cui, Z., Moore, T.M., Roalf, D.R., Ruparel, K., Wolf, D.H., Davatzikos, C., Gur, R.C., Gur, R.E., Shinohara, R.T., Bassett, D.S., Satterthwaite, T.D., 2018. Linked dimensions of psychopathology and connectivity in functional brain networks. Nat Commun 9, 3003. https://doi.org/10.1038/s41467-018-05317-y

Xu, T., Opitz, A., Craddock, R.C., Wright, M.J., Zuo, X.-N., Milham, M.P., 2016. Assessing variations in areal organization for the intrinsic brain: from fingerprints to reliability. Cerebral Cortex 26, 4192–4211.

Xue, A., Kong, R., Yang, Q., Eldaief, M.C., Angeli, P.A., DiNicola, L.M., Braga, R.M., Buckner, R.L., Yeo, B.T.T., 2021. The detailed organization of the human cerebellum estimated by intrinsic functional connectivity within the individual. Journal of Neurophysiology 125, 358–384. https://doi.org/10.1152/jn.00561.2020

Yeo, B.T., Krienen, F.M., Eickhoff, S.B., Yaakub, S.N., Fox, P.T., Buckner, R.L., Asplund, C.L., Chee, M.W., 2015. Functional specialization and flexibility in human association cortex. Cerebral cortex 25, 3654–3672.

Yeo, B.T., Krienen, F.M., Sepulcre, J., Sabuncu, M.R., Lashkari, D., Hollinshead, M., Roffman, J.L., Smoller, J.W., Zöllei, L., Polimeni, J.R., 2011. The organization of the human cerebral cortex estimated by intrinsic functional connectivity. Journal of neurophysiology.

Zuo, X.-N., Kelly, C., Martino, A.D., Mennes, M., Margulies, D.S., Bangaru, S., Grzadzinski, R., Evans, A.C., Zang, Y.-F., Castellanos, F.X., Milham, M.P., 2010. Growing Together and Growing Apart: Regional and Sex Differences in the Lifespan Developmental Trajectories of Functional Homotopy. J. Neurosci. 30, 15034–15043. https://doi.org/10.1523/JNEUROSCI.2612-10.2010

Homotopic local-global parcellation of the human cerebral cortex from resting-state functional connectivity

Supplemental Material

This supplemental material consists of Supplemental Methods and Supplemental Results to complement the Methods and Results sections in the main text.

Supplementary Methods

This section provides the mathematical and implementation details for the hMRF parcellation procedure. Section S1 discusses the choice of surface mesh used in hMRF parcellation procedure. Section S2 specifies the mathematical details regarding the hMRF model. Section S3 summarizes how to optimize the hMRF objective function. Section S4 provides details regarding the derivations of results from Supplementary Section S2. Section S5 discusses how the hyperparameters were set for the generation of hMRF parcellations.

S1. Choice of Surface Mesh

Our parcellation procedure is performed on the Freesurfer fsaverage6 template, where each spherical hemispheric mesh consists of 40,962 vertices. Each vertex is connected to 5 or 6 neighbor's vertices via edges. Note that there is no vertex-to-vertex correspondence between the left and right hemispheres in fsaverage6 space, therefore vertex-wise correspondence was established with the FreeSurfer command *mris_left_right_register*.

S2. Mathematical Model

In this section, we discuss the intuition behind the hMRF model. The fMRI time courses of each participant at each vertex were normalized to be of zero mean and standard deviation of one. The GSP dataset consists of participants with one or two runs. For participants with two runs, each run was normalized separately. For each vertex, the time courses of all runs of all participants were concatenated into a long column vector and normalized into unit norm. The concatenated time course at vertex n is denoted as y_n. This normalization and concatenation approach is motivated by the fact that the inner product of two concatenated time courses is equivalent to computing the Pearson product-moment correlation for each participant and then averaging across all participants (for more details, see Supplementary Methods S3 of Schaefer et al., 2018).

Let N denote the total number of vertices. Our input data thus consists of the normalized and concatenated time courses $\{y_1, \dots, y_N\}$, denoted briefly as $y_{1:N}$, and the 3-dimensional spherical coordinates $s_{1:N}$. Our goal is to estimate the cortical labels for each vertex $l_{1:N} = \{l_1, \cdots, l_N\}$, where $l_n \in \{1, \dots, L\}$ and L indicates the desired number of parcels. The following model describes the joint distribution of labels $l_{1:N}$, spatial coordinates $s_{1:N}$, and the fMRI time courses $y_{1:N}$:

$$p(l_{1:N}, y_{1:N}, s_{1:N}) = \frac{1}{Z}\exp\{-U_{global}(l_{1:N}, y_{1:N}) - V_{grad}(l_{1:N}) - U_{xyz}(l_{1:N}, s_{1:N}) - V_{homo}(l_{1:N}) - U_{sep}(l_{1:N})\}, \quad (1)$$

where Z is the normalization term to ensure that the resultant term is a valid probability distribution. $U_{global}(l_{1:N}, y_{1:N})$ is the unary potential encoding the global similarity of fMRI time courses. $V_{grad}(l_{1:N})$ defines the pairwise potential incorporating the local gradient approach. $U_{xyz}(l_{1:N}, s_{1:N})$ is the unary potential encoding the spatial connectedness of individual parcels. $V_{homo}(l_{1:N})$ is the pairwise potential encoding the homotopic constraint. $U_{sep}(l_{1:N})$ is a bookkeeping unary potential to keep the left hemisphere parcels on the left hemisphere and the right hemisphere parcels on the right hemisphere.

We note that $U_{global}(l_{1:N}, y_{1:N})$, $V_{grad}(l_{1:N})$, and $U_{xyz}(l_{1:N}, s_{1:N})$ were the same the original local-global parcellation approach (Schaefer et al., 2018). More specifically, the global similarity potential is written as

$$U_{global}(l_{1:N}, y_{1:N}) = -\sum_{n=1}^{N} \log\, p(y_n | l_n;\, \kappa_{l_n}, \mu_{l_n}) \;= -\sum_{n=1}^{N} \kappa_{l_n} y_n^T \mu_{l_n} - \sum_{n=1}^{N} \log z(\kappa_{l_n}), \quad (2)$$

where $p(y_n | l_n;\, \kappa_{l_n}, \mu_{l_n})$ is a von Mises-Fisher distribution. κ_{l_n} and μ_{l_n} are the concentration parameter and mean direction respectively for the von Mises-Fisher distribution associated with parcel l_n. In practice, as can be seen in Supplementary Methods S3, μ_{l_n} is iteratively estimated and corresponds to the mean time course of parcel l_n normalized to unit norm. Therefore, if the time course of vertex n is similar to the mean time course of parcel l_n (i.e.,

$y_n^T \mu_{l_n}$ is large), then the cost of assigning vertex n to parcellation label l_n will be smaller. Overall, the global similarity potential encourages vertices with similar time courses to be assigned to the same parcel.

The local gradient potential is written as

$$V_{grad}(l_{1:N}) = \sum_{n=1}^{N} \left(\sum_{m \in N_{q_n}} \Delta(l_n, l_m) * c * (e^{-kGrad(q_n,q_m)} - e^{-k}) \right), \quad (3)$$

where c and k are constants, N_{q_n} denotes the neighboring vertices of a vertex q_n on the surface mesh and the delta function

$$\Delta(l_n, l_m) = \begin{cases} 1 & l_n \neq l_m \\ 0 & l_n = l_m \end{cases} \quad (4)$$

Therefore, the delta function penalizes neighboring vertices with different parcellation labels. The delta function is multiplied by the gradient-weighted exponential term $e^{-kGrad(q_n,q_m)} - e^{-k}$. Here, $Grad(q_n, q_m)$ is the magnitude of RSFC gradient between vertices q_n and q_m and its value ranges from 0 to 1. Consistent with our previous study (Schaefer et al., 2018), we utilized the gradient map from a previous study (Gordon et al., 2016). If $l_n = l_m$ (i.e., vertices n and m have the same parcellatin label), then the penalty is always zero. If $l_n \neq l_m$ (i.e., vertices n and m have different parcellation labels), the penalty is weighted by the exponential term $e^{-kGrad(q_n,q_m)} - e^{-k}$. As $Grad(q_n, q_m)$ increases from zero to one, the exponential term decays from $(1 - e^k)$ to zero. Therefore, the penalty goes to zero if there is a very strong local RSFC gradient. k controls the decay rate of the exponential function and c controls for weight of the terms relative to other terms in the model. Both k and c are hyperparameters that are manually set.

Similarly, we utilize the von Mises-Fisher distribution for the spatial connectedness term:

$$U_{xyz}(l_{1:N}, s_{1:N}) = -w_{xyz} * \sum_{n=1}^{N} \log\ p(s_n | l_n;\ v_{l_n}, \tau_{l_n})$$

$$= -w_{xyz} * \left(\sum_{n=1}^{N} \tau_{l_n} s_n^T v_{l_n} + \sum_{n=1}^{N} \log z(\tau_{l_n}) \right), \qquad (5)$$

where s_n is the 3D coordinates of the n-th vertex on the fsaverage6 sphere. τ_{l_n} and v_{l_n} are the concentration parameter and mean direction respectively for the von Mises-Fisher distribution associated with parcel l_n. In practice, as can be seen in Supplementary Methods S3, v_{l_n} is iteratively estimated and corresponds to the mean spatial coordinates of parcel l_n normalized to unit norm (i.e., sphere). Therefore, if the spatial coordinates of vertex n is similar to the mean spatial coordinates of parcel l_n (i.e., $s_n^T v_{l_n}$ is large), then the cost of assigning vertex n to parcellation label l_n will be smaller. Here w_{xyz} is a tunable hyperparameter that controls the overall strength of the spatial connectedness term relative to the other terms in the cost function. The concentration parameters $\tau_{1:L}$ are also tunable. Parcels tend to get rounder as $\tau_{1:L}$ increases. Overly round parcels are not biologically realistic, so the original local-global parcellation procedure (Schaefer et al., 2018) involves an iterative procedure to adjust $\tau_{1:L}$ to ensure the spatial connectedness of individual parcels without making the parcels too round. In the current study, the procedure was simplified by initializing the model with a moderate value for $\tau_{1:L}$, and only increased the τ for spatially disconnected parcels (when such parcels emerged during the optimization procedure).

The remaining two terms $V_{homo}(l_{1:N})$ and $U_{sep}(l_{1:N})$ are necessary to achieve homotopic parcels. The homotopic pairwise potential is defined as:

$$V_{homo}(l_{1:N}) = \sum_{n=1}^{N} \left(\sum_{m \in H_{q_n}} \Delta'(l_n, l_m) \right), \qquad (6)$$

where H_{q_n} is the homotopic vertex on the opposite hemisphere and

$$\Delta'(l_n, l_m) = \begin{cases} d & l_n \text{ and } l_m \text{ are homotopic parcels} \\ 0 & l_n \text{ and } l_m \text{ are not homotopic parcels} \end{cases} \qquad (7)$$

For example, in the case of the 400-region hMRF parcellation, without loss of generality, we assume that parcels 1 to 200 are in the left hemisphere and parcels 201 to 400 are in the right hemisphere. Furthermore, we assume that parcels 1 and 201 are homotopic, parcels 2 and 202 are homotopic, etc. A larger value of d will result in greater penalty for homotopic vertices not being assigned to homotopic parcels and places a larger weight on this homotopic penalty term, relative to the other terms in the cost function.

Finally, because of the strong homotopic correlations between the hemispheres, we have an additional unary "bookkeeping" term that prevents parcellation labels from spanning the hemispheres.

$$U_{sep}(l_{1:N}) = -w_{sep}\left(\sum_{n=1}^{N_{hemi}} \log p_{lh}(l_n) + \sum_{n=N_{hemi}+1}^{N} \log\ p_{rh}(l_n)\right), \quad (8)$$

where $N_{hemi} = N/2$ and

$$p_{lh}(l_n) = \begin{cases} \frac{1}{N_{hemi}} & if\ l_n = 1,\ 2,\ \cdots, N_{hemi} \\ 0 & \text{otherwise} \end{cases} \quad (9)$$

$$p_{rh}(l_n) = \begin{cases} \frac{1}{N_{hemi}} & if\ l_n = N_{hemi}+1,\ N_{hemi}+2,\ ,\cdots, N \\ 0 & \text{otherwise} \end{cases} \quad (10)$$

To explain the above equations, let's consider the case of the 400-region hMRF parcellation, so N_{hemi} = 200. Without loss of generality, we assume that parcels 1 to 200 are in the left hemisphere and parcels 201 to 400 are in the right hemisphere. Eq. (9) assigns zero probability (or infinite penalty) if a left hemisphere vertex is assigned to a right hemisphere parcel (i.e., parcels 201 to 400), while Eq. (10) assigns zero probability (or infinite penalty) if a right hemisphere vertex is assigned to a left hemisphere parcel (i.e., parcels 1 to 200). w_{sep} is a hyperparameter that is simply set to a very big number to prevent any parcel from spanning across the hemispheres.

S3. Model estimation

Given observed spatial coordinates $s_{1:N}$, the fMRI time courses $y_{1:N}$, and fixed hyperparameters $c, d, k, w_{sep}, w_{xyz}$ and $\tau_{1:L}$, we can estimate labels $l_{1:N}$, concentration

parameter κ_{l_n}, and mean directions υ_{l_n} and μ_{l_n}using the maximum-a-posteriori (MAP) principle:

$$\underset{l_{1:N},\mu_{1:L},\kappa_{1:L},\upsilon_{1:L}}{\operatorname{argmax}} \log p(l_{1:N}, \kappa_{1:L}, \upsilon_{1:L}, \mu_{1:L} \mid s_{1:N},\ y_{1:N}, c, d, k, w_{xyz}, w_{sep}, \tau_{1:L}) \qquad (11)$$

We can achieve the optimization by block coordinate descent. At each iteration, given $l_{1:N}$, we can estimate $\{\kappa_{1:L}, \upsilon_{1:L}, \mu_{1:L}\}$, where:

$$\mu_l = \frac{\sum_{n=1}^{N} y_n \delta(l_n, l)}{||\sum_{n=1}^{N} y_n \delta(l_n, l)||} \qquad (12)$$

$$\kappa_l = \frac{(M-2)\Gamma_l}{2-\Gamma_l^2} + \frac{(M-1)\Gamma_l}{2(M-2)}, \text{where } \Gamma_l = \frac{1}{N}\sum_{n=1}^{N} \delta(l_n, l) y_n^T \mu_l \qquad (13)$$

$$\upsilon_l = \frac{\sum_{n=1}^{N} s_n \delta(l_n, l)}{||\sum_{n=1}^{N} s_n \delta(l_n, l)||} \quad , \qquad (14)$$

where $\delta(l_n, l) = 1\ if\ l_n = l$ and zero otherwise. M indicates the length of the time course y_n. $||\cdot||$ stands for L_2 norm. Therefore, μ_l is obtained by summing over the time courses of all vertices assigned to parcel l, and then normalized to unit norm; similarly, υ_l is obtained by summing over the spatial coordinates of vertices assigned to parcel l, and then normalized to unit norm.

On the other hand, given $\{\kappa_{1:L}, \upsilon_{1:L}, \mu_{1:L}\}$, we can use graph cuts (Delong et al., 2012) to estimate the labels $l_{1:N}$. Here we use the alpha expansion graph cut algorithm, consistent with our previous study (Schaefer et al., 2018). Given an initialization of the labels $l_{1:N}$ (and fixed values of c, d, k, w_{sep}, w_{xyz} and $\tau_{1:L}$), we can iterate between Eqs. (12) to (14) and the alpha expansion algorithm until convergence to estimate $l_{1:N}, \kappa_{1:L}, \upsilon_{1:L}, \mu_{1:L}$. We refer to this iterative optimization procedure as the **MAP1** algorithm. Supplementary Section S4 provides more details about the derivation of the MAP1 algorithm.

Recall that d is the hyperparameter for the homotopic constraint in Eq. (7). If d is too small, then there will not be homotopic parcels. If d is too big, then the homotopic parcels on both

hemispheres will be identical. Therefore, we want d to be just big enough so each parcel has a homotopic parcel on the other hemisphere, but not so big that the homotopic parcels are identical on both hemispheres. On the other hand, $\tau_{1:L}$ are the hyperparameters for the spatial connectedness constraint in Eq. (5). We want $\tau_{1:L}$ to be large enough so that parcels are spatially connected, but not so large that they become too round. To achieve these tradeoffs, d and $\tau_{1:L}$ were set to some initial values. The MAP1 algorithm was then run until convergence. The initial value of d was set to be moderately large, so that after MAP1 converged, parcels remained homotopic. We then reduced d by half and re-ran the MAP1 algorithm (initializing $\{\kappa_{1:L}, \upsilon_{1:L}, \mu_{1:L}\}$ with their previous estimates). We continued reducing d (and re-running the MAP1 algorithm) until parcels no longer become homotopic, in which case, we increased d again. Similarly, $\tau_{1:L}$ were initialized to a moderate value. After the MAP1 algorithm converged, we increased the τ of spatially disconnected parcels and re-ran the MAP1 algorithm. This process was repeated until all parcels were spatially connected. We refer to the repeated running of MAP1 algorithm and the automatic tuning of d and $\tau_{1:L}$ as the **MAP2** algorithm.

Overall, the entire algorithm proceeded as follows. For fixed values of c, k, w_{sep} and w_{xyz} and initial values of d and $\tau_{1:L}$, we randomly initialized parcels on the left hemisphere and then reflected the parcels on the right hemisphere based on the vertex-wise homotopic correspondence obtained from mris_left_right_register. We then ran MAP2 algorithm until convergence. We repeated with different random initializations of the initial parcels. The initialization that led to the best cost function value in terms of the global similarity and local gradient terms was selected as the final estimate. We referred to this as the **MAP3** algorithm

S4. MAP Estimation

This section derives the MAP1 algorithm (from Section S3) in detail. Given observed spatial coordinates $s_{1:N}$, the fMRI time courses $y_{1:N}$, and fixed hyperparameters $c, d, k, w_{sep}, w_{xyz}$ and $\tau_{1:L}$, we can estimate parcellation labels $l_{1:N}$, concentration parameter $\kappa_{1:L}$, mean directions $\upsilon_{1:L}$ and mean directions $\mu_{1:L}$ using the maximum-a-posteriori (MAP) principle:

$$\underset{l_{1:N},\mu_{1:L},\kappa_{1:L},\nu_{1:L}}{\operatorname{argmax}} \log p(l_{1:N}, \kappa_{1:L}, \upsilon_{1:L}, \mu_{1:L} \mid s_{1:N},\ y_{1:N};\ c, d, k, w_{xyz}, w_{sep}, \tau_{1:L}) \qquad (15)$$

Note that Eq. (15) is the same as Eq. (11) in Section S3. Assuming a uniform prior on $\kappa_{1:L}, \upsilon_{1:L}, \mu_{1:L}$, we can write Eq. (15) as:

$$\underset{l_{1:N},\mu_{1:L},\kappa_{1:L},\nu_{1:L}}{\operatorname{argmax}} \log p(l_{1:N}, s_{1:N},\ y_{1:N} | \kappa_{1:L}, \upsilon_{1:L}, \mu_{1:L}, c, d, k, w_{xyz}, w_{sep}, \tau_{1:L}) \quad (16)$$

We can then plug in Eq. (1), so the above equation becomes:

$$\underset{l_{1:N},\mu_{1:L},\kappa_{1:L},\nu_{1:L}}{\operatorname{argmax}} \frac{1}{Z} \exp\{ -U_{global}(l_{1:N}, y_{1:N}) - V_{grad}(l_{1:N}) - U_{xyz}(l_{1:N}, s_{1:N}) - V_{homo}(l_{1:N}) - U_{sep}(l_{1:N}) \} \quad (17)$$

Z is just a normalization term (that is not dependent on $l_{1:N}, \kappa_{1:L}, \upsilon_{1:L}, \mu_{1:L}$), so we can just drop Z from the above maximization problem. We will also expand each term in Eq. (17) following Eq. (2) to Eq. (10), apply the log (to cancel the exp), and finally flip the sign of the maximization problem into a minimization problem.

$$\begin{aligned}
\underset{l_{1:N},\mu_{1:L},\kappa_{1:L},\nu_{1:L}}{\operatorname{argmin}} \quad & -\left(\sum_{n=1}^{N} \kappa_{l_n} y_n^T \mu_{l_n} + \sum_{n=1}^{N} \log z(\kappa_{l_n}) \right) \\
& + \sum_{n=1}^{N} \left(\sum_{m \in N_{q_n}} \Delta(l_n, l_m) * c * \left(e^{-kGrad(q_n, q_m)} - e^{-k} \right) \right) \\
& - w_{xyz} * \left(\sum_{n=1}^{N} \tau_{l_n} s_n^T \upsilon_{l_n} + \sum_{n=1}^{N} \log z(\tau_{l_n}) \right) + \sum_{n=1}^{N} \left(\sum_{m \in H_{q_n}} \Delta'(l_n, l_m) \right) \\
& - w_{sep} * \left(\sum_{n=1}^{N_{lh}} \log p_{lh}(l_n) + \sum_{n=N_{lh}+1}^{N} \log p_{rh}(l_n) \right) \qquad (18)
\end{aligned}$$

To optimize Eq. (18), we will alternate between estimating parcellation labels $l_{1:N}$ (while fixing $\kappa_{1:L}, \upsilon_{1:L}, \mu_{1:L}$) and estimating von-Mises distribution parameters $\kappa_{1:L}, \upsilon_{1:L}, \mu_{1:L}$ (while fixing $l_{1:N}$).

To estimate $l_{1:N}$ (while fixing $\kappa_{1:L}, \upsilon_{1:L}, \mu_{1:L}$), we note that the global minimum is NP-hard to estimate. The alpha-expansion graph cut algorithm allows the estimation of a locally optimal solution whose cost is guaranteed to be close to the global optimum (Boykov et al. 2001).

Furthermore, alpha expansion cannot be used given the negative unary terms in Eq. (18), so a large positive constant M is added to offset the negative terms. The potentials were also divided by the total number of vertices N to avoid numerical overflow, thus yielding the final cost function for estimating $l_{1:N}$ (while fixing $\kappa_{1:L}, \upsilon_{1:L}, \mu_{1:L}$):

$$\begin{aligned}\underset{l_{1:N}}{\operatorname{argmin}} \quad & -\frac{1}{N}\left(\sum_{n=1}^{N} \kappa_{l_n} y_n^T \mu_{l_n} + \sum_{n=1}^{N} \log z(\kappa_{l_n})\right) \\ & + \frac{1}{N}\sum_{n=1}^{N}\left(\sum_{m \in N_{q_n}} \Delta(l_n, l_m) * c * \left(e^{-kGrad(q_n, q_m)} - e^{-k}\right)\right) \\ & - w_{xyz} * \frac{1}{N}\left(\sum_{n=1}^{N} \tau_{l_n} s_n^T \upsilon_{l_n} + \sum_{n=1}^{N} \log z(\tau_{l_n})\right) \\ & + \frac{1}{N}\sum_{n=1}^{N}\left(\sum_{m \in H_{q_n}} \Delta'(l_n, l_m)\right) \\ & - w_{sep} * \frac{1}{N}\left(\sum_{n=1}^{N_{lh}} \log p_{lh}(l_n) + \sum_{n=N_{lh}+1}^{N} \log p_{rh}(l_n)\right) + M \end{aligned} \tag{19}$$

Alpha expansion was utilized to optimize Eq. (19) with respect to parcellation labels $l_{1:N}$.

To estimate $\kappa_{1:L}, \upsilon_{1:L}, \mu_{1:L}$ (while fixing $l_{1:N}$) is equivalent to maximum likelihood estimation of von Mises-Fisher distributions. Under the constraints that $\mu_l^T \mu_l = 1$, $\upsilon_l^T \upsilon_l = 1$ and $\kappa > 0$, we differentiate Eq. (18) with respect to $\{\kappa_{1:L}, \upsilon_{1:L}, \mu_{1:L}\}$ and set the derivatives to zero, we get (Lashkari et al. 2010):

$$\mu_l = \frac{\sum_{n=1}^{N} y_n \delta(l_n, l)}{||\sum_{n=1}^{N} y_n \delta(l_n, l)||} \tag{20}$$

$$\kappa_l = \frac{(M-2)\Gamma_l}{2 - \Gamma_l^2} + \frac{(M-1)\Gamma_l}{2(M-2)}, \text{where } \Gamma_l = \frac{1}{N}\sum_{n=1}^{N} \delta(l_n, l) y_n^T \mu_l \tag{21}$$

$$\upsilon_l = \frac{\sum_{n=1}^{N} s_n \delta(l_n, l)}{||\sum_{n=1}^{N} s_n \delta(l_n, l)||}, \tag{22}$$

which are the same as Eq. (12) to Eq. (14). Overall, the MAP1 algorithm iterates between applying alpha expansion on Eq. (19) and computing Eq. (20) to Eq. (22).

S5. Hyperparameters of the hMRF model

This section discusses the settings of various hyperparameters in the hMRF model. For both benchmarking and the generation of a final set of parcellations, the MAP3 algorithm was ran with 1000 random initializations. As previously mentioned in Section S2, w_{sep} was simply set to be a very large number. $\tau_{1:L}$ was initialized with a function to ensure that the normalization term in von Mises-Fisher distribution does not trigger numerical overflow in the Bessel function, yielding τ to be equal to 25.742.

That left us with c, k, w_{xyz} and the initial value of d as the true "free" hyperparameters. The settings of these hyperparameters differed when the dimensionality of the input data $y_{1:N}$, or the number of parcels L changed. For the purpose of comparisons with other publicly available parcellations, the hyperparameters c, k, w_{xyz} and initial value of d were fixed as 80k, 15, 100k and 16,000 respectively, based on visual inspection of the parcellations estimated from the GSP training set.

For the generation of the final set of parcellations for public release, different sets of hyperparameters were used for different resolutions. Hyperparameters were selected based on visual inspection of the parcellations in the full GSP dataset. Architectonic geodesic distances, visuotopic geodesic distances and resting-homogeneity in the GSP dataset were also computed to ensure the final parcellations were both visually and quantitatively compelling. For the 100-region parcellation, c, k, w_{xyz} and initial value of d were set to be 10k, 15, 100k and 20k respectively. For the 200-region parcellation, c, k, w_{xyz} and initial value of d were set to be 110k, 15, 120k and 25k respectively. For the 300-region parcellation, c, k, w_{xyz} and initial value of d were set to be 130k, 15, 130k and 30k respectively. For the 400-region parcellation, c, k, w_{xyz} and initial value of d were set to be 140k, 15, 150k and 50k respectively. For the 500-region parcellation, c, k, w_{xyz} and initial value of d were set to be 180k, 15, 250k and 50k respectively. For the 600-region to 1000-region parcellations, c, k, w_{xyz} and initial value of d were set to be 200k, 15, 300k and 50k respectively.

Supplementary Results

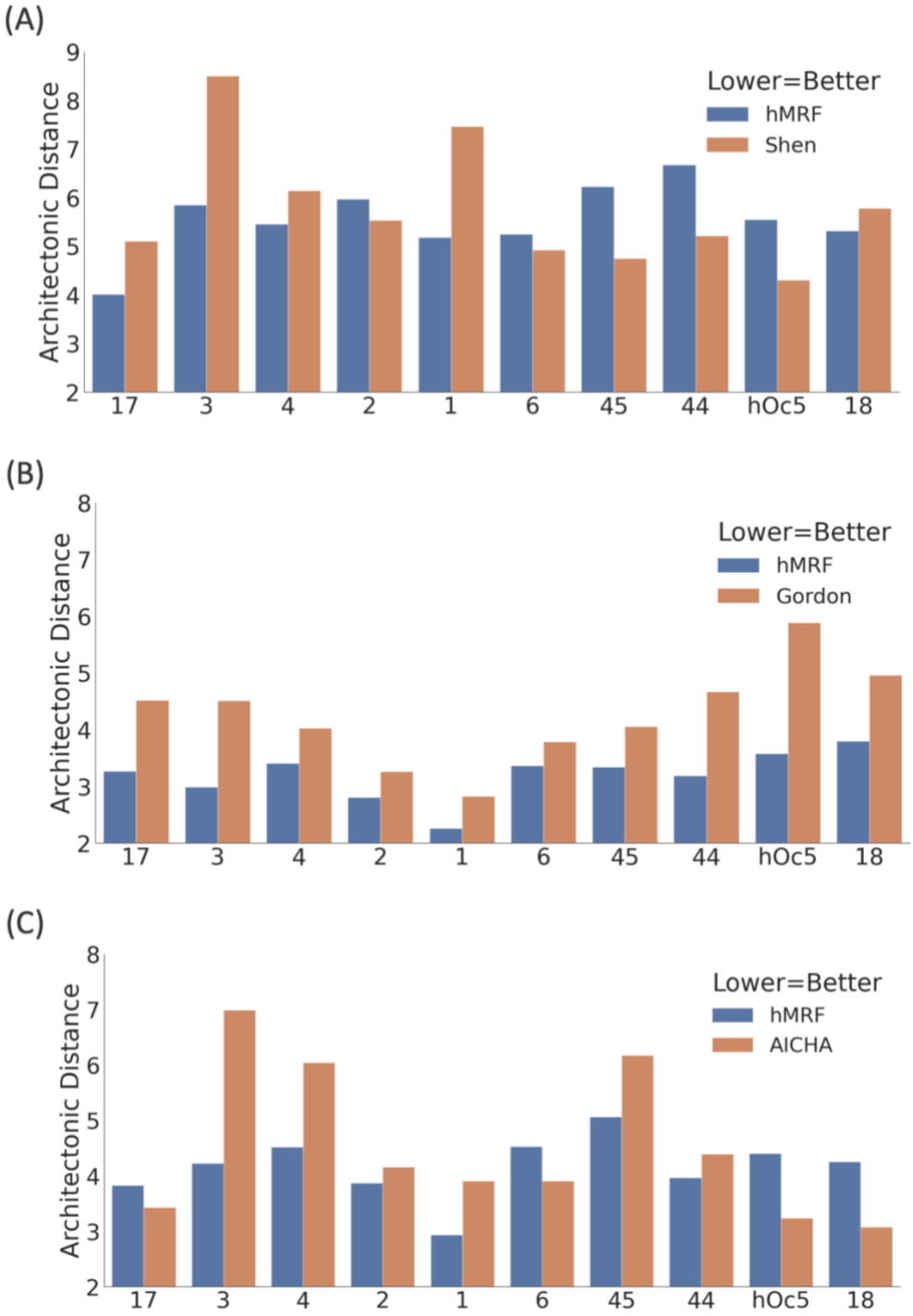

Figure S1. Distance between parcellation and architectonic boundaries as measured by average geodesic distance (mm). Lower distance indicates better agreement. Number of parcels was matched between the publicly available parcellations and corresponding hMRF parcellations. Figure continues next page.

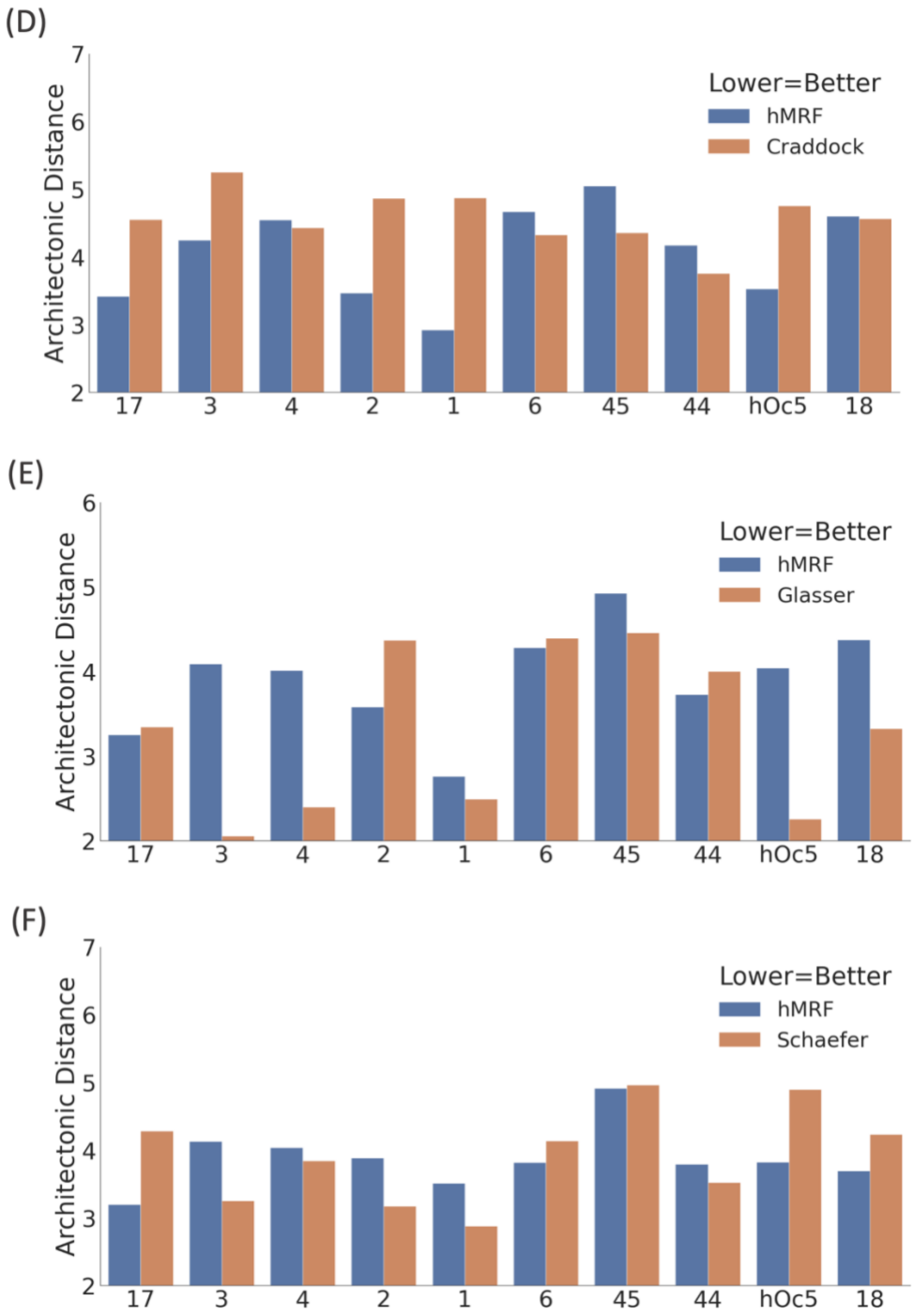

Figure S1 (cont). Distance between parcellation and architectonic boundaries as measured by average geodesic distance (mm). Lower distance indicates better agreement. Number of parcels was matched between the publicly available parcellations and corresponding hMRF parcellations. The hMRF approach generated parcellations that achieved (A) similar architectonic distance to Shen ($p = 0.441$ uncorrected), (B) better distance than Gordon ($p \approx 0$ uncorrected), (C) similar distance to AICHA ($p = 0.210$ uncorrected), (D) better distance than Craddock ($p = 0.031$ uncorrected), (E) worse distance than Glasser ($p = 0.032$ uncorrected), and (F) similar distance to Schaefer ($p = 0.835$). After correcting for multiple comparisons with a false discovery rate (FDR) of $q < 0.05$, only the comparison with the Gordon parcellation remained significant. Overall, the hMRF parcellations exhibited architectonic

alignment comparable with (or better than) other parcellations. We note that the parcellations comprised 197, 333, 341, 355, 360 and 400 parcels in subplots A, B, C, D, E and F respectively. Therefore, comparisons between subplots are not meaningful because more parcels lead to more boundary vertices, and therefore lower geodesic distances (on average).

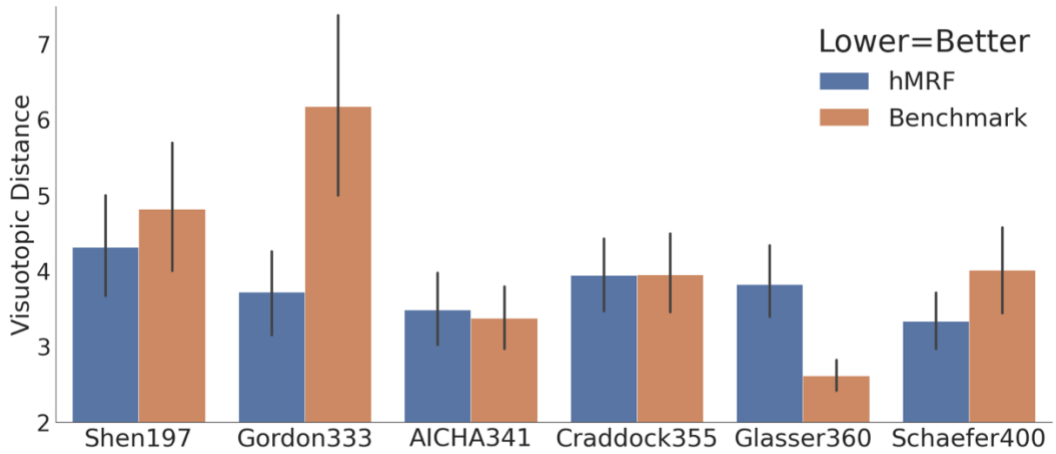

Figure S2. Distance between parcellation and visuotopic boundaries (Abdollahi et al., 2014) as measured by average geodesic distance (mm). Lower distance indicates better agreement. Number of parcels was matched between the publicly available parcellations and corresponding hMRF parcellations. The hMRF parcellations achieve (A) similar visuotopic distance to Shen ($p = 0.279$), (B) better distance to Gordon ($p \approx 0$), (C) similar distance to ACIHA ($p = 0.731$), (D) similar distance to Craddock ($p = 0.986$), (E) worse distance to Glasser ($p \approx 0$) and (F) similar distance to Schaefer ($p = 0.083$). After correcting for multiple comparisons with a FDR of $q < 0.05$, the comparisons with the Gordon and Glasser parcellations remained significant. We note that the Glasser parcellation was derived with a semi-automated algorithm that required an anatomist to manually select multi-modal information to match prior knowledge of areal boundaries. Overall, the hMRF parcellations achieved visuotopic alignment comparable with (or better than) other fully automatic approaches. Like before, comparisons between parcellations with different number of parcels (e.g., Shen197 versus Gordon333) are not meaningful.

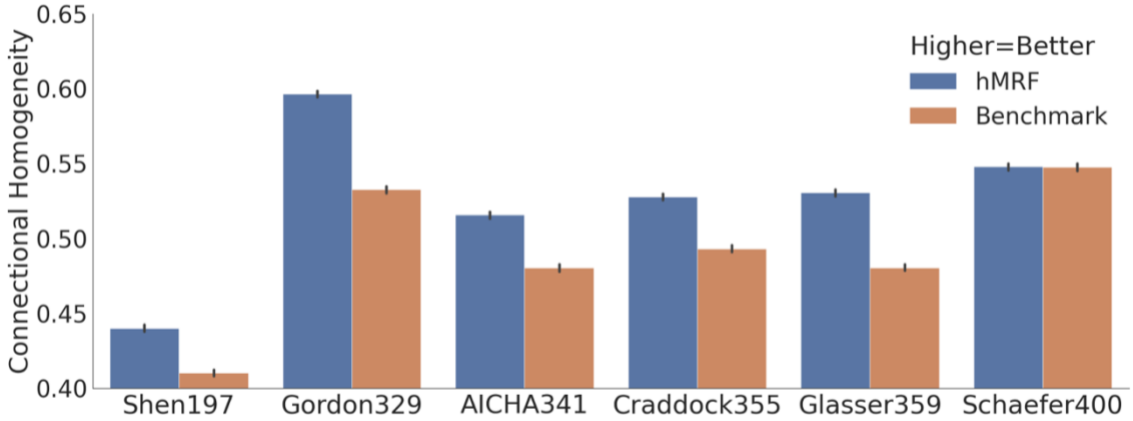

Figure S3. Resting-fMRI homogeneity computed with the GSP test set (N = 739) in fsaverage space. The hMRF parcellations achieved comparable resting-fMRI homogeneity with the Schaefer parcellation. On the other hand, the hMRF parcellations were more homogeneous than 5 parcellations.

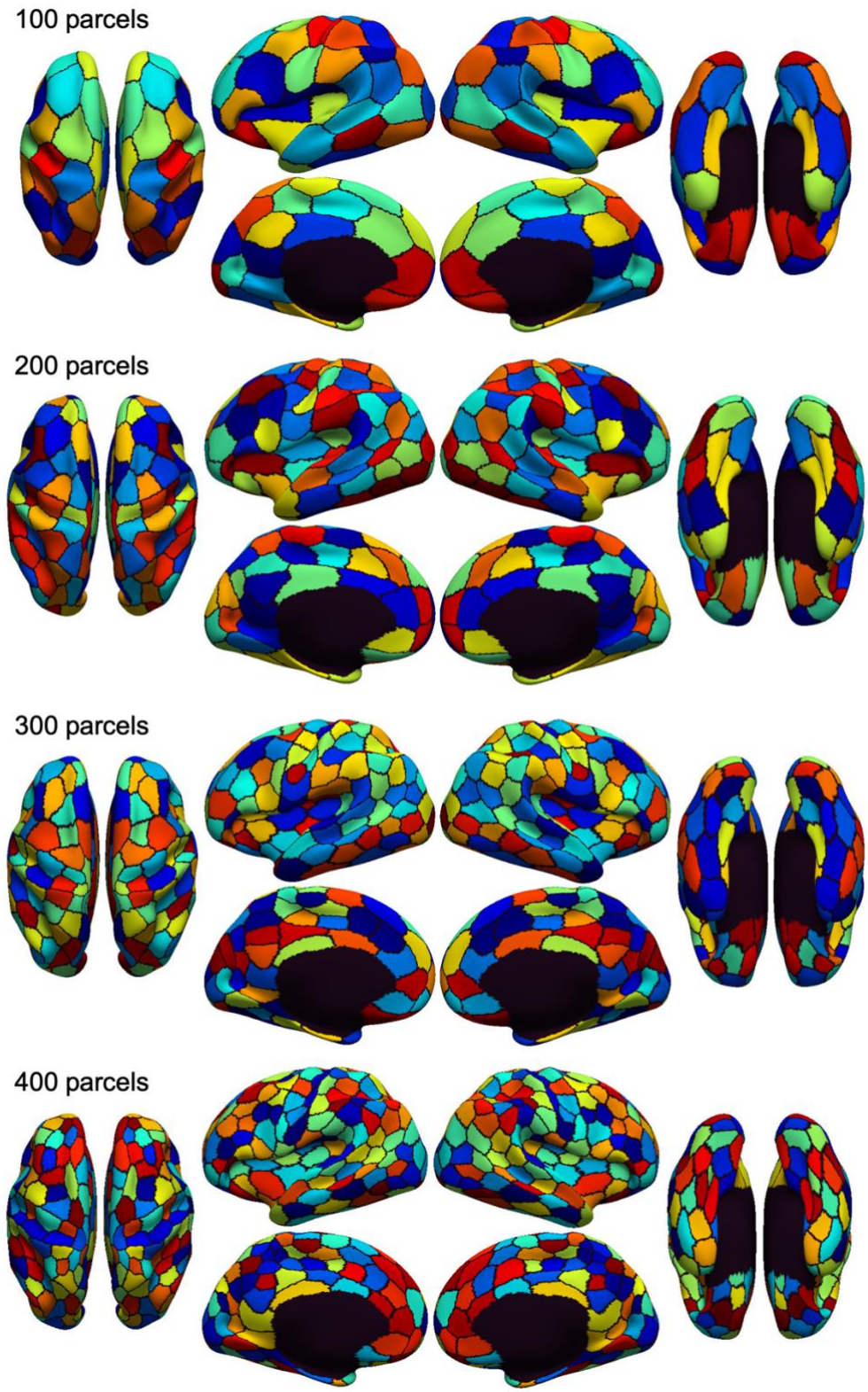

Figure S4. Cerebral cortex parcellations with 100 to 400 parcels based on the full GSP dataset of 1479 subjects. Homotopic parcels have identical colors. Figure continues next page.

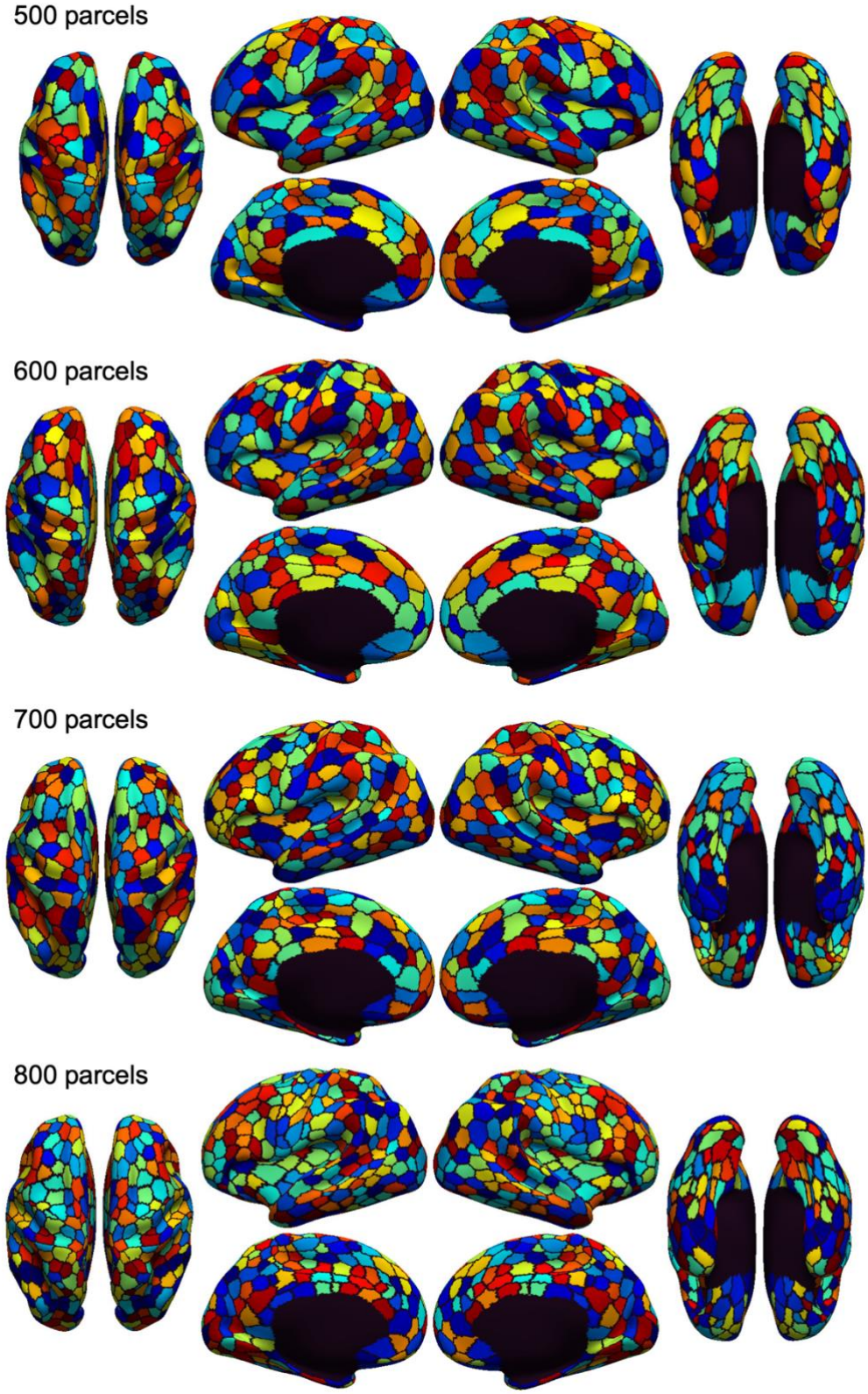

Figure S4 (cont). Cerebral cortex parcellations with 500 to 800 parcels based on the GSP dataset of 1479 subjects. Homotopic parcels have identical colors. Figure continues next page.

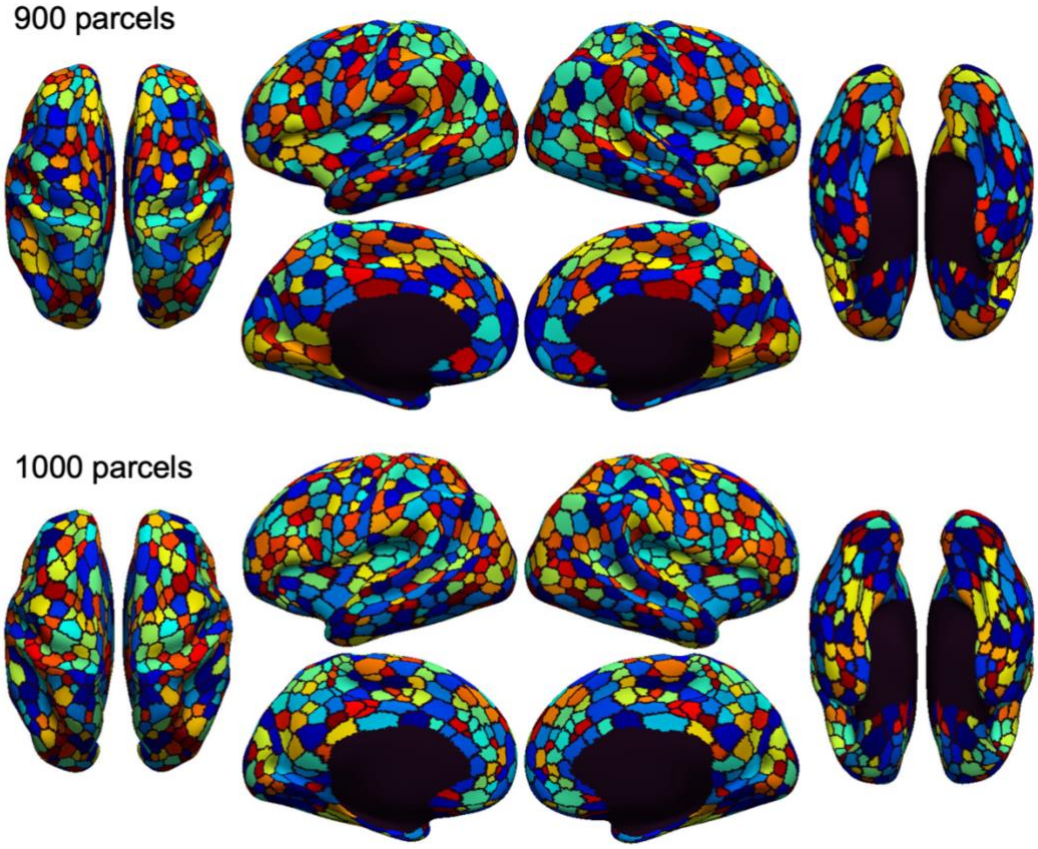

Figure S4 (cont). Cerebral cortex parcellations with 900 to 1000 parcels based on the full GSP dataset of 1479 subjects. Homotopic parcels have identical colors.

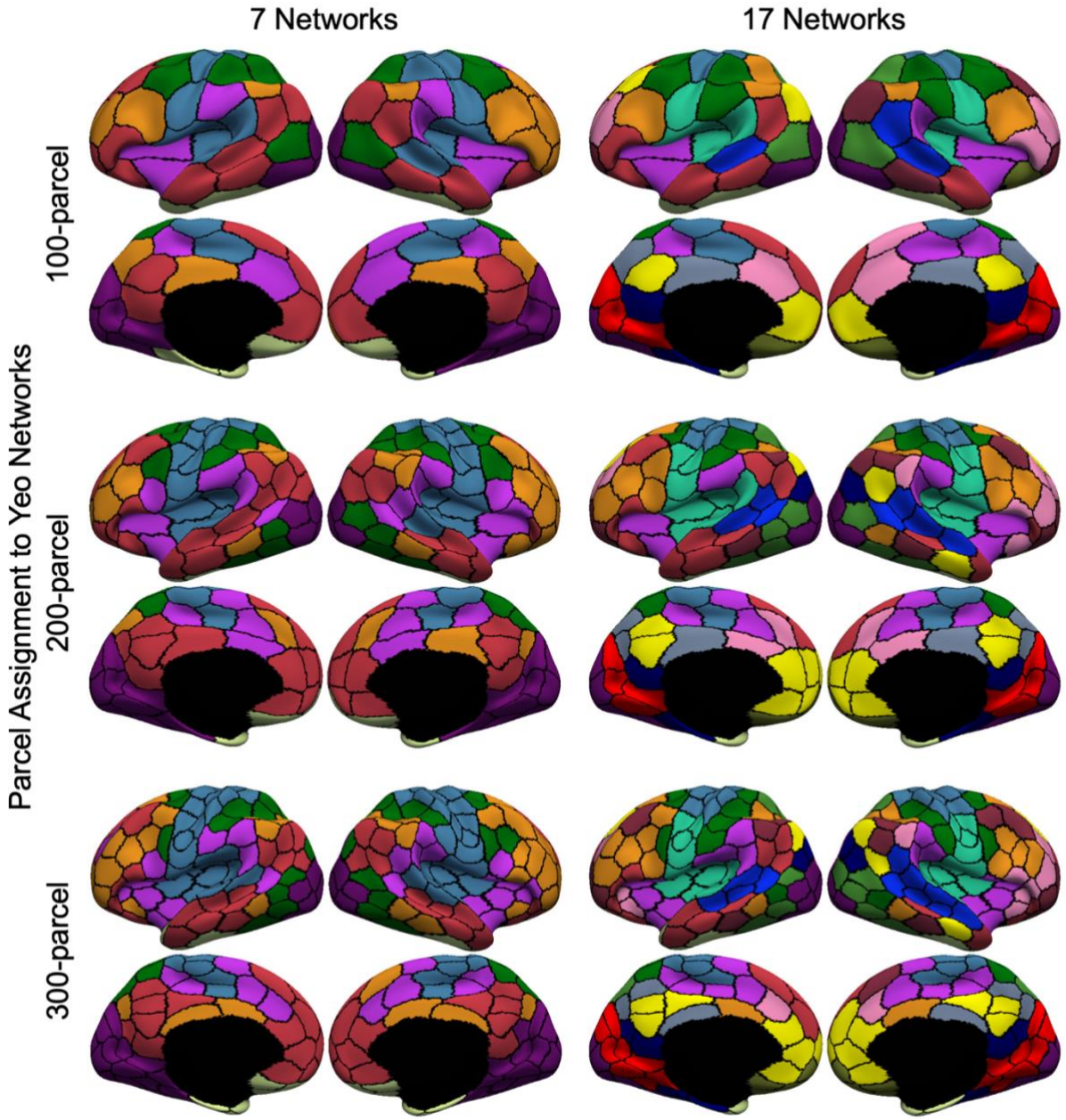

Figure S5. Assignment of parcels to 7 or 17 networks (Yeo et al., 2011) for hMRF parcellations with 100 to 300 regions. Note that the 400-region parcellation is shown in the main text (Figure 5). Figure continues next page.

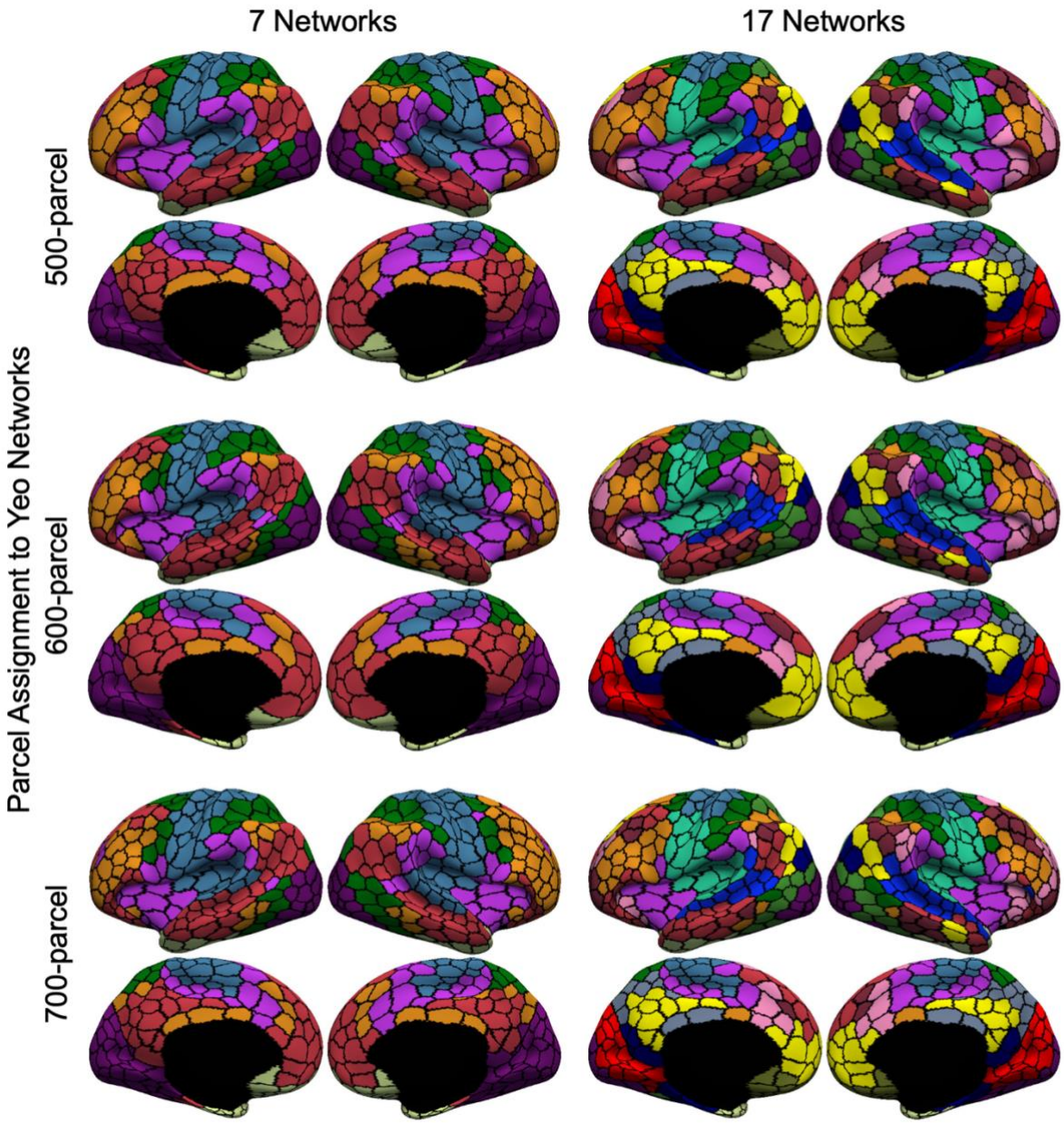

Figure S5 (cont). Assignment of parcels to 7 or 17 networks (Yeo et al., 2011) for hMRF parcellations with 500 to 700 regions. Figure continues next page.

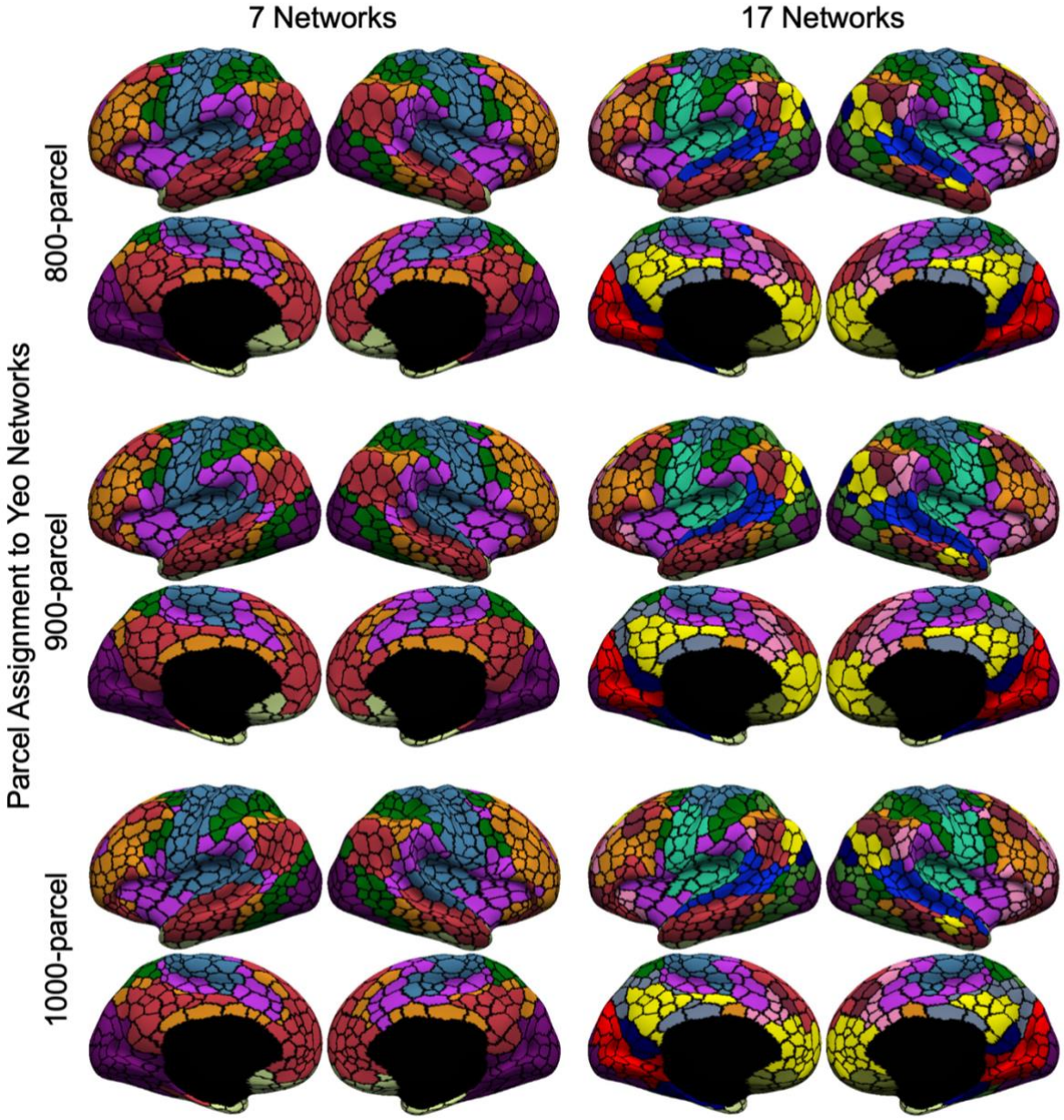

Figure S5 (cont). Assignment of parcels to 7 or 17 networks (Yeo et al., 2011) for hMRF parcellations with 800 to 1000 regions.

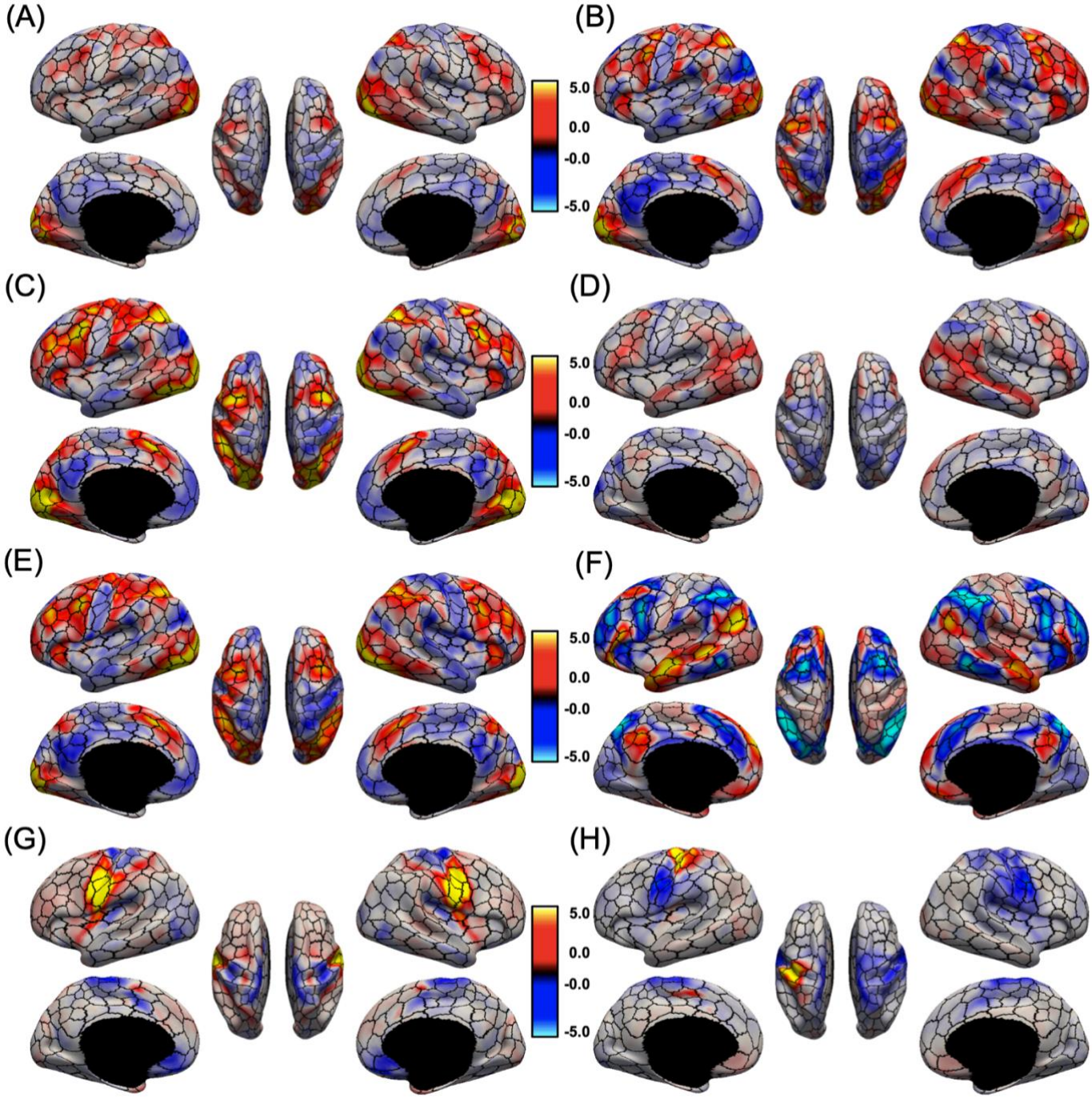

Figure S6. Group-average task activation maps of (A) emotion (faces - fixation), (B) gambling (punishment - fixation), (C) relational (matching - fixation), (D) social (theory of mind - random) and (E) working memory (2 back body - fixation), (F) language (story – math), (G) tongue motion (tongue – average motor), (H) right finger tapping (right finger – average motor) from the HCP dataset overlaid on (black) boundaries of 400-area cerebral cortex parcellation. Activations were unthresholded.

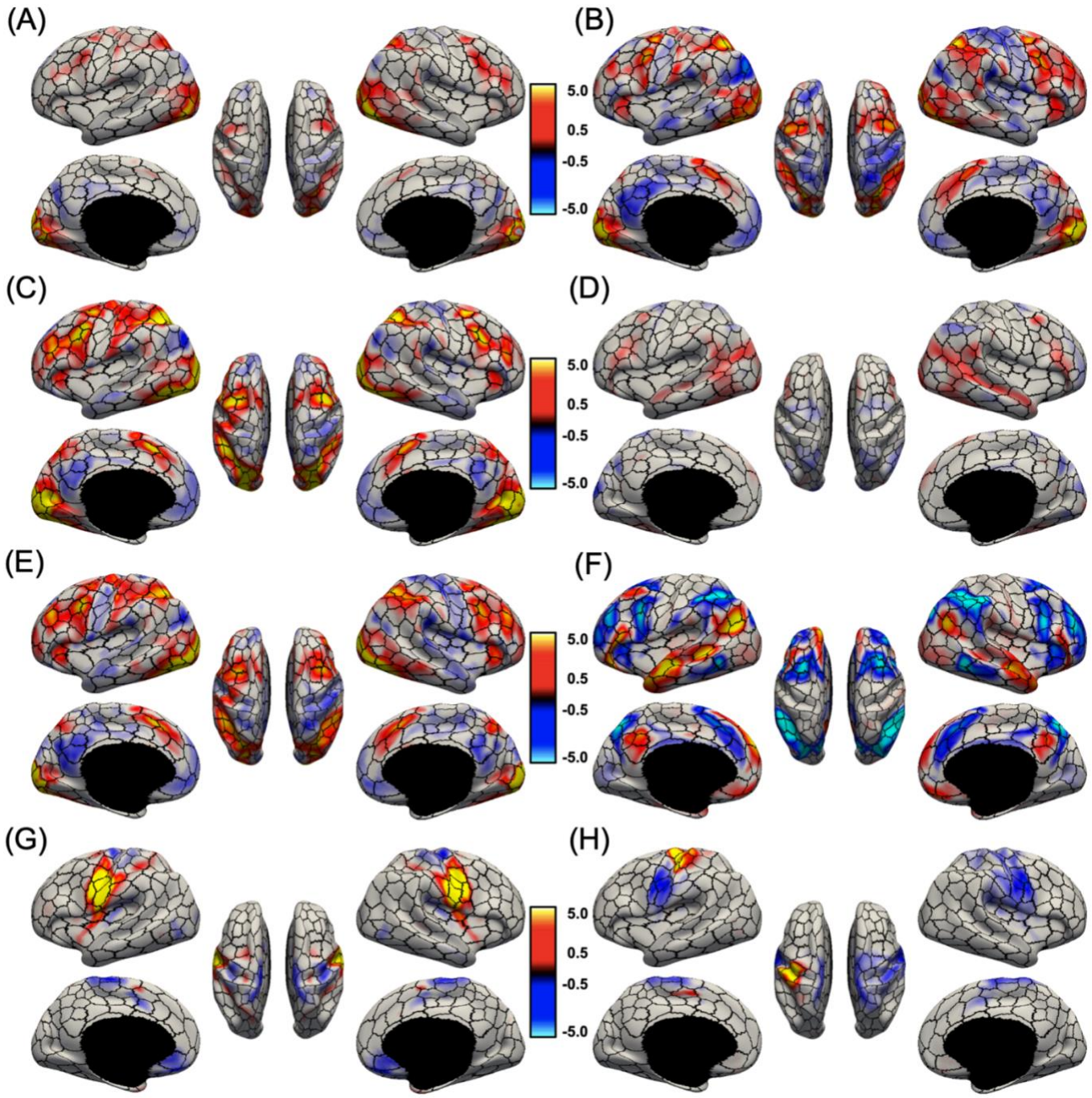

Figure S7. Group-average task activation maps of (A) emotion (faces - fixation), (B) gambling (punishment - fixation), (C) relational (matching - fixation), (D) social (theory of mind - random) and (E) working memory (2 back body - fixation), (F) language (story – math), (G) tongue motion (tongue – average motor), (H) right finger tapping (right finger – average motor) from the HCP dataset overlaid on (black) boundaries of 400-area cerebral cortex parcellation. Activations were thresholded at ±0.5.

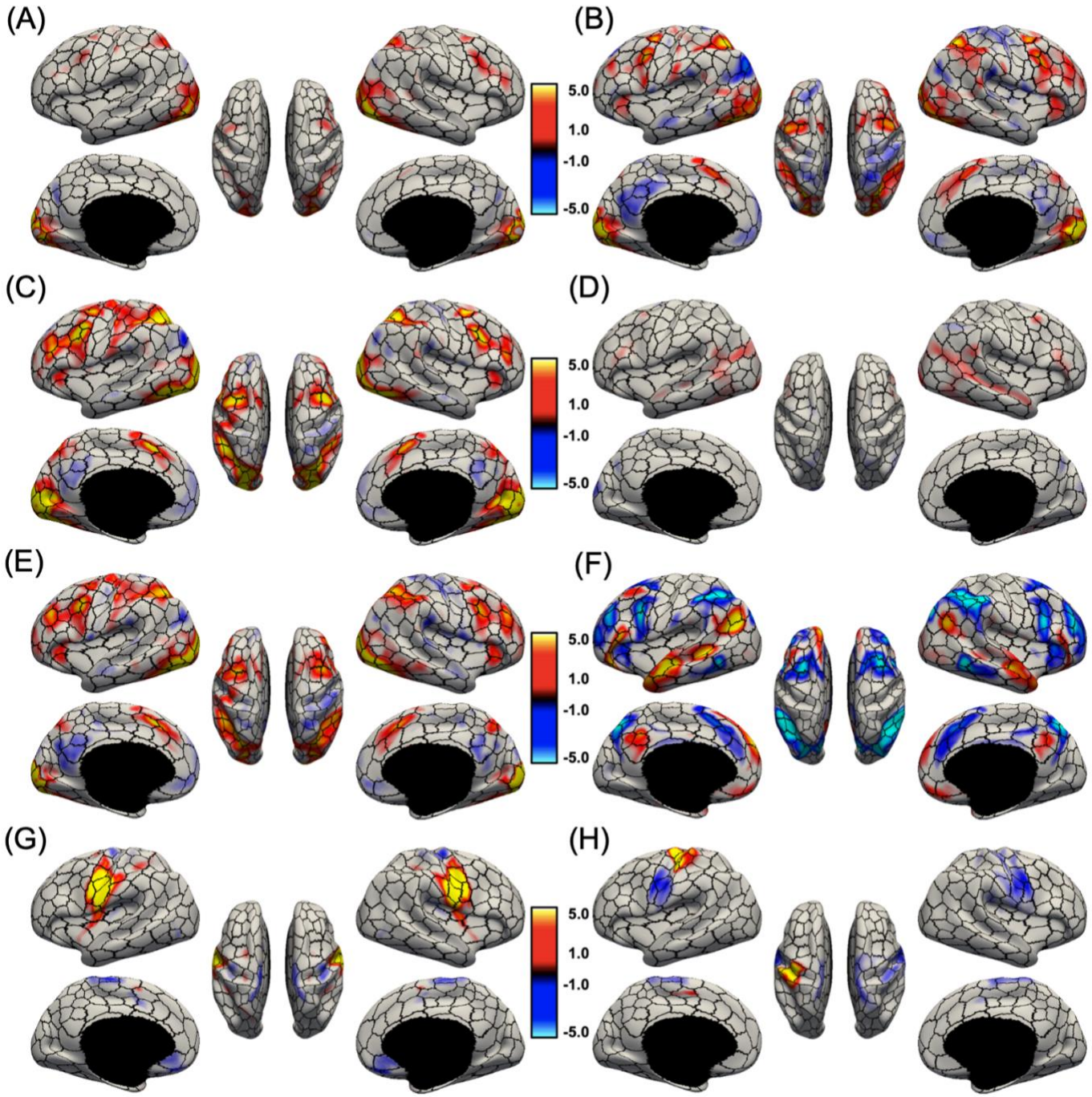

Figure S8. Group-average task activation maps of (A) emotion (faces - fixation), (B) gambling (punishment - fixation), (C) relational (matching - fixation), (D) social (theory of mind - random) and (E) working memory (2 back body - fixation), (F) language (story – math), (G) tongue motion (tongue – average motor), (H) right finger tapping (right finger – average motor) from the HCP dataset overlaid on (black) boundaries of 400-area cerebral cortex parcellation. Activations were thresholded at ±1.0.

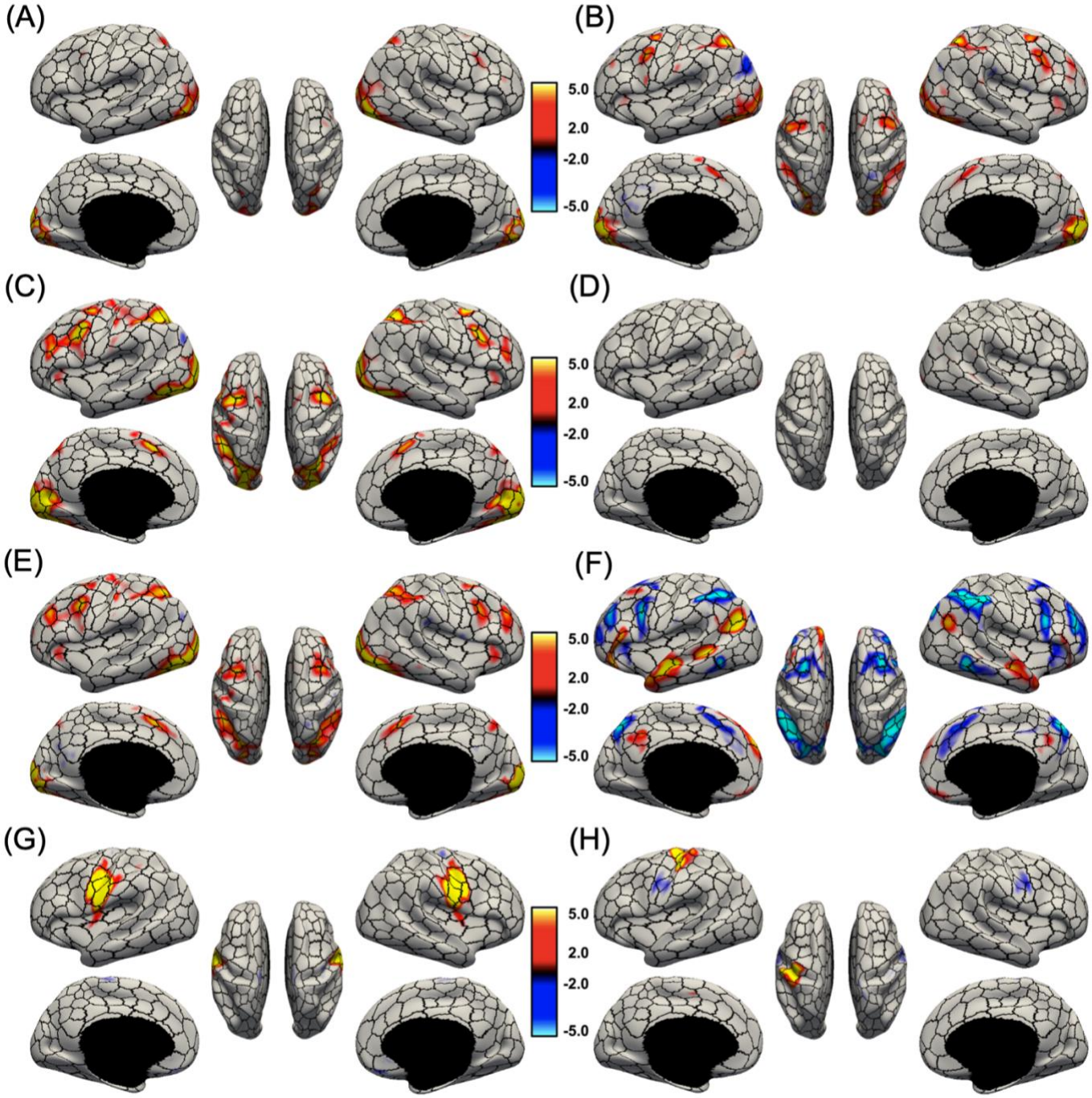

Figure S9. Group-average task activation maps of (A) emotion (faces - fixation), (B) gambling (punishment - fixation), (C) relational (matching - fixation), (D) social (theory of mind - random) and (E) working memory (2 back body - fixation), (F) language (story – math), (G) tongue motion (tongue – average motor), (H) right finger tapping (right finger – average motor) from the HCP dataset overlaid on (black) boundaries of 400-area cerebral cortex parcellation. Activations were thresholded at ±2.0.

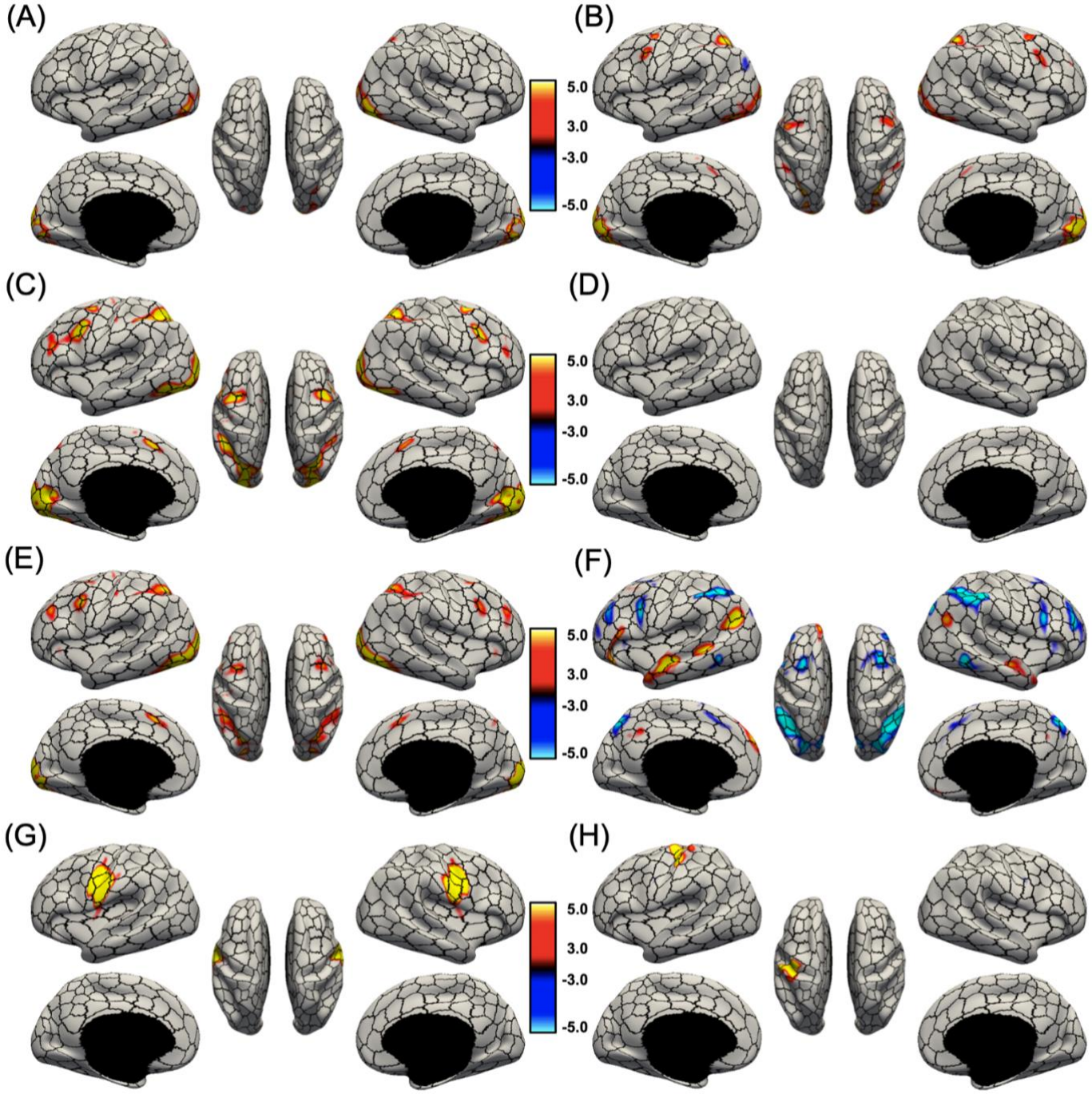

Figure S10. Group-average task activation maps of (A) emotion (faces - fixation), (B) gambling (punishment - fixation), (C) relational (matching - fixation), (D) social (theory of mind - random) and (E) working memory (2 back body - fixation), (F) language (story – math), (G) tongue motion (tongue – average motor), (H) right finger tapping (right finger – average motor) from the HCP dataset overlaid on (black) boundaries of 400-area cerebral cortex parcellation. Activations were thresholded at ±3.0.

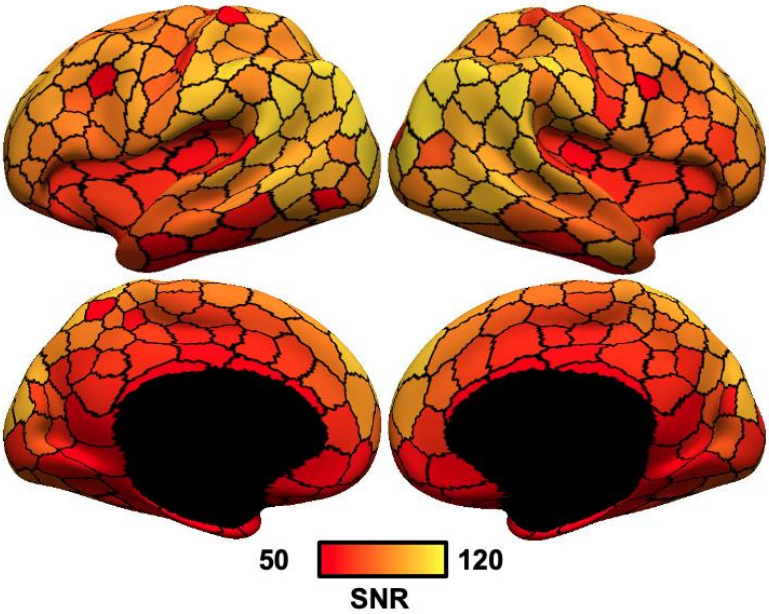

Figure S11. HCP signal-to-noise ratio (SNR) map. SNR was computed for each vertex as the mean fMRI signal divided by the standard deviation of the fMRI signal. The vertex-wise SNR map was averaged within each parcel and shown in this figure. Observe the strong anterior-to-posterior SNR gradient in the HCP dataset.

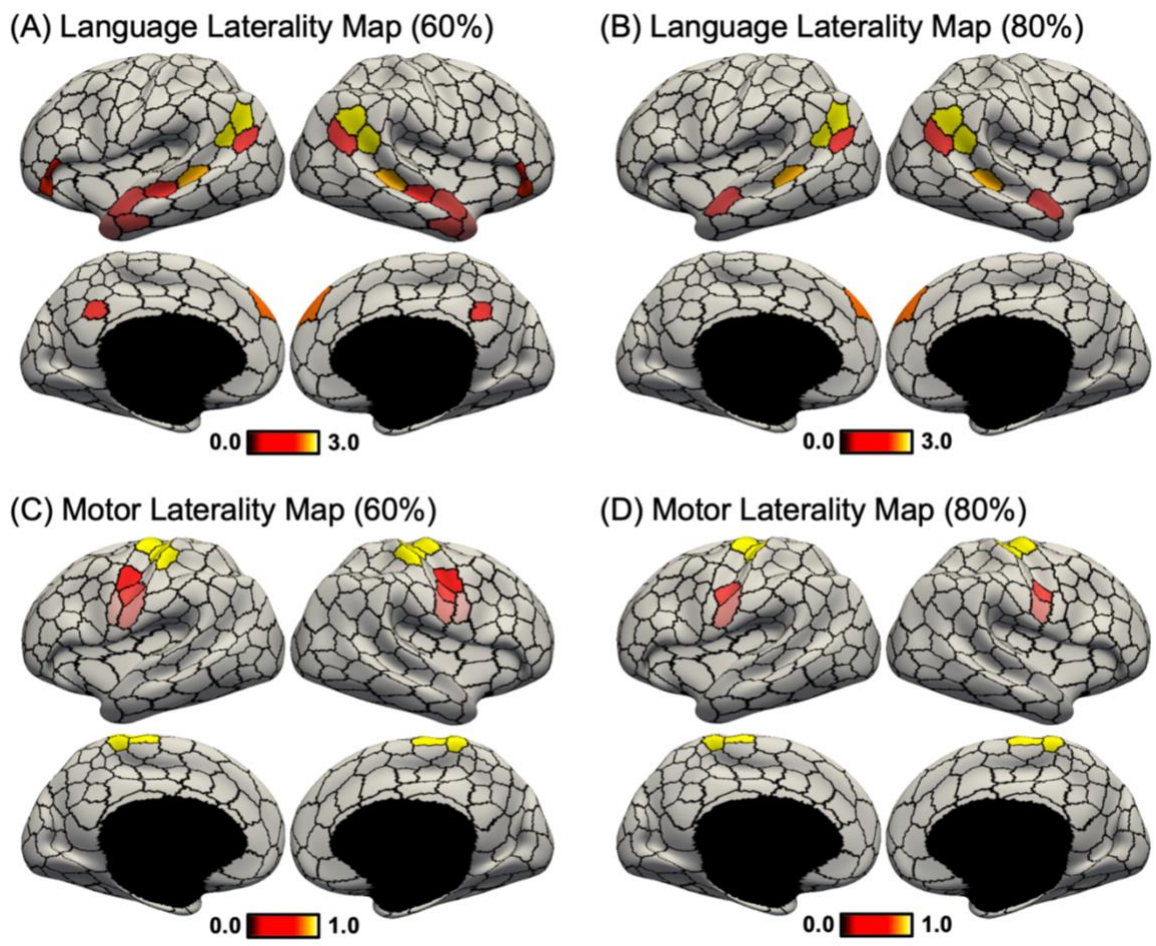

Figure S12. Task activation lateralization maps at different activation thresholds. (A) Task laterality map for the "story -math" language contrast computed for parcels whose average activations were at least 60% of the most activated parcel. (B) Task laterality map for the "story -math" language contrast computed for parcels whose average activations were at least 80% of the most activated parcel. (C) Task laterality map averaged across the motor contrasts, computed for parcels whose average activations were at least 60% of the most activated parcel. (D) Task laterality map averaged across the motor contrasts, computed for parcels whose average activations were at least 80% of the most activated parcel.

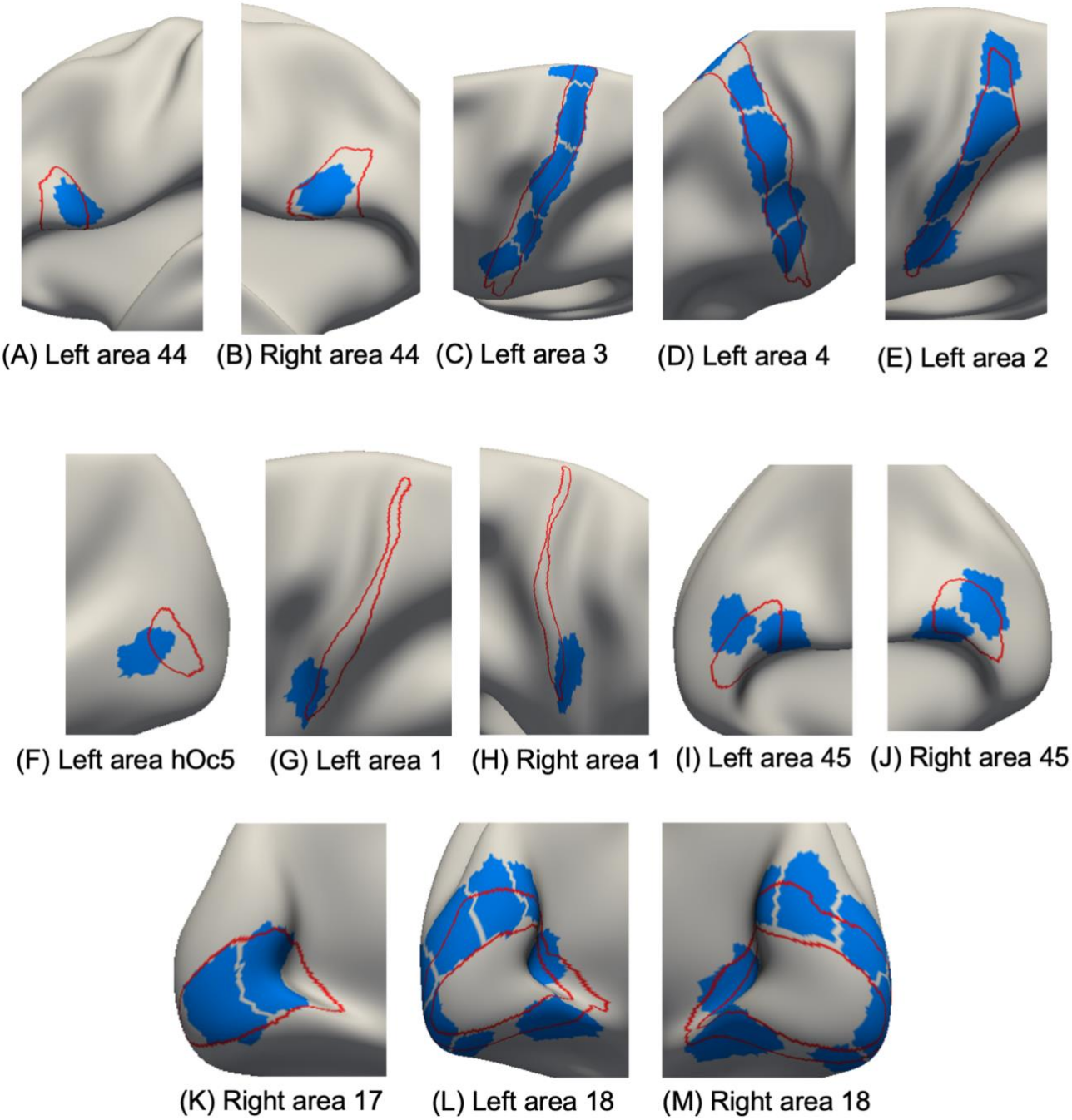

Figure S13. Parcels (blue) of the 400-region hMRF parcellation overlaid on (red) boundaries of histologically defined architectonic areas.

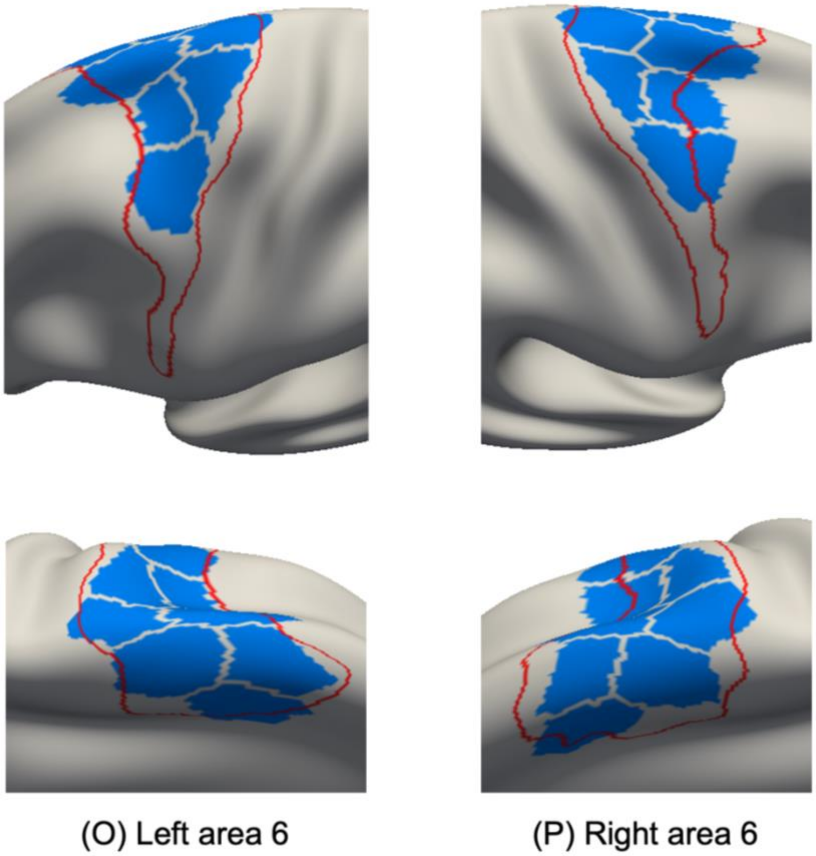

Figure S13 (cont). Parcels (blue) of the 400-region hMRF parcellation overlaid on (red) boundaries of histologically defined architectonic areas.

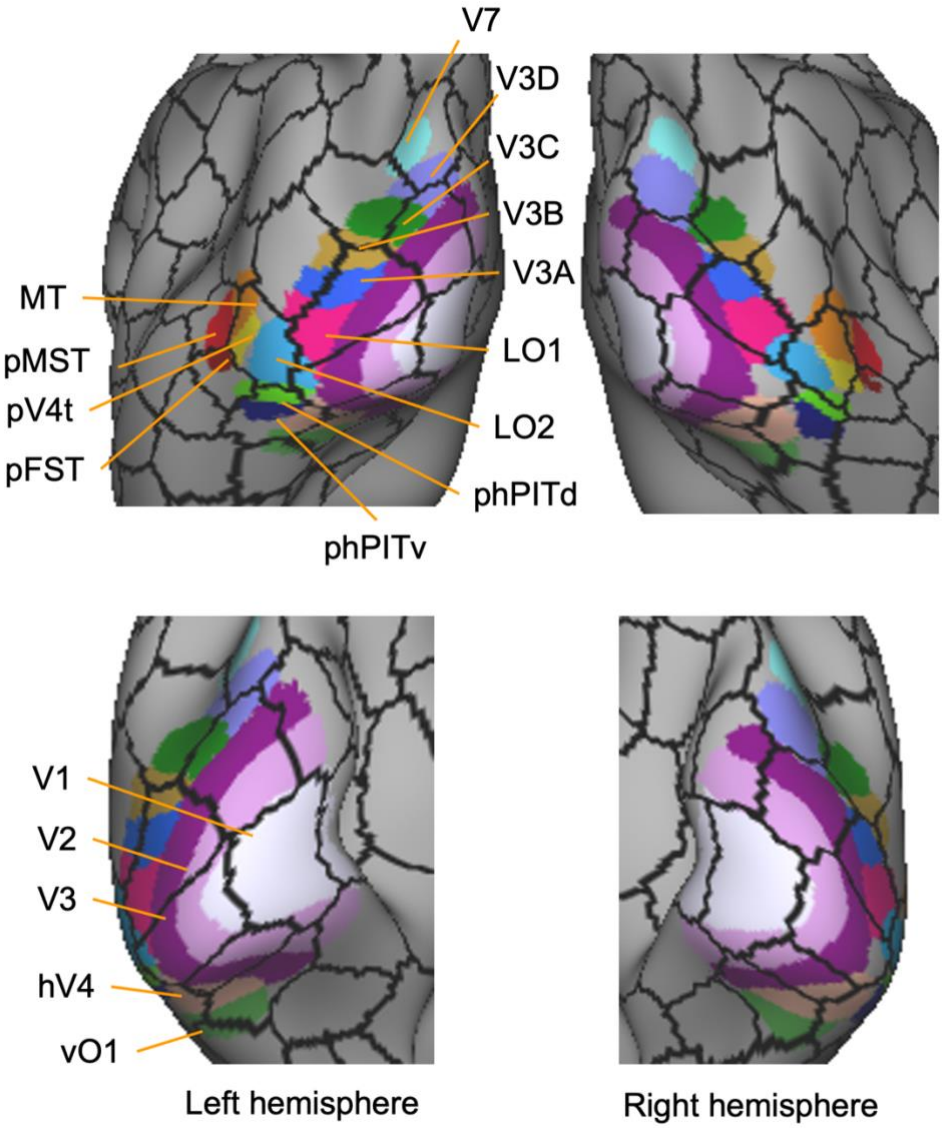

Figure S14. 18 visuotopic areas (Abdollahi et al., 2014) overlaid on (black) boundaries of the 400-region hMRF parcellation.